

Randomness of Shapes and Statistical Inference on Shapes via the Smooth Euler Characteristic Transform

Kun Meng^{1,*}, Jinyu Wang², Lorin Crawford^{3,4}, and Ani Eloyan³

¹Division of Applied Mathematics, Brown University, RI, USA

²Data Science Institute, Brown University, RI, USA

³Department of Biostatistics, Brown University School of Public Health, Providence, RI, USA

⁴Microsoft Research New England, Cambridge, MA, USA

*Address for correspondence: Kun Meng, Division of Applied Mathematics, Brown University, 182 George Street, Providence, RI 02912, USA. Email: kun_meng@brown.edu.

May 27, 2024

Abstract

In this article, we establish the mathematical foundations for modeling the randomness of shapes and conducting statistical inference on shapes using the smooth Euler characteristic transform. Based on these foundations, we propose two chi-squared statistic-based algorithms for testing hypotheses on random shapes. Simulation studies are presented to validate our mathematical derivations and to compare our algorithms with state-of-the-art methods to demonstrate the utility of our proposed framework. As real applications, we analyze a data set of mandibular molars from four genera of primates and show that our algorithms have the power to detect significant shape differences that recapitulate known morphological variation across suborders. Altogether, our discussions bridge the following fields: algebraic and computational topology, probability theory and stochastic processes, Sobolev spaces and functional analysis, analysis of variance for functional data, and geometric morphometrics.

Keywords: functional data analysis; Karhunen–Loève expansion; o-minimal structures; persistence diagrams; reproducing kernel Hilbert spaces.

1 Introduction

The quantification of shapes has become an important research direction. It has brought advances to many fields including geometric morphometrics (Boyer et al., 2011; Gao et al., 2019b,a), biophysics and structural biology (Wang et al., 2021; Tang et al., 2022), and radiogenomics (Crawford et al., 2020). When shapes are considered as random variables, their corresponding quantitative summaries are also random, implying that such summaries of random shapes are statistics. The statistical inference on shapes based on these quantitative summaries has been of particular interest (Fasy et al., 2014; Roycraft et al., 2023).

In this paper, we bring together mathematical and statistical approaches to make three significant contributions to shape statistics: (i) we provide mathematical foundations for the randomness of shapes encountered in applications, bridging algebraic topology (Hatcher, 2002) and stochastic processes (Hairer, 2009); (ii) we connect the statistical inference on shape-valued data to the well-studied analysis of variance for functional data (fdANOVA, Zhang, 2013), bridging topological data analysis (TDA, Edelsbrunner and Harer, 2010) and functional data analysis (FDA, Hsing and Eubank, 2015); and (iii) our framework does not rely on any assumptions about diffeomorphisms or pre-specified landmarks.

1.1 A Motivating Scientific Question

Through modeling the randomness of shapes, we aim to address the following statistical inference question: *Is the observed difference between two groups of shapes statistically significant?* For example, the mandibular molars in Figure 1.1 are from four genera of primates. A pertinent question from a morphological perspective is: *In Figure 1.1, do the molars from genus *Tarsius* exhibit significant differences from those from the other genera?*

The primary objective of this paper is to propose a powerful approach for testing hy-

potheses on random shapes. This would help address morphology-motivated statistical inference questions like the one raised above. In achieving this objective, we lay down the mathematical foundations that justify our hypothesis testing methods. We take two key steps: In **Step 1**, we find the appropriate representations of shapes; and in **Step 2**, we test hypotheses on shapes using these representations. In Section 1.2, we provide a literature review on shape representations and introduce the topological summary employed in this paper. Section 1.3 begins by presenting the main theme of our hypothesis testing approach, followed by an overview of our contributions. Since the molars in Figure 1.1 are diffeomorphic to the 2-dimensional unit sphere, some existing diffeomorphism-related methods can be considered for representing the molars (e.g., parameterized surfaces; Kurtek et al., 2011). In contrast, we aim to propose an approach that does not rely on any diffeomorphic assumptions, allowing for a wider range of applications.

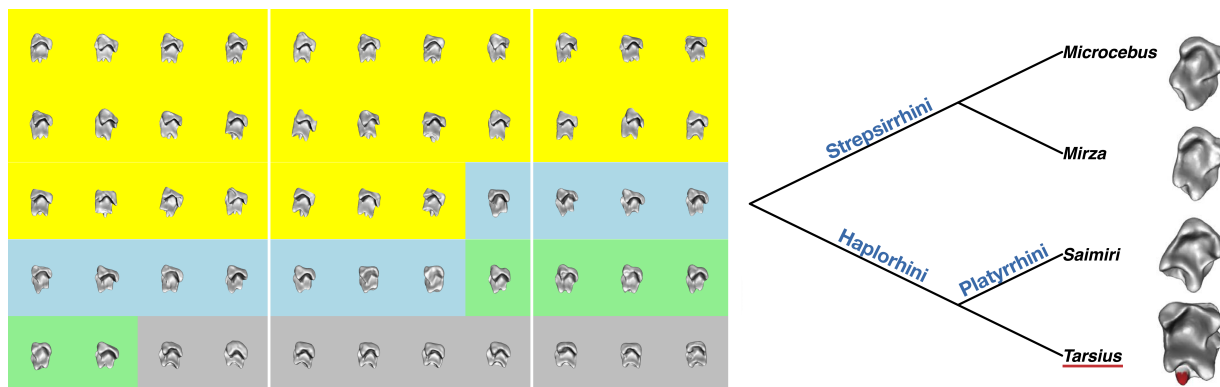


Figure 1.1: Left: Molars from two suborders of the primates: Haplorhini and Strepsirrhini. The Haplorhini suborder has genera *Tarsius* (yellow) and *Saimiri* (grey). The Strepsirrhini suborder has genera *Microcebus* (blue) and *Mirza* (green). Right: Relationship between the four primate genera. Tarsier molars exhibit additional high cusps (highlighted in red). A similar figure was published in Wang et al. (2021).

1.2 Overview of Shape and Topological Data Analysis

In classical geometric morphometrics, shapes are represented using prespecified points called landmarks (Kendall, 1989). The manual landmarking of a collection of shapes requires domain knowledge, can be very labor intensive, and is subject to bias (Boyer et al., 2011). Furthermore, an equal number of landmarks must be selected for each shape in a study in order to make comparisons (e.g., the Procrustes framework discussed in Section 2.1 of Gao et al. (2019a)). This necessitates comprehensive information about entire collections of shapes for consistency, which can be difficult to obtain (e.g., landmarking cancer tumors, which can have very different morphology across a population of patients). Unfortunately, many datasets do not come with prespecified landmarks (e.g., Goswami, 2015). Although many algorithms can automatically sample reasonable landmarks on shapes when their parameters are fine-tuned (e.g., Gao et al., 2019a,b), using a finite number of landmarks extracted from a continuum inevitably results in the loss of information. Diffeomorphism-based approaches (Dupuis et al., 1998; Gao et al., 2019a) are part of the “computational anatomy” that was historically studied by the “pattern theory school” pioneered by Ulf Grenander (Grenander and Miller, 1998). They enable the comparison of (dis-)similarity between shapes with benefit of bypassing the need for landmarks. However, these approaches are based on the assumption that the shapes being compared are diffeomorphic to one another, making them unsuitable for many datasets (e.g., fruit fly wings in Miller (2015)). Furthermore, parameterized curves and surfaces (PCS) provide a toolbox for assessing the heterogeneity of shapes with summary statistics that are invariant to reparameterizations (Kurtek et al., 2010, 2011, 2012). Despite their effectiveness in analyzing real data (e.g., DT-MRI brain fibers; Kurtek et al., 2012), PCS are based on assumptions about the diffeomorphism types of the shapes of interest. For example, Kurtek et al. (2011)

focuses on surfaces that are diffeomorphic to the 2-dimensional unit sphere.

TDA opens the door for landmark-free and diffeomorphism-free representations of shapes. Motivated by differential topology, [Turner et al. \(2014\)](#) proposed the persistent homology transform (PHT) with the capability to sufficiently encode all information within shapes ([Ghrist et al., 2018](#)). To describe the PHT, we briefly provide some basics of TDA. One common statistical invariant in TDA is the persistence diagram (PD, [Edelsbrunner and Harer, 2010](#)). When equipped with the Wasserstein distance, the collection of PDs, denoted as \mathcal{D} , is a Polish space ([Mileyko et al., 2011](#)). Thus, probability measures can be applied, and the randomness of shapes can be represented using the probability measures on \mathcal{D} . The PHT takes values in $C(\mathbb{S}^{d-1}; \mathcal{D}^d) = \{\text{continuous maps } F : \mathbb{S}^{d-1} \rightarrow \mathcal{D}^d\}$, where \mathbb{S}^{d-1} denotes the sphere $\{x \in \mathbb{R}^d : \|x\| = 1\}$ and \mathcal{D}^d is the d -fold Cartesian product of \mathcal{D} ([Turner et al., 2014](#), Lemma 2.1 and Definition 2.1). A single PD does not preserve all information of a shape ([Crawford et al., 2020](#)). In contrast, the PHT is injective, which means it preserves all the information of a shape. However, since \mathcal{D} is not a vector space and the distances on \mathcal{D} are abstract (e.g., the Wasserstein and bottleneck distances, [Cohen-Steiner et al., 2007](#)), many fundamental statistical concepts do not easily apply to summaries resulting from the PHT. For example, the definition of moments corresponding to probability measures on \mathcal{D} (e.g., means) is highly nontrivial ([Mileyko et al., 2011](#)). The difficulty in defining these concepts hinders the application of PHT-based statistical methods in $C(\mathbb{S}^{d-1}; \mathcal{D}^d)$.

The smooth Euler characteristic transform (SECT, [Crawford et al., 2020](#)) offers an alternative summary statistic for shapes. The SECT not only preserves the information of shapes ([Ghrist et al., 2018](#), Corollary 1) but also represents shapes using continuous functions instead of PDs. More precisely, the values of the SECT are maps from the sphere \mathbb{S}^{d-1} to a separable Banach space $\mathcal{B} \stackrel{\text{def}}{=} C([0, T])$, the collection of continuous functions on a compact interval $[0, T]$ (values of T will be given in Eq. (3.1)). Hence, for any shape K , its

SECT, denoted as $\{\text{SECT}(K)(\nu)\}_{\nu \in \mathbb{S}^{d-1}}$, lies in $\mathcal{B}^{\mathbb{S}^{d-1}} = \{\text{maps } F : \mathbb{S}^{d-1} \rightarrow \mathcal{B}\}$. Specifically, $\text{SECT}(K)(\nu)$ belongs to \mathcal{B} for each $\nu \in \mathbb{S}^{d-1}$. As a result, the randomness of shapes K is represented via the SECT by a collection of \mathcal{B} -valued random variables. Probability theory in separable Banach spaces is better developed than in \mathcal{D} (e.g., [Hairer, 2009](#)). In particular, a \mathcal{B} -valued random variable is a stochastic process with its sample paths in \mathcal{B} . As we will demonstrate in [Section 3](#), \mathcal{B} here can be replaced with a reproducing kernel Hilbert space (RKHS). The theory of stochastic processes has evolved over a century and FDA is a well-developed branch of statistics. Consequently, a myriad of tools are available to underpin both the randomness of shapes and the statistical inference on shapes.

From an application perspective, [Crawford et al. \(2020\)](#) applied the SECT to magnetic resonance images taken from tumors in a cohort of glioblastoma multiforme (GBM) patients. Using summary statistics derived from the SECT as predictors within Gaussian process regression, the authors demonstrated that the SECT can predict clinical outcomes more effectively than existing tumor shape quantification approaches and common molecular assays. The relative performance of the SECT in the GBM study suggests a promising future for its utility in medical imaging and broader statistical applications related to shape analyses. Similarly, [Wang et al. \(2021\)](#) utilized derivatives of the Euler characteristic transform (ECT) as predictors in statistical models for subimage analysis. This analysis is akin to variable selection, aiming to identify physical features that are important for distinguishing between two classes of shapes. Lastly, [Marsh et al. \(2022\)](#) highlighted that the SECT outperforms the standard measures employed in organoid morphology.

1.3 Overview of Contributions and Paper Organization

Our goal is to address the hypothesis testing question posed in Section 1.1 by employing a landmark-free and diffeomorphism-free approach, which opens up possibilities for further applications in the future. We formulate the question more generically here. Let $\mathbb{P}^{(1)}$ and $\mathbb{P}^{(2)}$ be two distributions that generate two collections of random shapes, $\{K_i^{(1)}\}_{i=1}^n$ and $\{K_i^{(2)}\}_{i=1}^n$. Detecting whether there is a significant difference between $\{K_i^{(1)}\}_{i=1}^n$ and $\{K_i^{(2)}\}_{i=1}^n$ is equivalent to rejecting the hypothesis $\mathbb{P}^{(1)} = \mathbb{P}^{(2)}$. Since each shape $K_i^{(j)}$ is random, $\text{SECT}(K_i^{(j)})$ is a random variable taking values in a vector space (as discussed in Section 1.2) and can be decomposed as follows (see Theorem 5.1 for a rigorous version)

$$\text{SECT}(K_i^{(j)}) = m^{(j)} + \text{random terms}, \quad \text{for } j \in \{1, 2\}, \quad (1.1)$$

where $m^{(j)}$ denotes the mean of $\text{SECT}(K_i^{(j)})$ with respect to the distribution $\mathbb{P}^{(j)}$. The random terms in Eq. (1.1) can be characterized by the Karhunen–Loève (KL) expansion (Hsing and Eubank, 2015, Section 7.3). To reject $\mathbb{P}^{(1)} = \mathbb{P}^{(2)}$, it suffices to reject $m^{(1)} = m^{(2)}$. That is, the question posed in Section 1.1 can be addressed by testing for the equality of two means. The important component of the test is the variance represented by the random terms in Eq. (1.1). In Section 5, we formulate this test as a two-sample problem in the fdANOVA literature (Zhang, 2013, Section 5.2). In addition, using the KL expansion, we provide a χ^2 -statistic in Section 5 to test the hypothesis. Throughout the paper, our focus is on the two-sample problem. However, one may also consider employing the one-way fdANOVA to compare the means of three or more groups of shapes. The theoretical foundation and numerical experiments for this aspect are left for future research.

To develop our framework, we have to address the following mathematical foundation related questions: (i) *What underlying probability spaces allow the randomness of shapes and their corresponding SECT?* and (ii) *Are the conditions of the KL expansion satisfied in*

our setting? We answer these questions in Sections 3 and 4 — we model the randomness of shapes via the SECT using RKHS-valued random fields. The “theory of random sets” is a well-established framework for characterizing set-valued random variables (Molchanov, 2005). However, its application to persistent homology-based statistics (e.g., the SECT) remains underexplored. In this paper, we introduce a new probability space to characterize the randomness of shapes in a manner compatible with the SECT.

We first propose a collection of shapes as our sample space on which the SECT is well-defined. We then demonstrate that every shape in this collection has its SECT in $C(\mathbb{S}^{d-1}; \mathcal{H}) = \{\text{continuous maps } F : \mathbb{S}^{d-1} \rightarrow \mathcal{H}\}$, where $\mathcal{H} = H_0^1([0, T])$ is not only a Sobolev space (Brezis, 2011) but also an RKHS (reasons for using $[0, T]$ instead of $(0, T)$ for $H_0^1([0, T])$ are in Appendix A.1). Importantly, $C(\mathbb{S}^{d-1}; \mathcal{H})$ is a separable Banach space (Theorem C.1) and, hence, a Polish space. It helps construct a probability space to characterize the distributions of shapes. Building on this probability space, we define the mean and covariance of the SECT. Using the Sobolev embedding, we present some properties of the mean and covariance, which pave the way for the KL expansion of the SECT.

Traditionally, the statistical inference on shapes in TDA is conducted in the persistence diagram space \mathcal{D} , which is unsuitable for exponential family-based distributions and requires any corresponding statistical inference to be highly nonparametric (Fasy et al., 2014; Robinson and Turner, 2017). The PHT-based statistical inference in $C(\mathbb{S}^{d-1}; \mathcal{D}^d)$ is even more difficult. With the KL expansion of the SECT, we propose a χ^2 -statistic for testing hypotheses on shapes. Beyond the mathematical foundations, we also provide simulation studies to illustrate the performance of our proposed hypothesis testing method. Lastly, we apply our proposed framework to answer the motivating question raised in Section 1.1.

We organize this paper as follows. In Section 2, we provide the mathematical preparations. In Section 3, we define the SECT for a specific collection of shapes, highlighting its

properties. In Section 4, we construct a probability space to model shape distributions. In Section 5, we propose the KL expansion of the SECT, leading to a statistic for hypothesis testing. In Section 6, we conduct simulation studies to evaluate our method. In Section 7, we apply our method to real data. In Section 8, we conclude the paper. The Appendix provides the proofs of theorems, further data analysis, and future research topics.

2 Notations and Mathematical Preparations

To model the shapes discussed in our motivating question from Section 1.1, we need certain preparations regarding (i) topology and (ii) function spaces.

Topology. The first question we must address is: *What are the “shapes” in our framework?* Ghrist et al. (2018) and Curry et al. (2022) applied o-minimal structures (van den Dries, 1998) to prove the injectivity of the PHT. Subsequent to this, o-minimal structures have been applied in many TDA studies to model shapes (e.g., Jiang et al., 2020; Kirveslahti and Mukherjee, 2023). To stay consistent with the existing literature, we also model shapes using o-minimal structures. An o-minimal structure is a sequence $\mathcal{S} = \{\mathcal{S}_n\}_{n \geq 1}$ of subset collections $\mathcal{S}_n \subseteq 2^{\mathbb{R}^n}$ satisfying six set-theoretical axioms, where $2^{\mathbb{R}^n}$ denotes the power set of \mathbb{R}^n . The precise definition of o-minimal structures is available in van den Dries (1998) and is provided in Appendix A.3 for the reader’s convenience.

A typical example of o-minimal structures is the collection of *semialgebraic sets*. Specifically, a set $K \subseteq \mathbb{R}^n$ is semialgebraic if it can be expressed as a finite union of sets of the form $\{x \in \mathbb{R}^n \mid p(x) = 0, q_1(x) > 0, \dots, q_k(x) > 0\}$, where p, q_1, \dots, q_k are polynomial functions on \mathbb{R}^n . If we define \mathcal{S}_n as the collection of semialgebraic subsets of \mathbb{R}^n , then $\mathcal{S} = \{\mathcal{S}_n\}_{n \geq 1}$ is an o-minimal structure (van den Dries, 1998, Chapter 2). The unit sphere \mathbb{S}^{d-1} , open ball $B(0, R) = \{x \in \mathbb{R}^d \mid \|x\|^2 < R^2\}$ for any $R > 0$, and all polyhedra (e.g., polygon meshes in

computer graphics) are semialgebraic, given that they can be represented using either the polynomial $\|x\|^2$ or affine functions. We assume the following:

Assumption 1. *The o-minimal structure \mathcal{S} of interest contains all semialgebraic sets.*

Hereafter, a “shape” refers to a compact set $K \in \bigcup_{n \geq 1} \mathcal{S}_n$ for a prespecified o-minimal structure $\mathcal{S} = \{\mathcal{S}_n\}_{n \geq 1}$ satisfying Assumption 1. Assumption 1 incorporates many common shapes (e.g., balls and polyhedra) in our framework. More importantly, it implies the subsequent Theorem 2.1 through the “triangulation theorem” (van den Dries, 1998, Chapter 8). Although the definition of an o-minimal structure \mathcal{S} is highly abstract (see Appendix A.3), each compact set in \mathcal{S} resembles a polyhedron, which is precisely stated as follows.

Theorem 2.1. *Suppose $\mathcal{S} = \{\mathcal{S}_n\}_{n \geq 1}$ is an o-minimal structure satisfying Assumption 1 and $K \in \bigcup_{n \geq 1} \mathcal{S}_n$. If K is compact, there exists a finite simplicial complex S such that the polyhedron $|S| \stackrel{\text{def}}{=} \bigcup_{s \in S} s$ is homeomorphic to K , where each $s \in S$ denotes a simplex.*

Herein, a finite simplicial complex S is a finite collection of simplexes. Each face of a simplex $s \in S$ also belongs to S (i.e., S is a so-called “closed complex” referred to in Chapter 8 of van den Dries (1998)). Theorem 2.1 directly results from the “triangulation theorem” (van den Dries, 1998); hence, its proof is omitted. For the d -th component \mathcal{S}_d of $\mathcal{S} = \{\mathcal{S}_n\}_{n \geq 1}$, Theorem 2.1 indicates that the compact sets $K \in \mathcal{S}_d$ are subsets of \mathbb{R}^d that are homeomorphic to polyhedra. Theorem 2.1 also implies that the homology groups of each compact $K \in \mathcal{S}_d$ are well-defined and finitely generated; hence, the Betti numbers and Euler characteristic of K are well-defined and finite (Hatcher, 2002, Chapter 2).

Function Spaces. We apply the following notations throughout this paper:

- (i) For any normed space \mathcal{V} , let $\|\cdot\|_{\mathcal{V}}$ denote its norm. Denote $\|\cdot\|_{\mathbb{R}^d}$ as $\|\cdot\|$ for succinctness.
- (ii) Let X be a compact metric space equipped with metric d_X , and let \mathcal{V} denote a normed space. $C(X; \mathcal{V})$ is the collection of continuous maps from X to \mathcal{V} . Furthermore, $C(X; \mathcal{V})$ is

a normed space equipped with $\|f\|_{C(X;\mathcal{V})} = \sup_{x \in X} \|f(x)\|_{\mathcal{V}}$. The Hölder space $C^{0,\frac{1}{2}}(X;\mathcal{V})$ is defined as $\left\{ f \in C(X;\mathcal{V}) \mid \sup_{x,y \in X, x \neq y} \left(\frac{\|f(x)-f(y)\|_{\mathcal{V}}}{\sqrt{d_X(x,y)}} \right) < \infty \right\}$. Here, $C^{0,\frac{1}{2}}(X;\mathcal{V})$ is a normed space equipped with $\|f\|_{C^{0,\frac{1}{2}}(X;\mathcal{V})} = \|f\|_{C(X;\mathcal{V})} + \sup_{x,y \in X, x \neq y} \left(\frac{\|f(x)-f(y)\|_{\mathcal{V}}}{\sqrt{d_X(x,y)}} \right)$. Obviously, $C^{0,\frac{1}{2}}(X;\mathcal{V}) \subseteq C(X;\mathcal{V})$. For simplicity, we denote $C(X) = C(X;\mathbb{R})$ and $C^{0,\frac{1}{2}}(X) = C^{0,\frac{1}{2}}(X;\mathbb{R})$. For a given $T > 0$ (e.g., see Eq. (3.1)), we denote $C([0, T])$ as \mathcal{B} .

(iii) The inner product of $\mathcal{H} = H_0^1([0, T]) = \{f \in L^2([0, 1]) \mid f' \in L^2([0, T]) \text{ and } f(0) = f(T) = 0\}$ is defined as $\langle f, g \rangle = \int_0^T f'(t)g'(t) dt$ (Brezis, 2011, Chapter 8.3, Remark 17).

(iv) Suppose (Y, d_Y) is a metric space (not necessarily compact). Both $\mathcal{B}(Y)$ and $\mathcal{B}(d_Y)$ denote the Borel algebra generated by the metric topology corresponding to d_Y .

(v) $\{F(z)\}_{z \in Z}$ denotes a function F defined on the set Z .

The following inequalities are useful for deriving many results presented in this paper

$$\|f\|_{\mathcal{B}} \leq \|f\|_{C^{0,\frac{1}{2}}([0,T])} \leq \tilde{C}_T \|f\|_{\mathcal{H}}, \quad \text{for all } f \in \mathcal{H}, \quad (2.1)$$

where \tilde{C}_T is a constant depending only on T . The first inequality in Eq. (2.1) results from the definition of $\|\cdot\|_{C^{0,\frac{1}{2}}([0,T])}$, while the second inequality is from Brezis (2011) (Corollary 9.14; also see Appendix L.2). Eq. (2.1) implies the following Sobolev embedding

$$H_0^1([0, T]) \stackrel{\text{def}}{=} \mathcal{H} \subseteq C^{0,\frac{1}{2}}([0, T]) \subseteq \mathcal{B} \stackrel{\text{def}}{=} C([0, T]). \quad (2.2)$$

3 Smooth Euler Characteristic Transform

In this section, we give the background on the SECT and propose corresponding mathematical foundations. Notably, we specify the “sample space” — a collection of shapes on which the SECT is well-defined. The SECT of the shapes in this sample space has properties that are suitable for the probability theory developed in Section 4. The molars in the motivating question from Section 1.1 will be modeled as elements of the sample space.

Suppose an o-minimal structure $\mathcal{S} = \{\mathcal{S}_n\}_{n \geq 1}$ satisfying Assumption 1 is given, and we focus on shapes in d -dimensional space \mathbb{R}^d . We assume the shape $K \in \mathcal{S}_d$ is compact and $K \subseteq B(0, R) = \{x \in \mathbb{R}^d : \|x\| < R\}$, e.g., the $K \subseteq \mathbb{R}^2$ in Figure 3.1 or the surfaces of the mandibular molars in \mathbb{R}^3 as presented by Figure 1.1. For each direction $\nu \in \mathbb{S}^{d-1}$, we define a filtration $\{K_t^\nu\}_{t \in [0, T]}$ of sublevel sets by the following (see Figure 3.1 for an illustration)

$$K_t^\nu \stackrel{\text{def}}{=} \{x \in K \mid x \cdot \nu \leq t - R\}, \quad \text{for all } t \in [0, T], \quad \text{where } T \stackrel{\text{def}}{=} 2R. \quad (3.1)$$

We then have the following Euler characteristic curve (ECC, denoted as χ_t^ν) in direction ν

$$\chi_t^\nu(K) \stackrel{\text{def}}{=} \text{the Euler characteristic of } K_t^\nu = \chi(K_t^\nu) = \sum_{k=0}^{d-1} (-1)^k \cdot \beta_k(K_t^\nu), \quad (3.2)$$

for $t \in [0, T]$, where $\beta_k(K_t^\nu)$ is the k -th Betti number of K_t^ν . The sum in Eq. (3.2) ends at $d - 1$ because higher homology groups are trivial (Curry et al., 2022, Section 4). If K_t^ν is a triangle mesh, $\chi(K_t^\nu) = \#V - \#E + \#F$, where $\#V$, $\#E$, and $\#F$ denote the number of vertices, edges, and faces of the mesh, respectively. Due to Theorem 2.1, the compactness of K guarantees that the Betti numbers in Eq. (3.2) are well-defined and finite.

The Euler characteristic transform (ECT) defined as $\text{ECT}(K) : \mathbb{S}^{d-1} \rightarrow \mathbb{Z}^{[0, T]}$, $\nu \mapsto \{\chi_t^\nu(K)\}_{t \in [0, T]}$ was proposed by Turner et al. (2014) as an alternative to the PHT. Based on the ECT, Crawford et al. (2020) further proposed the SECT as follows

$$\begin{aligned} \text{SECT}(K) : \mathbb{S}^{d-1} &\rightarrow \mathbb{R}^{[0, T]}, \quad \nu \mapsto \text{SECT}(K)(\nu) = \{\text{SECT}(K)(\nu, t)\}_{t \in [0, T]}, \\ \text{where } \text{SECT}(K)(\nu, t) &\stackrel{\text{def}}{=} \int_0^t \chi_\tau^\nu(K) d\tau - \frac{t}{T} \int_0^T \chi_\tau^\nu(K) d\tau. \end{aligned} \quad (3.3)$$

A visualization of the function $(\nu, t) \mapsto \text{SECT}(K)(\nu, t)$ is presented in Figure 3.1. The following lemma implies that the Lebesgue integrals in Eq. (3.3) are well-defined.

Lemma 3.1. *For any fixed $K \in \mathcal{S}_d$ and $\nu \in \mathbb{S}^{d-1}$, the function $t \mapsto \chi(K_t^\nu)$ is piecewise constant with only finitely many discontinuities.*

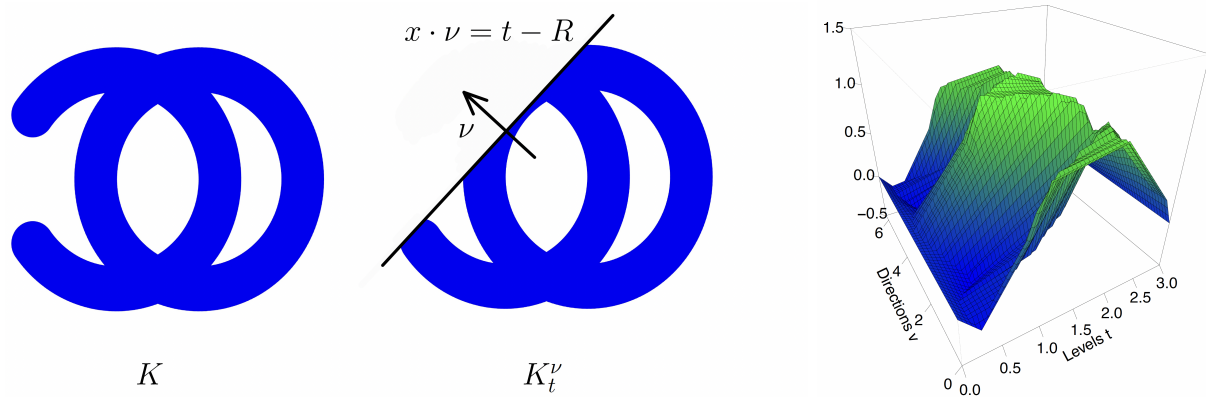


Figure 3.1: Consider the 2-dimensional shape $K \in \mathcal{S}_2$ in the left panel. For each pair of ν and t , the equation $x \cdot \nu = t - R$ represents a straight line (or a hyperplane in a high-dimensional space). The subset K_t^ν denotes the region below this line. Let $\phi_\nu(x) = x \cdot \nu + R$, then $K_t^\nu = \{x \in K \mid \phi_\nu(x) \leq t\}$. The right panel presents the function $(\nu, t) \mapsto \text{SECT}(K)(\nu, t)$, where $\nu \in \mathbb{S}^1$ is identified by $\theta \in [0, 2\pi]$ through $\nu = (\cos \theta, \sin \theta)$. Procedures for generating the shape K and the right panel are given in Appendix D.1.

Through the “cell decomposition theorem” (van den Dries, 1998, Chapter 3), Lemma 3.1 directly follows from either Lemma 3.4 of Curry et al. (2022) or “(2.10) Proposition” in Chapter 4 of van den Dries (1998). Hence, the proof of Lemma 3.1 is omitted.

To investigate the distribution of $\text{SECT}(K)$ over different shapes K , we introduce the following condition to restrict our attention to a subset of \mathcal{S}_d .

Condition 3.1. *Let $K \in \mathcal{S}_d$. The condition is that K satisfies the following inequality*

$$\sup_{k \in \{0, \dots, d-1\}} \left[\sup_{\nu \in \mathbb{S}^{d-1}} \left(\#\left\{ \xi \in \text{Dgm}_k(K; \phi_\nu) \mid \text{pers}(\xi) > 0 \right\} \right) \right] \leq \frac{M}{d}, \quad (3.4)$$

where $\text{Dgm}_k(K; \phi_\nu)$ is the PD of K associated with the function $\phi_\nu(x) = x \cdot \nu + R$ (also see Figure 3.1), $\text{pers}(\xi)$ is the persistence of the homology feature ξ , $\#\{\cdot\}$ denotes the cardinality of a multiset, and $M > 0$ is a sufficiently large prespecified number.

Condition 3.1 involves technicalities from computational topology (Edelsbrunner and Harer, 2010). To maintain the flow of the paper, we relegate the details of this condition, as well as the definitions of $\text{Dgm}_k(K; \phi_\nu)$ and $\text{pers}(\xi)$, to Appendix B. Heuristically, Condition

3.1 implies the existence of a uniform upper bound on the number of nontrivial homology features of K across all directions ν . Hereafter, we focus on shapes in the following collection

$$\mathcal{S}_{R,d}^M \stackrel{\text{def}}{=} \{K \in \mathcal{S}_d \mid K \subseteq B(0, R) \text{ is compact and satisfies Condition 3.1 with fixed } M > 0\}.$$

Our proposed collection $\mathcal{S}_{R,d}^M$ is suitable for modeling shapes in many applications. For example, the surfaces of the molars in Figure 1.1 are compact subsets of \mathbb{R}^3 , bounded by a common open ball, and can be approximately represented by triangle meshes (hence, modeled by an o-minimal structure satisfying Assumption 1). In addition, the four genera of primates in Figure 1.1 share a phylogenetic relationship which implies that their molars have common baseline features and satisfy Condition 3.1 with a shared upper bound M . In each application, the dimension d and radius R of the ball $B(0, R)$ can easily be determined based on observed shapes. Although our mathematical framework requires the existence of such an M in Eq. (3.4), the value of M is not needed for our statistical methodology (see Section 5). Thus, Condition 3.1 does not hinder our proposed statistical methodology.

Lemma 3.1 implies that the function $\{\chi_t^\nu(K)\}_{t \in [0, T]}$ of t belongs to $L^1([0, T])$. Therefore, the function $\text{SECT}(K)(\nu) = \{\text{SECT}(K)(\nu, t)\}_{t \in [0, T]}$ of t is absolutely continuous on $[0, T]$. Furthermore, we have the following regularity result of the Sobolev type.

Lemma 3.2. *For any $K \in \mathcal{S}_{R,d}^M$ and $\nu \in \mathbb{S}^{d-1}$, the function $\text{SECT}(K)(\nu)$ belongs to \mathcal{H} .*

Lemma 3.2 is a special case of Lemma C.3. It indicates $\text{SECT}(\mathcal{S}_{R,d}^M) \subseteq \mathcal{H}^{\mathbb{S}^{d-1}} = \{\text{all maps } F : \mathbb{S}^{d-1} \rightarrow \mathcal{H}\}$, which is enhanced by the following result.

Theorem 3.2. *For each $K \in \mathcal{S}_{R,d}^M$, we have: (i) There exists a constant $C_{M,R,d}^*$ depending only on M , R , and d such that the following inequality holds for any directions $\nu_1, \nu_2 \in \mathbb{S}^{d-1}$,*

$$\|\text{SECT}(K)(\nu_1) - \text{SECT}(K)(\nu_2)\|_{\mathcal{H}} \leq C_{M,R,d}^* \cdot \sqrt{\|\nu_1 - \nu_2\| + \|\nu_1 - \nu_2\|^2}; \quad (3.5)$$

and (ii) $\text{SECT}(K) \in C^{0, \frac{1}{2}}(\mathbb{S}^{d-1}; \mathcal{H})$, where \mathbb{S}^{d-1} is equipped with the geodesic distance $d_{\mathbb{S}^{d-1}}$.

Results complementary to Theorem 3.2 can be found in Theorem C.3, which imply that the function $(\nu, t) \mapsto \text{SECT}(K)(\nu, t)$ belongs to $C^{0, \frac{1}{2}}(\mathbb{S}^{d-1} \times [0, T])$. Theorem 3.2(i) is an analog of Lemma 2.1 in Turner et al. (2014). Theorem 3.2(ii) implies $\text{SECT}(\mathcal{S}_{R,d}^M) \subseteq C^{0, \frac{1}{2}}(\mathbb{S}^{d-1}; \mathcal{H}) \subseteq C(\mathbb{S}^{d-1}; \mathcal{H}) \subseteq \mathcal{H}^{\mathbb{S}^{d-1}}$. As a result, Eq. (3.3) defines the following map

$$\text{SECT} : \mathcal{S}_{R,d}^M \rightarrow C(\mathbb{S}^{d-1}; \mathcal{H}), \quad K \mapsto \text{SECT}(K). \quad (3.6)$$

In Appendix D.1, we provide detailed proof-of-concept examples (similar to Figure 3.1) to visually illustrate the SECT and support the regularity results in Theorems 3.2 and C.3.

Corollary 1 of Ghrist et al. (2018) implies the following result, which shows that the SECT preserves all the information of shapes $K \in \mathcal{S}_{R,d}^M$.

Theorem 3.3. *The map SECT defined in Eq. (3.6) is injective for all dimensions d .*

The map $\text{SECT} : \mathcal{S}_{R,d}^M \rightarrow C(\mathbb{S}^{d-1}; \mathcal{H})$ is injective, but not surjective. Specifically, Theorem 3.2 suggests that the image of SECT does not lie outside of $C^{0, \frac{1}{2}}(\mathbb{S}^{d-1}; \mathcal{H})$. An explicit characterization of the image $\text{SECT}(\mathcal{S}_{R,d}^M)$ remains a topic for future research.

Inspired by Theorem 3.3, one may consider reconstructing a shape K from either the $\text{SECT}(K)$ or the $\text{ECT}(K)$. From a theoretical standpoint, a shape K can be reconstructed using the ‘‘Schapira’s inversion formula’’ (Schapira, 1995). Further details are available in Ghrist et al. (2018). From an algorithmic perspective, the proof of Theorem 3.1 in Turner et al. (2014) offers an algorithm to reconstruct low-dimensional meshes from their ECT. Nevertheless, effective algorithmic approaches to reconstructing shapes are still underdeveloped. Challenges in reconstructing shapes are extensively discussed in Fasy et al. (2018). A comprehensive exploration of the reconstruction using SECT is also left for future research.

Together with Eq. (3.6), Theorem 3.3 allows us to represent each $K \in \mathcal{S}_{R,d}^M$ by $\text{SECT}(K) \in C(\mathbb{S}^{d-1}; \mathcal{H})$. This perspective aids us in modeling the randomness of shapes using probability measures on the separable Banach space $C(\mathbb{S}^{d-1}; \mathcal{H})$. Here, we prefer $C(\mathbb{S}^{d-1}; \mathcal{H})$

over $\frac{1}{2}$ -Hölder space $C^{0,\frac{1}{2}}(\mathbb{S}^{d-1}; \mathcal{H})$. This is because $\frac{1}{2}$ -Hölder spaces are typically not separable (Hairer, 2009, Remark 4.21). The separability condition is essential for probability measures on Banach spaces to exhibit non-pathological behavior (Hairer, 2009, Section 4).

4 Probabilistic Distributions over the SECT

To address the motivating question outlined in Section 1.1 using hypothesis testing, we need to view the observed shapes (e.g., the molars in Figure 1.1) as shape-valued random variables. In this section, we construct a probability space to model the randomness of shapes and make the SECT a random variable (in the measurable sense) taking values in $C(\mathbb{S}^{d-1}; \mathcal{H})$. More importantly, this probability space helps justify the KL expansion of the SECT, which lays the foundations for our hypothesis testing method in Section 5.

Probability Space. Suppose $\mathcal{S}_{R,d}^M$ is equipped with a σ -algebra \mathcal{F} . A distribution of shapes K across $\mathcal{S}_{R,d}^M$ is represented by a probability measure $\mathbb{P} = \mathbb{P}(dK)$ on \mathcal{F} . Then, $(\mathcal{S}_{R,d}^M, \mathcal{F}, \mathbb{P})$ is a probability space. For each fixed (ν, t) , the integer-valued map $\chi_t^\nu : K \mapsto \chi_t^\nu(K)$ is defined on $\mathcal{S}_{R,d}^M$. Hereafter, we assume the following:

Assumption 2. *For each fixed $(\nu, t) \in \mathbb{S}^{d-1} \times [0, T]$, the map $\chi_t^\nu : (\mathcal{S}_{R,d}^M, \mathcal{F}) \rightarrow (\mathbb{R}, \mathcal{B}(\mathbb{R}))$ is a measurable function and, hence, a real-valued random variable.*

A σ -algebra \mathcal{F} satisfying Assumption 2 exists. Here, we construct a metric ρ on $\mathcal{S}_{R,d}^M$ and show that the Borel algebra $\mathcal{B}(\rho)$ induced by ρ satisfies Assumption 2. We define

$$\rho(K_1, K_2) \stackrel{\text{def}}{=} \sup_{\nu \in \mathbb{S}^{d-1}} \left\{ \left(\int_0^T \left| \chi_\tau^\nu(K_1) - \chi_\tau^\nu(K_2) \right|^2 d\tau \right)^{1/2} \right\}, \quad \text{for all } K_1, K_2 \in \mathcal{S}_{R,d}^M. \quad (4.1)$$

Theorem 4.1. *The map ρ is a metric on $\mathcal{S}_{R,d}^M$. Assumption 2 is satisfied if $\mathcal{F} = \mathcal{B}(\rho)$.*

Under Assumption 2, the ECC $\{\chi_t^\nu\}_{t \in [0, T]}$, for each $\nu \in \mathbb{S}^{d-1}$, is a stochastic process defined on the probability space $(\mathcal{S}_{R,d}^M, \mathcal{F}, \mathbb{P})$. Since each sample path $\{\chi_t^\nu(K)\}_{t \in [0, T]}$ has

finitely many discontinuities (Lemma 3.1), $\int_0^t \chi_\tau^\nu(K) d\tau$ for each $t \in [0, T]$ is a Riemann integral, which is equal to the limit of Riemann sum $\int_0^t \chi_\tau^\nu(K) d\tau = \lim_{n \rightarrow \infty} \left\{ \frac{t}{n} \sum_{l=1}^n \chi_{\frac{tl}{n}}^\nu(K) \right\}$. Given that each $\chi_{\frac{tl}{n}}^\nu$ is a random variable under Assumption 2, the limit of the Riemann sum for each $t \in [0, T]$ is a random variable as well. Therefore, for each $\nu \in \mathbb{S}^{d-1}$, $\left\{ \int_0^t \chi_\tau^\nu d\tau \right\}_{t \in [0, T]}$ with $\int_0^t \chi_\tau^\nu d\tau : K \mapsto \int_0^t \chi_\tau^\nu(K) d\tau$ is a stochastic process. Then, under Assumption 2, Eq. (3.3) defines the following stochastic process on $(\mathcal{S}_{R,d}^M, \mathcal{F}, \mathbb{P})$ for each $\nu \in \mathbb{S}^{d-1}$

$$\text{SECT}(\nu) \stackrel{\text{def}}{=} \left\{ \int_0^t \chi_\tau^\nu d\tau - \frac{t}{T} \int_0^T \chi_\tau^\nu d\tau \stackrel{\text{def}}{=} \text{SECT}(\nu, t) \right\}_{t \in [0, T]}. \quad (4.2)$$

Precisely, for each fixed ν , we have the stochastic process $\text{SECT}(\nu) : K \mapsto \text{SECT}(K)(\nu) = \left\{ \text{SECT}(K)(\nu, t) \right\}_{t \in [0, T]}$ defined on $(\mathcal{S}_{R,d}^M, \mathcal{F}, \mathbb{P})$; and, for each fixed (ν, t) , we have the real-valued random variable $\text{SECT}(\nu, t) : K \mapsto \text{SECT}(K)(\nu, t)$ defined on $(\mathcal{S}_{R,d}^M, \mathcal{F}, \mathbb{P})$.

Since \mathcal{H} is an RKHS (Appendix A.1), Lemma 3.2 and Theorem 3.2, together with Theorem 7.1.2 of Hsing and Eubank (2015), imply the following. Its proof is omitted.

Theorem 4.2. (i) For each $\nu \in \mathbb{S}^{d-1}$, $\text{SECT}(\nu)$ is a real-valued stochastic process with sample paths in \mathcal{H} . Equivalently, $\text{SECT}(\nu)$ is a random variable taking values in $(\mathcal{H}, \mathcal{B}(\mathcal{H}))$.
(ii) The map SECT defined in Eq. (3.6) is a random variable taking values in $C(\mathbb{S}^{d-1}; \mathcal{H})$.

Using Theorem 4.2 in conjunction with Theorem 3.3, we can represent random shapes (which model the surfaces of the mandibular molars in Figure 1.1) as $C(\mathbb{S}^{d-1}, \mathcal{H})$ -valued random variables. This representation through the SECT has no loss of information.

In Appendix D.2, we provide proof-of-concept examples to illustrate random shapes and their SECT representations visually. These examples relate the SECT to Fréchet regression (Petersen and Müller, 2019), Wasserstein regression (Chen et al., 2023), and manifold learning (Dunson and Wu, 2021; Meng and Eloyan, 2021; Li et al., 2022).

Mean and Covariance of the SECT. For deriving the KL expansion in Section 5, we define the mean and covariance of the SECT. To do so, we need the following lemma.

Lemma 4.1. *For any probability measure \mathbb{P} defined on the measurable space $(\mathcal{S}_{R,d}^M, \mathcal{F})$, we have $\mathbb{E} \{ \sup_{\nu \in \mathbb{S}^{d-1}} \|\text{SECT}(\nu)\|_{\mathcal{H}}^2 \} = \int_{\mathcal{S}_{R,d}^M} \{ \sup_{\nu \in \mathbb{S}^{d-1}} \|\text{SECT}(K)(\nu)\|_{\mathcal{H}}^2 \} \mathbb{P}(dK) < \infty$.*

Lemma 4.1, together with Eq. (2.1), implies that $\mathbb{E} |\text{SECT}(\nu, t)|^2 \leq \tilde{C}_T^2 \cdot \mathbb{E} \|\text{SECT}(\nu)\|_{\mathcal{H}}^2 < \infty$ for all $(\nu, t) \in \mathbb{S}^{d-1} \times [0, T]$. Then, we define the mean and covariance functions as follows

$$\begin{aligned} m_\nu(t) &= \mathbb{E} \{ \text{SECT}(\nu, t) \} = \int_{\mathcal{S}_{R,d}^M} \text{SECT}(K)(\nu, t) \mathbb{P}(dK), \\ \Xi_\nu(s, t) &= \text{Cov} \left(\text{SECT}(\nu, s), \text{SECT}(\nu, t) \right), \quad \text{for } s, t \in [0, T] \text{ and } \nu \in \mathbb{S}^{d-1}. \end{aligned} \tag{4.3}$$

Lemma C.4 provides several properties of the mean m_ν and covariance Ξ_ν that validate our KL expansion of $\text{SECT}(\nu)$ in Section 5. Additionally, Lemma C.4 demonstrates that the mean $\mathbf{m} \stackrel{\text{def}}{=} \{m_\nu\}_{\nu \in \mathbb{S}^{d-1}}$ of SECT belongs to $C(\mathbb{S}^{d-1}; \mathcal{H})$. A tentative discussion on the “pseudo-inverse” $\text{SECT}^{-1}(\mathbf{m})$ is provided after Lemma C.4 in Appendix C.

In most shape analysis studies, data are preprocessed by alignment. In Appendix E, we introduce the “ECT alignment” as a preprocessing step before any statistical inference. Throughout the manuscript, we assume that the data have been aligned using this method. The ECT alignment exploits rigid motions, does not rely on landmarks, and is equivalent to the alignment approach outlined in Wang et al. (2021) (Supplementary Section 4). The primary objective of the ECT alignment is to minimize the differences between two shapes that arise from rigid motions. For instance, the molars in Figure 1.1 were aligned using the ECT alignment. Furthermore, the ECT alignment is compatible with our SECT framework. Appendix E demonstrates that the ECT alignment does not alter the qualitative properties of SECT (e.g., the measurability, Sobolev-regularity, and $\frac{1}{2}$ -Hölder continuity).

In applications, it is infeasible to sample infinitely many directions $\nu \in \mathbb{S}^{d-1}$ and levels $t \in [0, T]$. For given shapes K , we compute $\text{SECT}(K)(\nu, t)$ for finitely many directions $\{\nu_1, \dots, \nu_\Gamma\} \subseteq \mathbb{S}^{d-1}$ and levels $\{t_1, \dots, t_\Delta\} \subseteq [0, T]$. To retain information about shapes K , one needs to properly set the numbers of directions and levels (i.e., Γ and Δ). From a

theoretical viewpoint, [Curry et al. \(2022\)](#) comprehensively discussed the number Γ of directions needed to recover shapes K from $\text{ECT}(K)$ when K are “piecewise linearly embedded shapes with plausible geometric bounds.” From the numerical perspective, we note the following: (i) [Wang et al. \(2021\)](#) provided detailed simulation studies on the choices of Γ and Δ in sub-image analysis, and a general guideline for setting Γ and Δ in practice was presented in Supplementary Table 1 therein; and (ii) in our Appendix [K](#), we provide detailed numerical experiments on the trade-offs between the choices of Γ and Δ , the statistical power of our proposed algorithms (Algorithms [1](#) and [2](#)), and computational cost.

5 Testing Hypotheses on Shapes

In this section, we apply the probabilistic formulation from Section [4](#) and Lemma [C.4](#) to test hypotheses on shapes. Suppose $\mathbb{P}^{(1)}$ and $\mathbb{P}^{(2)}$ are two distributions on the measurable space $(\mathcal{S}_{R,d}^M, \mathcal{F})$. Let $\mathbb{P}^{(1)} \otimes \mathbb{P}^{(2)}$ be the product probability measure defined on the product σ -algebra $\mathcal{F} \otimes \mathcal{F}$, satisfying $\mathbb{P}^{(1)} \otimes \mathbb{P}^{(2)}(A \times B) = \mathbb{P}^{(1)}(A) \cdot \mathbb{P}^{(2)}(B)$ for all $A, B \in \mathcal{F}$. To address the motivating question from Section [1.1](#), we test the following hypotheses

$$H_0^* : \mathbb{P}^{(1)} = \mathbb{P}^{(2)}, \quad \text{vs.} \quad H_1^* : \mathbb{P}^{(1)} \neq \mathbb{P}^{(2)}, \quad (5.1)$$

e.g., suppose $\mathbb{P}^{(1)}$ and $\mathbb{P}^{(2)}$ model the distributions of molars from two genera of primates ([Figure 1.1](#)). Rejecting the H_0^* in [Eq. \(5.1\)](#) helps distinguish the two genera of primates.

Define $m_\nu^{(j)}(t) = \int_{\mathcal{S}_{R,d}^M} \text{SECT}(K)(\nu, t) \mathbb{P}^{(j)}(dK)$ for $j \in \{1, 2\}$ as the mean functions corresponding to $\mathbb{P}^{(1)}$ and $\mathbb{P}^{(2)}$. To reject the null H_0^* in [Eq. \(5.1\)](#) (equivalently, distinguish two collections of shapes), it suffices to reject the null hypothesis H_0 in the following

$$H_0 : m_\nu^{(1)}(t) = m_\nu^{(2)}(t) \text{ for all } (\nu, t), \quad \text{vs.} \quad H_1 : m_\nu^{(1)}(t) \neq m_\nu^{(2)}(t) \text{ for some } (\nu, t). \quad (5.2)$$

Analysis of Variance for Functional Data (fdANOVA). Considering the hypotheses in Eq. (5.2) for all directions $\nu \in \mathbb{S}^{d-1}$ results in simultaneous multiple-comparisons and inflation of the type I error. To address this issue, we focus on a specific direction, motivated by the observation that the null hypothesis H_0 in Eq. (5.2) is equivalent to $\sup_{\nu \in \mathbb{S}^{d-1}} \{\|m_\nu^{(1)} - m_\nu^{(2)}\|_{\mathcal{B}}\} = 0$. Hence, the direction of interest is defined as

$$\nu^* \stackrel{\text{def}}{=} \operatorname{argmax}_{\nu \in \mathbb{S}^{d-1}} \{\|m_\nu^{(1)} - m_\nu^{(2)}\|_{\mathcal{B}}\}. \quad (5.3)$$

Lemma C.4 and Eq. (2.2) imply $\{m_\nu^{(j)}\}_{j=1}^2 \subseteq \mathcal{B}$ for all ν . Lemma C.4, together with Eq. (2.1), confirms the existence of a maximizer in Eq. (5.3). The maximizer in Eq. (5.3) may not be unique. If there are multiple maximizers, we arbitrarily choose one, as this choice does not influence our framework. The null hypothesis H_0 in Eq. (5.2) is then equivalent to $\|m_{\nu^*}^{(1)} - m_{\nu^*}^{(2)}\|_{\mathcal{B}} = 0$, where the ν^* defined in Eq. (5.3) is called a *distinguishing direction*. Hereafter, we investigate the distribution of $\text{SECT}(\nu^*)$.

Based on the discussion above, testing the hypotheses in Eq. (5.2) is equivalent to testing $m_{\nu^*}^{(1)}(t) = m_{\nu^*}^{(2)}(t)$ for $t \in [0, T]$ using $\text{SECT}(\nu^*)$, which is a fdANOVA problem that has been well-studied in the literature (e.g., Zhang, 2013, Section 5.2). However, many state-of-the-art fdANOVA approaches are incompatible with $\text{SECT}(\nu^*)$. For example, the Gaussianity of $\text{SECT}(\nu^*)$ is not guaranteed (Remark C.1), and the “two-sample problem assumptions” in Section 5.2 of Zhang (2013) may not be satisfied. Besides, the L^2 -norm-based test (Zhang and Chen, 2007) and F-type test (Shen and Faraway, 2004) are not preferred when the functional data are not Gaussian (Zhang, 2013, Chapter 5). Additionally, many fdANOVA methods are time-consuming. For example, tests based on random projections (TRP, Cuesta-Albertos and Febrero-Bande, 2010) require the computation of (at least 30) L^2 -projections for each observed function, followed by the application of appropriate ANOVA tests to these projections. To address the Gaussianity issue and achieve computational

efficiency, we propose a method for fdANOVA using the KL expansion. Our test has a foundation that aligns with the probabilistic framework of $\text{SECT}(\nu^*)$ in Section 4; it is comparable with the existing methods in terms of size and power (see Appendix J); and it is also computationally efficient, allowing for the permutation test used with our method.

Karhunen–Loève Expansion. Let $\Xi_{\nu^*}^{(j)}(s, t)$ be the covariance function of the stochastic process $\text{SECT}(\nu^*)$ corresponding to $\mathbb{P}^{(j)}$, for $j \in \{1, 2\}$ (see Eq. (4.3)). Hereafter, we assume the following, which is true under the null hypothesis $H_0^* : \mathbb{P}^{(1)} = \mathbb{P}^{(2)}$ in Eq. (5.1).

Assumption 3 (Homoscedasticity). $\Xi_{\nu^*} \stackrel{\text{def}}{=} \Xi_{\nu^*}^{(1)} = \Xi_{\nu^*}^{(2)}$, where ν^* is defined in Eq. (5.3).

This is a standard assumption in the fdANOVA literature (e.g., Zhang, 2013, Section 5.2) and can be tested using the methods proposed by Jia Guo and Zhang (2019).

We define an integral operator on $L^2([0, T]^2)$ as $f \mapsto \int_0^T f(s) \cdot \Xi_{\nu^*}(s, \cdot) ds$. This operator is compact and self-adjoint (Hsing and Eubank, 2015, Theorems 4.6.2 and Example 3.3.4). Moreover, the Hilbert-Schmidt theorem (Reed and Simon, 1972, Theorem VI.16) suggests that there is a complete orthonormal basis $\{\phi_l\}_{l=1}^\infty$ for $L^2([0, T])$ so that (i) each ϕ_l is an eigenfunction with eigenvalue λ_l , (ii) $\lambda_1 \geq \lambda_2 \geq \dots \geq 0$, and (iii) $\lim_{l \rightarrow \infty} \lambda_l = 0$. Lemma C.4 and Theorem 7.3.5 of Hsing and Eubank (2015) imply the following KL expansion:

Theorem 5.1 (Karhunen–Loève expansion). (i) For each fixed $j \in \{1, 2\}$, we have

$$\lim_{L \rightarrow \infty} \sup_{t \in [0, T]} \mathbb{E}^{(j)} \left[\text{SECT}(\nu^*, t) - m_{\nu^*}^{(j)}(t) - \sum_{l=1}^L \sqrt{\lambda_l} \cdot Z_l^{(j)} \cdot \phi_l(t) \right]^2 = 0, \quad (5.4)$$

where $Z_l^{(j)}(K) \stackrel{\text{def}}{=} \frac{1}{\sqrt{\lambda_l}} \int_0^T \{\text{SECT}(K)(\nu^*, t) - m_{\nu^*}^{(j)}(t)\} \cdot \phi_l(t) dt$ for $l = 1, 2, \dots$, and $\mathbb{E}^{(j)}$ is the expectation associated with $\mathbb{P}^{(j)}$. For each $j \in \{1, 2\}$, the random variables $\{Z_l^{(j)}\}_{l=1}^\infty$ are defined on the probability space $(\mathcal{S}_{R,d}^M, \mathcal{F}, \mathbb{P}^{(j)})$, are mutually uncorrelated, and have mean

0 and variance 1. (ii) There exists $\mathcal{N} \in \mathcal{F} \otimes \mathcal{F}$ so that $\mathbb{P}^{(1)} \otimes \mathbb{P}^{(2)}(\mathcal{N}) = 0$ and

$$\begin{aligned} \delta_l(K^{(1)}, K^{(2)}) &\stackrel{\text{def}}{=} \frac{1}{\sqrt{2\lambda_l}} \int_0^T \left\{ \text{SECT}(K^{(1)})(\nu^*, t) - \text{SECT}(K^{(2)})(\nu^*, t) \right\} \cdot \phi_l(t) dt \\ &= \theta_l + \left(\frac{Z_l^{(1)}(K^{(1)}) - Z_l^{(2)}(K^{(2)})}{\sqrt{2}} \right), \end{aligned} \quad (5.5)$$

$$\text{where } \theta_l \stackrel{\text{def}}{=} \frac{1}{\sqrt{2\lambda_l}} \int_0^T \left\{ m_{\nu^*}^{(1)}(t) - m_{\nu^*}^{(2)}(t) \right\} \cdot \phi_l(t) dt,$$

for any $(K^{(1)}, K^{(2)}) \notin \mathcal{N}$ and each fixed $l = 1, 2, \dots$. The null set \mathcal{N} is allowed to be empty.

Using the KL expansion in Eq. (5.4), the random sampling of shapes may be considered, which is discussed in Appendix M.1 and left for future research.

Our Approach. Consider two independent collections of random shapes $\{K_i^{(j)}\}_{i=1}^n \stackrel{\text{i.i.d.}}{\sim} \mathbb{P}^{(j)}$, for $j \in \{1, 2\}$ (i.e., $\{(K_i^{(1)}, K_i^{(2)})\}_{i=1}^n \stackrel{\text{i.i.d.}}{\sim} \mathbb{P}^{(1)} \otimes \mathbb{P}^{(2)}$). The pairing in $(K_i^{(1)}, K_i^{(2)})$ is arbitrary for the following reasons: (i) pairs $(K_i^{(1)}, K_i^{(2)})$ and $(K_{i'}^{(1)}, K_{i'}^{(2)})$ with $i \neq i'$ have the same distribution $\mathbb{P}^{(1)} \otimes \mathbb{P}^{(2)}$, and (ii) numerical experiments in Sections 6 and 7 demonstrate that the performance of our proposed algorithms is numerically invariant to shuffling the index i within each collection $\{K_i^{(j)}\}_{i=1}^n$. Without loss of generality, we assume that all the shapes have been aligned using the ‘‘ECT alignment’’ (Appendix E). Here, we present the theoretical foundation for employing $\{(K_i^{(1)}, K_i^{(2)})\}_{i=1}^n$ to test the hypotheses in Eq. (5.2). This foundation helps address the motivating question from Section 1.1.

Without loss of generality, we assume $(K_i^{(1)}, K_i^{(2)}) \notin \mathcal{N}$, for all $i = 1, 2, \dots, n$, where \mathcal{N} is the null set in Theorem 5.1 satisfying $\mathbb{P}^{(1)} \otimes \mathbb{P}^{(2)}(\mathcal{N}) = 0$. Then, we have

$$\xi_{l,i} \stackrel{\text{def}}{=} \delta_l(K_i^{(1)}, K_i^{(2)}) = \theta_l + \left(\frac{Z_l^{(1)}(K_i^{(1)}) - Z_l^{(2)}(K_i^{(2)})}{\sqrt{2}} \right), \quad (5.6)$$

where δ_l and θ_l are defined in Eq. (5.5). Theorem 5.1 implies that, for each fixed l , the random variables $\{\xi_{l,i}\}_{i=1}^n$ are i.i.d. across $i = 1, \dots, n$ with mean θ_l and variance 1; for each fixed i , the random variables $\{\xi_{l,i}\}_{l=1}^\infty$ are mutually uncorrelated across $l = 1, 2, 3, \dots$.

The following lemma represents the null H_0 in Eq. (5.2) using the means $\{\theta_l\}_{l=1}^\infty$.

Lemma 5.1. *The null H_0 in Eq. (5.2) is equivalent to $\theta_l = 0$ for all positive integers l .*

Recall that $\lim_{l \rightarrow \infty} \lambda_l = 0$. When eigenvalues λ_l in the denominator of Eq. (5.5) are close to zero for large l , the estimated θ_l becomes unstable. Specifically, even if $m_{\nu^*}^{(1)}(t) \approx m_{\nu^*}^{(2)}(t)$, an extremely small λ_l can move the corresponding estimated θ_l far away from zero. Using the standard approach in principal component analysis, we focus on $\{\theta_l\}_{l=1}^L$ with

$$L \stackrel{\text{def}}{=} \max\{1, \tilde{L}\}, \quad \text{where } \tilde{L} \stackrel{\text{def}}{=} \min \left\{ l \in \mathbb{N} \mid \frac{\sum_{l'=1}^l \lambda_{l'}}{\sum_{l''=1}^{\infty} \lambda_{l''}} > 0.95 \right\}. \quad (5.7)$$

Hence, to test the hypotheses in Eq. (5.2) via Lemma 5.1, we test the following

$$\widehat{H}_0 : \theta_1 = \cdots = \theta_L = 0, \quad \text{vs.} \quad \widehat{H}_1 : \text{there exists } l' \in \{1, \dots, L\} \text{ such that } \theta_{l'} \neq 0. \quad (5.8)$$

Under the null \widehat{H}_0 in Eq. (5.8), for each $l \in \{1, \dots, L\}$, the central limit theorem indicates that $\frac{1}{\sqrt{n}} \sum_{i=1}^n \xi_{l,i}$ is asymptotically $N(0, 1)$ when n is large. The mutual uncorrelation in Theorem 5.1 and the asymptotic normality of $\frac{1}{\sqrt{n}} \sum_{i=1}^n \xi_{l,i}$ provide the asymptotic independence of $\{\frac{1}{\sqrt{n}} \sum_{i=1}^n \xi_{l,i}\}_{l=1}^L$ across $l = 1, \dots, L$. Then, $\sum_{l=1}^L (\frac{1}{\sqrt{n}} \sum_{i=1}^n \xi_{l,i})^2$ is asymptotically χ_L^2 under the \widehat{H}_0 in Eq. (5.8). At the asymptotic significance $\alpha \in (0, 1)$, we reject the \widehat{H}_0 if

$$\sum_{l=1}^L \left(\frac{1}{\sqrt{n}} \sum_{i=1}^n \xi_{l,i} \right)^2 > \chi_{L,1-\alpha}^2 = \text{the } 1 - \alpha \text{ lower quantile of the } \chi_L^2 \text{ distribution.} \quad (5.9)$$

In applications, neither the mean $m_{\nu}^{(j)}(t)$ nor the covariance $\Xi_{\nu}(s, t)$ is known. Hence, the KL expansions in Eq. (5.5) cannot be directly used and must be estimated. In Appendix F, we propose a numerical foundation for conducting the asymptotic χ^2 -test in Eq. (5.9) and encapsulate the numerical procedures for the test in **Algorithm 1**. In all our analyses in Sections 6 and 7, the numerical estimates \widehat{L} (see Eq. (F.4) in Appendix F) of the L in Eq. (5.7) are smaller than 10. When the \widehat{L} values are large (e.g., several hundred), one may also consider applying the adaptive Neyman test proposed by Fan (1996).

In the simulation studies presented in Tables 6.1 and J.1, our Algorithm 1 has comparable performance with more than ten existing state-of-the-art fdANOVA methods. Nonethe-

less, both Algorithm 1 and the existing methods exhibit type I error inflation (e.g., the rejection rate of Algorithm 1 is 0.118, whereas the significance is 0.05). To mitigate this inflation, we may consider applying the permutation test using one of these methods that is computationally efficient. For example, Górecki and Smaga (2015) proposed a permutation test based on an F-type statistic (FP). Specifically, Górecki and Smaga (2015) approximated each observed function by basis functions via information criteria, and the F-type statistic was approximated by a form conducive to efficiently computing permutation-based p-values. However, the FP also exhibits type I error inflation (see Tables 6.1 and J.1). Motivated by the FP, we apply the permutation test to the χ^2 -statistic defined in Eq. (5.9) in the following way: we first apply Algorithm 1 to our original shapes $K_i^{(j)}$ and then repeatedly re-apply Algorithm 1 to the shapes with shuffled group labels j . The χ^2 -test statistic derived from the original data is then compared to that from the shuffled data. A detailed description of our permutation-based approach is presented in Algorithm 2 in Appendix F. Simulations in Section 6 demonstrate that our permutation-based approach eliminates the type I error inflation encountered by Algorithm 1. The permutation nature of Algorithm 2 is also advantageous for small sample sizes. Note, however, that the power of Algorithm 2 under the alternative is moderately weaker than that of Algorithm 1. Lastly, the runtimes of Algorithms 1 and 2, when applied to simulations, are studied in Appendix K. We present the runtimes when applying the algorithms to real data in Table 7.1.

6 Experiments Using Simulations

We present simulations showing the performance of our Algorithms 1 and 2. In addition, we compare our algorithms with the “randomization-style null hypothesis significance test (NHST)” (Robinson and Turner, 2017), the TRP using Wald-type permutation statistic

(TRP-WTPS, [Cuesta-Albertos and Febrero-Bande, 2010](#); [Pauly et al., 2014](#)), and the FP. Details of the randomization-style NHST are given in [Appendix G](#) and referred to as [Algorithm 3](#). The application of the FP and TRP to the SECT is described in [Section 5](#). We implement the FP and TRP-WTPS using the R package `fdANOVA` with its default parameters as recommended by [Górecki and Smaga \(2019\)](#). Additional simulations comparing our proposed algorithms and other existing `fdANOVA` methods are presented in [Appendix J](#).

We focus on a family of distributions $\{\mathbb{P}^{(\varepsilon)}\}_{0 \leq \varepsilon \leq 0.1}$ with shapes $\{K_i^{(\varepsilon)}\}_{i=1}^n \stackrel{\text{i.i.d.}}{\sim} \mathbb{P}^{(\varepsilon)}$ via

$$K_i^{(\varepsilon)} \stackrel{\text{def}}{=} \left\{ x \in \mathbb{R}^2 \left| \inf_{y \in S_i^{(\varepsilon)}} \|x - y\| \leq 0.2 \right. \right\}, \quad \text{where} \quad (6.1)$$

$$S_i^{(\varepsilon)} \stackrel{\text{def}}{=} \left\{ \left(\frac{2}{5} + a_{1,i} \cdot \cos t, b_{1,i} \cdot \sin t \right) \left| \frac{1-\varepsilon}{5}\pi \leq t \leq \frac{9+\varepsilon}{5}\pi \right. \right\} \cup \left\{ \left(-\frac{2}{5} + a_{2,i} \cdot \cos t, b_{2,i} \cdot \sin t \right) \left| \frac{6\pi}{5} \leq t \leq \frac{14\pi}{5} \right. \right\}$$

and $\{a_{1,i}, a_{2,i}, b_{1,i}, b_{2,i}\}_{i=1}^n \stackrel{\text{i.i.d.}}{\sim} N(1, 0.05^2)$. The ε denotes the dissimilarity between $\mathbb{P}^{(\varepsilon)}$ and $\mathbb{P}^{(0)}$. For each $\varepsilon \in [0, 0.1]$, through the discussion in [Section 5](#), we test the following hypotheses via `fdANOVA` methods (i.e., FP, TRP-WTPS, [Algorithms 1](#), and [2](#))

$$H_0 : m_\nu^{(0)}(t) = m_\nu^{(\varepsilon)}(t) \text{ for all } (\nu, t) \in \mathbb{S}^{d-1} \times [0, T] \quad \text{vs.} \quad H_1 : m_\nu^{(0)}(t) \neq m_\nu^{(\varepsilon)}(t) \text{ for some } (\nu, t),$$

where the mean $m_\nu^{(\varepsilon)}(t) \stackrel{\text{def}}{=} \int_{\mathcal{S}_{R,d}^M} \text{SECT}(K)(\nu, t) \mathbb{P}^{(\varepsilon)}(dK)$, and the null hypothesis H_0 is true when $\varepsilon = 0$. We also test $H_0^* : \mathbb{P}^{(0)} = \mathbb{P}^{(\varepsilon)}$ vs. $\mathbb{P}^{(0)} \neq \mathbb{P}^{(\varepsilon)}$ using [Algorithm 3](#).

We set $T = 3$, directions $\nu_p = (\cos \frac{p-1}{4}\pi, \sin \frac{p-1}{4}\pi)^\top$ for $p \in \{1, 2, 3, 4\}$, levels $t_q = \frac{T}{50}q$ for $q \in \{1, \dots, 50\}$ (i.e., $\Gamma = 4$ and $\Delta = 50$ in [Algorithms 1](#), [2](#), and [3](#)), the confidence level 95% (i.e., $\alpha = 0.05$), and the number of permutations $\Pi = 1000$. For each $\varepsilon \in \{0, 0.01, 0.02, 0.03, 0.04, 0.05, 0.06, 0.08, 0.1\}$, we independently generate two collections $\{K_i^{(0)}\}_{i=1}^n \stackrel{\text{i.i.d.}}{\sim} \mathbb{P}^{(0)}$ and $\{K_i^{(\varepsilon)}\}_{i=1}^n \stackrel{\text{i.i.d.}}{\sim} \mathbb{P}^{(\varepsilon)}$ through [Eq \(6.1\)](#) with the number of shape pairs set to $n = 100$, and we compute the SECT of each generated shape in directions $\{\nu_p\}_{p=1}^4$ and at levels $\{t_q\}_{q=1}^{50}$. We then implement the `fdANOVA` methods and [Algorithm 3](#) to these computed SECT statistics and get the corresponding `Accept/Reject` outputs. We repeat

this procedure 1000 times and report the rejection rates across all 1000 replicates for each ε in Table 6.1. The rejection rates are also visually presented in Figure 6.1. We choose $\Gamma = 4$ as the number of directions in our simulations based on the following observation: in Appendix K, we experiment with all combinations of $\Gamma \in \{2, 4, 8\}$, $\Delta \in \{25, 50, 100\}$, and $n \in \{25, 50, 100\}$. When $\Delta = 50$ and $n = 100$, the number $\Gamma = 4$ is sufficiently large for our Algorithms 1 and 2 to distinguish $\mathbb{P}^{(0)}$ from $\mathbb{P}^{(\varepsilon)}$ with $\varepsilon > 0$ using the significance level $\alpha = 0.05$. Moreover, this choice allows us to demonstrate that even a relatively small number of directions (e.g., $\Gamma = 4$) is sufficient for implementing our Algorithm 1 and 2.

Table 6.1: Rejection rates (from 1000 experiments) for different indices ε (significance $\alpha = 0.05$). Appendix J provides a comparison of Algorithms 1, 2, and 3 to other existing fdANOVA methods.

Indices ε	0.00	0.01	0.02	0.03	0.04	0.05	0.06	0.08	0.10
Algorithm 1	0.118	0.161	0.315	0.519	0.785	0.910	0.975	0.990	1.000
Algorithm 2	0.046	0.054	0.162	0.343	0.612	0.789	0.931	0.994	1.000
Algorithm 3	0.050	0.050	0.111	0.185	0.335	0.535	0.739	0.983	0.999
FP	0.136	0.153	0.308	0.539	0.810	0.924	0.986	0.997	1.000
TRP-WTPS	0.075	0.091	0.261	0.515	0.790	0.929	0.980	0.997	1.000

The results in Table 6.1 and Figure 6.1 demonstrate that our proposed algorithms are effective at detecting the difference between $\mathbb{P}^{(\varepsilon)}$ and $\mathbb{P}^{(0)}$ in terms of distinguishing their mean functions. Notably, our algorithms (especially Algorithm 2) tend to avoid falsely detecting differences between shape-generating distributions under the null hypothesis (i.e., $\varepsilon = 0$). As ε increases, $\mathbb{P}^{(\varepsilon)}$ deviates from $\mathbb{P}^{(0)}$, and the power of our algorithms in detecting the deviation increases. When $\varepsilon \geq 0.08$, the power of Algorithms 1 and 2 exceeds 0.99. For all the ε , it is difficult to see the deviation of $\mathbb{P}^{(\varepsilon)}$ from $\mathbb{P}^{(0)}$ visually. For instance, by merely observing the shapes in Figure 6.1, one might find it hard to differentiate between the shape collections generated by $\mathbb{P}^{(0)}$ (blue) and $\mathbb{P}^{(0.08)}$ (pink). However, in more than

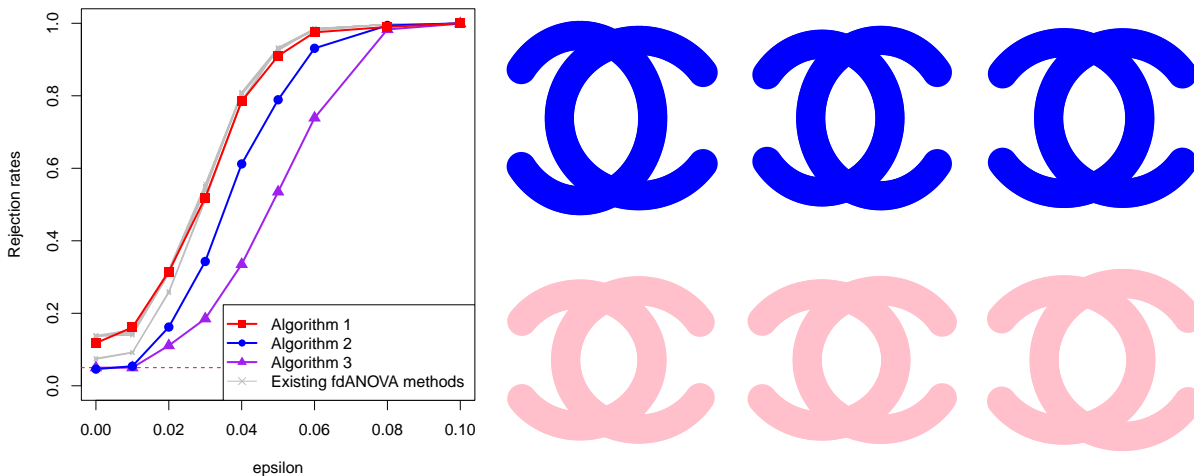


Figure 6.1: (Left panel) The relationship between ε and the rejection rates computed via Algorithms 1, 2, 3 (see Table 6.1), and twelve existing fdANOVA methods (see Table J.1 in Appendix J for details on the existing fdANOVA methods). The (red) dashed line presents the significance level $\alpha = 0.05$. (Right panel) The shapes in the first row are from $\mathbb{P}^{(0)}$, and the shapes in the second row are from $\mathbb{P}^{(0.08)}$.

99% of the simulations, our algorithms detect the difference between the two distributions. We also randomly shuffle the index i within each collection $\{K_i^{(\varepsilon)}\}_{i=1}^n$ and apply Algorithms 1 and 2 to the shuffled collections. The results obtained from the unshuffled and shuffled shape collections, respectively, are nearly identical. Algorithm 3 performs well in detecting the discrepancy between $\mathbb{P}^{(0)}$ and $\mathbb{P}^{(\varepsilon)}$. However, its power under the alternative hypotheses (i.e., $\varepsilon > 0$) is weaker than that of our Algorithms 1 and 2. Moreover, Algorithms 1 and 2 exhibit performance comparable to twelve existing state-of-the-art fdANOVA methods (see Table 6.1, Figure 6.1, and Table J.1 in Appendix J).

7 Applications

We first apply our proposed Algorithms 1 and 2 to the MPEG-7 shape silhouette database (Sikora, 2001) as a toy example. Details of this are provided in Appendix I. This analysis shows that our proposed algorithms can distinguish between shape classes in the silhouette

database and do not falsely identify signals when there are no differences between groups.

In this section, we apply our algorithms to address the motivating question in Section 1.1. Specifically, we utilize Algorithms 1 and 2 to distinguish between the four categories of mandibular molars in Figure 1.1 that are from four genera of primates. The shapes in Figure 1.1 come from two suborders of primates: Haplorhini and Strepsirrhini (see Figure 1.1). In the haplorhine suborder collection, 29 molars came from the genus *Tarsius* (yellow panels in Figure 1.1), and 9 molars came from the genus *Saimiri* (grey panels in Figure 1.1). In the strepsirrhine collection, 11 molars came from the genus *Microcebus* (blue panels in Figure 1.1), and 6 molars came from the genus *Mirza* (green panels in Figure 1.1).

Before applying Algorithms 1 and 2, we preprocess the raw triangle mesh data of the surfaces of the molars by aligning them through the ECT alignment approach detailed in Appendix E. The aligned molars are presented in Figure 1.1. We apply our Algorithms 1 and 2 to the preprocessed molars. For each aligned molar, we compute its SECT for 2918 directions; in each direction, we use 200 sublevel sets. To compare any pair of molar groups, as a proof of concept, we select the smaller size of the two groups as the sample size input n in our algorithms. For example, when comparing the *Tarsius* and *Microcebus* groups, we choose $n = 11$; that is, we compare the first 11 molars of the *Tarsius* group to all the molars in the *Microcebus* group. We apply our algorithms to the four groups of molars and present the results in Table 7.1. The p-values in Table 7.1 are either χ^2 -test p-values (Algorithm 1) or permutation-test p-values (Algorithm 2 with 1000 permutations). The small p-values ($P < 0.05$) in Table 7.1 show that our proposed algorithms can distinguish the four different genera of primates. Since the genera *Microcebus* and *Mirza* belong to the same suborder Strepsirrhini (see Figure 1.1), the p-value from Algorithm 2 is comparatively large when comparing molars from these two groups. In comparison, although the *Tarsius* and *Saimiri* both belong to the suborder Haplorhini, the molars of the two genera look

different. Specifically, the paraconids (i.e., the cusp highlighted in red in Figure 1.1) are only retained by the genus *Tarsius* and, thus, are a key reason for the small p-values ($P < 10^{-3}$) when comparing with molars from the *Saimiri*. Other small p-values ($P < 10^{-3}$) in our analyses are a result of the corresponding genera belonging to different suborders.

Table 7.1: P-values of Algorithms 1, 2, and 4 for the data set of mandibular molars. In the last row, we present the overall runtime for conducting all hypothesis testing tasks using each algorithm.

	Algorithm 1	Algorithm 2	Algorithm 4
<i>Tarsius</i> vs. <i>Microcebus</i>	$< 10^{-3}$	$< 10^{-3}$	$< 10^{-3}$
<i>Tarsius</i> vs. <i>Mirza</i>	$< 10^{-3}$	$< 10^{-3}$	0.001
<i>Tarsius</i> vs. <i>Saimiri</i>	$< 10^{-3}$	$< 10^{-3}$	$< 10^{-3}$
<i>Microcebus</i> vs. <i>Mirza</i>	$< 10^{-3}$	0.009	0.004
<i>Microcebus</i> vs. <i>Saimiri</i>	$< 10^{-3}$	$< 10^{-3}$	$< 10^{-3}$
<i>Mirza</i> vs. <i>Saimiri</i>	$< 10^{-3}$	$< 10^{-3}$	$< 10^{-3}$
<i>Tarsius</i> vs. <i>Tarsius</i>	0.196 (0.220)	0.496 (0.294)	0.527 (0.273)
Overall runtimes (in hours)	≈ 3	≈ 3	≈ 20

In addition to testing the difference between genera, we apply our algorithms within the genus *Tarsius*. Specifically, we focus on the first 28 molars in the *Tarsius* group. We randomly split the 28 molars into two halves and apply Algorithms 1 and 2 to test the difference between the two halves. We repeat the random splitting procedure 100 times and present the corresponding p-values in Table 7.1. The results are summarized by their mean and standard deviation (in parentheses). These p-values show that our proposed Algorithm 2 tends to avoid the type I error for the molars from the genus *Tarsius*.

Landmark methods are widely used in geometric morphometrics. One state-of-the-art approach is the ‘‘Gaussian process landmarking (GPL)’’ algorithm (Gao et al., 2019a,b) which can automatically sample landmarks on the surfaces of the molars in Figure 1.1. Gao et al. (2019a) showed that these sampled landmarks could induce a continuous Pro-

crustes distance to measure the dissimilarity between molars. A permutation test can be derived using the Procrustes distance induced by the GPL algorithm. This test is detailed in Appendix H and is encapsulated by Algorithm 4. We use the GPL-based Algorithm 4 to differentiate the four collections of molars. For this, we utilize the MATLAB code from the GitHub repository provided by Gao et al. (2019a) to compute the Procrustes distance. Performance of Algorithm 4 is in Table 7.1, which shows that the GPL-based method and our Algorithm 2 have comparable performance. However, repeatedly computing the Procrustes distance is time-consuming. Hence, Algorithm 2 is more computationally efficient than Algorithm 4 while achieving similar performance (see the last row of Table 7.1).

We want to note that, in addition to the GPL algorithm, many other existing methods can be applied to measure dissimilarity between molars, including parameterized surfaces (Kurtek et al., 2010, 2011) and the approaches from computational anatomy (Grenander and Miller, 1998). Similarly, the parameterized curves (Kurtek et al., 2012) can also be used to analyze the silhouette database in Appendix I. An even more comprehensive comparison of our algorithms with the entire edifice of existing methods is left for future research.

8 Conclusions and Discussions

In this paper, we established the mathematical foundations for the randomness of shapes via the SECT. Specifically, (i) $(\mathcal{S}_{R,d}^M, \mathcal{B}(\rho), \mathbb{P})$ was constructed as the underlying probability space; (ii) the SECT was modeled as a $C(\mathbb{S}^{d-1}; \mathcal{H})$ -valued random variable. We further demonstrated several properties of the SECT ensuring its KL expansion, which led to a χ^2 -statistic for testing hypotheses on random shapes. We bridged the fdANOVA and TDA. Simulation studies corroborated our mathematical derivations and showed the performance of our hypothesis testing algorithms. Our approach was shown to be powerful in detecting

the difference between two shape-generating distributions. We applied our proposed algorithms to silhouette and primate molar datasets. Importantly, our simulations when $\varepsilon = 0$, together with the applications to the molars and the silhouette database, indicate that our algorithms tend to avoid falsely detecting differences between shape-generating distributions when there are none. Using the molars in Figure 1.1, we compared the performance of our algorithms to a permutation test based on a state-of-the-art landmarking algorithm (Gao et al., 2019a,b), underscoring the efficiency of our algorithms. We enumerate potential future research areas in Appendix M, e.g., the fdANOVA methods can be utilized for functional connectivity (Chen et al., 2024; Meng and Eloyan, 2024) via topological summaries.

Software Availability

The source code for implementing the simulation studies and applications is publicly available online at <https://github.com/JinyuWang123/TDA.git>.

Acknowledgments

We are grateful to the Editor, Associate Editor, and three Referees of the *Journal of the American Statistical Association* for their thorough review of our article and the insightful suggestions that have tremendously improved its quality. We want to thank Dr. Matthew T. Harrison from the Division of Applied Mathematics at Brown University for useful comments and suggestions. KM wants to thank Mattie Ji from the Department of Mathematics at Brown University for her insightful comments. LC would like to acknowledge the support of a David & Lucile Packard Fellowship for Science and Engineering. Research

reported in this publication was partially supported by the National Institute On Aging of the National Institutes of Health under Award Number R01AG075511. The content is solely the responsibility of the authors and does not necessarily represent the official views of the National Institutes of Health.

Disclosure Statement

The authors report there are no competing interests to declare.

Appendix

Contents

1	Introduction	2
1.1	A Motivating Scientific Question	2
1.2	Overview of Shape and Topological Data Analysis	4
1.3	Overview of Contributions and Paper Organization	7
2	Notations and Mathematical Preparations	9
3	Smooth Euler Characteristic Transform	11
4	Probabilistic Distributions over the SECT	16
5	Testing Hypotheses on Shapes	19
6	Experiments Using Simulations	24
7	Applications	27
8	Conclusions and Discussions	30
A	Mathematical Remarks	37
A.1	Remark on $H_0^1([0, T])$ vs. $H_0^1((0, T))$	37
A.2	Homeomorphism Critical Points	38
A.3	O-minimal Structures	38
B	Overview of Persistence Diagrams	39
B.1	Definition of Persistence Diagrams	39

B.2	Eq. (3.4) in the definition of $\mathcal{S}_{R,d}^M$	42
B.3	Bottleneck Stability	42
C	Additional Theorems	43
D	Proof-of-Concept Simulation Examples	48
D.1	Proof-of-Concept Simulation Examples I: Deterministic Shapes	48
D.2	Proof-of-Concept Simulation Examples II: Random Shapes	51
D.3	Computation of SECT	53
E	Alignment	57
E.1	Motivation	57
E.2	ECT Alignment	58
F	Numerical Foundation for Hypothesis Testing	59
G	Randomization-style Null Hypothesis	
	Significance Test	63
H	Landmark-based Permutation Test	63
H.1	Permutation Test Using Landmark-based Distances	65
H.2	Gaussian Process-based Landmarks and Correspondence	65
H.2.1	Gaussian process landmarking algorithm	65
H.2.2	Procrustes distance induced by the Gaussian Process-based Landmarks and Correspondence	66
I	Applications to Silhouette Database	67
J	Numerical Experiments on the ANOVA for Functional Data — Existing	

Methods vs. Our Proposed Methods	69
K Trade-off Studies for Algorithms 1 and 2 — Numbers of Directions and Levels, Sample Sizes, and Computational Cost	70
L Proofs	75
L.1 Proof of Theorem C.1	75
L.2 An Elementary Proof of Eq. (2.1)	76
L.3 Proof of Theorem C.2	78
L.4 Proof of Lemma C.3	79
L.5 Proof of Eq. (C.1)	80
L.6 Proof of Theorem 3.2	83
L.7 Proof of Lemma C.2	84
L.8 Proof of Eq. (C.2)	84
L.9 Proof of Theorem 3.3	86
L.10 Proof of Theorem 4.1	86
L.11 Proof of Lemma 4.1	88
L.12 Proof of Lemma C.4	88
L.13 Proof of Theorem 5.1	90
L.14 Proof of Lemma 5.1	92
L.15 Proof of Theorem C.5	92
M Potential Future Research Areas	93
M.1 Generative Models for Complex Shapes	93
M.2 Definition of Mean Shapes	94

M.3 Two-sample Test via the Reproducing Kernel Hilbert Space embedding or Optimal Transport	94
M.4 Euler Characteristic-based Statistical Inference on Grayscale Images: The- ory and Applications	95
M.5 Euler Characteristic-based Topological Data Analysis	96

A Mathematical Remarks

In this section, we provide some mathematical remarks.

A.1 Remark on $H_0^1([0, T])$ vs. $H_0^1((0, T))$

Strictly speaking, the functions in Sobolev space \mathcal{H} are defined on the open interval $(0, T)$ instead of the closed interval $[0, T]$ (Brezis, 2011, Chapter 8.2). Hence, the rigorous notation of \mathcal{H} should be $H_0^1((0, T))$. However, Theorem 8.8 of Brezis (2011) indicates that each function in $H_0^1((0, T))$ can be uniquely represented by a continuous function defined on the closed interval $[0, T]$, which implies that functions in $H_0^1((0, T))$ can be viewed as being defined on the closed interval $[0, T]$. Therefore, to implement the boundary values on $\partial(0, T) = \{0, T\}$, we use the notation $H_0^1([0, T])$ throughout this paper to indicate that all functions in \mathcal{H} are viewed as defined on $[0, T]$. The same reasoning is also applied for the space $W_0^{1,p}([0, T])$ implemented in Appendix C (also see Brezis, 2011, Theorem 8.8 and Remark 8 after Proposition 8.3).

Notably, $\mathcal{H} = H_0^1([0, T])$ is the RKHS generated by the kernel $\kappa(s, t) = \min\{s, t\} - \frac{st}{T}$ (Lifshits, 2012, Example 4.9).

Sobolev spaces have traditionally been used to study partial differential equations (Lu, 1996; Hadac et al., 2009; Li and Meng, 2016; Lv et al., 2019; Wei and Zhang, 2021). In statistics, the Sobolev spaces most commonly used are those that are also RKHSs (Duchon, 1977; Wahba, 1990). Hairer (2009) offers a detailed exploration of the relationship between Sobolev spaces and RKHSs through Gaussian measures, noting that RKHSs can be broadly understood as equivalent to compact Sobolev embeddings.

A.2 Homeomorphism Critical Points

To introduce the concept of *homeomorphism critical points* (HCPs), we need the following lemma

Lemma A.1. *For any $K \in \mathcal{S}_{R,d}^M$ and any direction $\nu \in \mathbb{S}^{d-1}$, the homeomorphism type of K_t^ν can only change finitely many times as a function of t .*

Lemma A.1 is a direct consequence of Lemma 3.4 from Curry et al. (2022); hence, its proof is omitted.

For clarity of the presentation in the rest of the Appendix, we define the HCPs as follows:

For any $K \in \mathcal{S}_{R,d}^M$ and any direction $\nu \in \mathbb{S}^{d-1}$, each value of t where the homeomorphism type of K_t^ν changes is called an HCP of K in direction ν .

Lemma A.1 implies that there are only finitely many HCPs of K in each direction. Furthermore, due to the homeomorphic invariance of the Euler characteristic and Betti numbers, Lemma A.1 implies that the functions $t \mapsto \beta_k(K_t^\nu)$ and $t \mapsto \chi(K_t^\nu)$ are piecewise constant functions. The discontinuities of these functions are HCPs in direction ν .

A.3 O-minimal Structures

The definition of o-minimal structures is available in van den Dries (1998) and rephrased as follows.

Definition A.1 (van den Dries (1998)). *An o-minimal structure is a sequence $\mathcal{S} = \{\mathcal{S}_n\}_{n \geq 1}$ satisfying the following:*

- i) for each n , \mathcal{S}_n is a Boolean algebra of subsets of \mathbb{R}^n ;*
- ii) $A \in \mathcal{S}_n$ implies $A \times \mathbb{R} \in \mathcal{S}_{n+1}$ and $\mathbb{R} \times A \in \mathcal{S}_{n+1}$;*
- iii) $\{(x_1, \dots, x_n) \in \mathbb{R}^n \mid x_i = x_j\} \in \mathcal{S}_n$ for all $1 \leq i < j \leq n$;*

- iv) $A \in \mathcal{S}_{n+1}$ implies $\pi(A) \in \mathcal{S}_n$, where $\pi : \mathbb{R}^{n+1} \rightarrow \mathbb{R}^n$ is the usual projection map;
- v) $\{r\} \in \mathcal{S}_1$ for all $r \in \mathbb{R}$, and $\{(x, y) \in \mathbb{R}^2 \mid x < y\} \in \mathcal{S}_2$; and
- vi) the only sets in \mathcal{S}_1 are the finite unions of open intervals (with $\pm\infty$ endpoints allowed) and points.

B Overview of Persistence Diagrams

In Appendix B, we provide an overview of PDs in the literature. The overview is provided for the following purposes:

- We provide the details of the definition of $\mathcal{S}_{R,d}^M$, particularly Condition 3.1.
- The PD framework is the necessary tool for several proofs in Appendix L.

Most of the materials in the overview come from or are modified from Mileyko et al. (2011) and Turner (2013).

B.1 Definition of Persistence Diagrams

Let \mathbb{K} be a compact topological space and φ be a real-valued continuous function defined on \mathbb{K} . Because of the compactness of \mathbb{K} and continuity of φ , we assume $\varphi(\mathbb{K}) \subseteq [0, T]$ without loss of generality. For each $t \in [0, T]$, denote

$$\mathbb{K}_t^\varphi \stackrel{\text{def}}{=} \{x \in \mathbb{K} \mid \varphi(x) \leq t\}.$$

Then $\mathbb{K}_{t_1}^\varphi \subseteq \mathbb{K}_{t_2}^\varphi$ for all $0 \leq t_1 \leq t_2 \leq T$, and $i_{t_1 \rightarrow t_2}$ denotes the corresponding inclusion map. Hereafter, we assume the following

Assumption 4. \mathbb{K}_t^φ falls into finitely many homeomorphism types as t ranges over $[0, T]$.

If we take $\mathbb{K} = K \in \mathcal{S}_{R,d}^M$ and

$$\varphi(x) = x \cdot \nu + R \stackrel{\text{def}}{=} \phi_\nu(x), \quad x \in K, \quad \nu \in \mathbb{S}^{d-1}, \quad (\text{B.1})$$

we have the scenario discussed in Section 3. Lemma A.1 implies that Assumption 4 is satisfied by ϕ_ν for every $\nu \in \mathbb{S}^{d-1}$.

The inclusion maps $i_{t_1 \rightarrow t_2}^\varphi : \mathbb{K}_{t_1}^\varphi \rightarrow \mathbb{K}_{t_2}^\varphi$ induces the group homomorphisms

$$i_{t_1 \rightarrow t_2}^\# : H_k(\mathbb{K}_{t_1}^\varphi) \rightarrow H_k(\mathbb{K}_{t_2}^\varphi), \quad \text{for all } k \in \mathbb{Z},$$

where $H_k(\cdot) = H_k(\cdot; \mathbb{Z}_2)$ denotes the k -th homology group with respect to field \mathbb{Z}_2 , and \mathbb{Z}_2 is omitted for succinctness. Under Assumption 4, for any $t_1 \leq t_2$, we have that the image

$$\text{im} \left(i_{(t_1-\delta) \rightarrow t_2}^\# \right) = \text{im} \left(i_{(t_1-\delta) \rightarrow t_1}^\# \circ i_{t_1 \rightarrow t_2}^\# \right)$$

does not depend on $\delta > 0$ when δ is sufficiently small, and then this constant image is denoted as $\text{im}(i_{(t_1-)\rightarrow t_2}^\#)$. For any t , the k -th *birth group* at t is defined as the quotient group

$$B_k^t \stackrel{\text{def}}{=} H_k(\mathbb{K}_t^\varphi) / \text{im}(i_{(t-)\rightarrow t}^\#),$$

and $\pi_{B_k^t} : H_k(\mathbb{K}_t^\varphi) \rightarrow B_k^t$ denotes the corresponding quotient map. For any $\alpha \in H_k(\mathbb{K}_t^\varphi)$, we say α is born at t if $\pi_{B_k^t}(\alpha) \neq 0$ in B_k^t . Assumption 4 implies that B_k^t is a nontrivial group only for finitely many t . For any $t_1 < t_2$, we denote the quotient group

$$E_k^{t_1, t_2} \stackrel{\text{def}}{=} H_k(\mathbb{K}_{t_2}^\varphi) / \text{im}(i_{(t_1-)\rightarrow t_2}^\#)$$

and the corresponding quotient map $\pi_{E_k^{t_1, t_2}} : H_k(\mathbb{K}_{t_2}^\varphi) \rightarrow E_k^{t_1, t_2}$. Furthermore, we define the following map

$$g_k^{t_1, t_2} : B_k^{t_1} \rightarrow E_k^{t_1, t_2}, \quad \pi_{B_k^{t_1}}(\alpha) \mapsto \pi_{E_k^{t_1, t_2}} \left(i_{t_1 \rightarrow t_2}^\#(\alpha) \right),$$

for all $\alpha \in H_k(\mathbb{K}_{t_1}^\varphi)$. Then, we define the *death group*

$$D_k^{t_1, t_2} \stackrel{\text{def}}{=} \ker(g_k^{t_1, t_2}).$$

We say a homology class $\alpha \in H_k(\mathbb{K}_{t_1}^\varphi)$ is born at t_1 and dies at t_2 if

- i) $\pi_{B_k^{t_1}}(\alpha) \neq 0$,
- ii) $\pi_{B_k^{t_1}}(\alpha) \in D_k^{t_1, t_2}$, and
- iii) $\pi_{B_k^{t_1}}(\alpha) \notin D_k^{t_1, t_2 - \delta}$ for any $\delta \in (0, t_2 - t_1)$.

If α does not die, we artificially say that it dies at T as $K_T^\varphi = \mathbb{K}$. Then we denote $\text{birth}(\alpha) = t_1$ and $\text{death}(\alpha) = t_2$, and the persistence of α is defined as

$$\text{pers}(\alpha) \stackrel{\text{def}}{=} \text{death}(\alpha) - \text{birth}(\alpha). \quad (\text{B.2})$$

With the notions of $\text{death}(\alpha)$ and $\text{birth}(\alpha)$, the k -th PD of \mathbb{K} with respect to φ is defined as the following multiset of 2-dimensional points (Mileyko et al., 2011, Definition 2).

$$\begin{aligned} & \text{Dgm}_k(\mathbb{K}; \varphi) \\ & \stackrel{\text{def}}{=} \left\{ (\text{birth}(\alpha), \text{death}(\alpha)) \mid \alpha \in H_k(\mathbb{K}_t) \text{ for some } t \in [0, T] \text{ with } \text{pers}(\alpha) > 0 \right\} \cup \mathfrak{D}, \end{aligned} \quad (\text{B.3})$$

where $(\text{birth}(\alpha_1), \text{death}(\alpha_1))$ and $(\text{birth}(\alpha_2), \text{death}(\alpha_2))$ for $\alpha_1 \neq \alpha_2$ are counted as two points even if α_1 and α_2 are born and die at the same times, respectively; that is, the multiplicity of the point $(\text{birth}(\alpha_1), \text{death}(\alpha_1)) = (\text{birth}(\alpha_2), \text{death}(\alpha_2))$ is at least 2; \mathfrak{D} denotes the diagonal $\{(t, t) \mid t \in \mathbb{R}\}$ with the multiplicity of each point on this diagonal is the cardinality of \mathbb{Z} . Since $\text{birth}(\alpha)$ is no later than $\text{death}(\alpha)$, the PD $\text{Dgm}_k(\mathbb{K}; \varphi)$ is contained in the triangular region $\{(s, t) \in \mathbb{R}^2 \mid 0 \leq s \leq t \leq T\}$.

B.2 Eq. (3.4) in the definition of $\mathcal{S}_{R,d}^M$

The following ingredients give the details of Condition 3.1.

- The function ϕ_ν defined in Eq. (B.1),
- the corresponding PDs defined by Eq. (B.3), and
- the definition of $\text{pers}(\cdot)$ given in Eq. (B.2).
- The notation $\#\{\cdot\}$ counts the multiplicity of the corresponding multiset.

B.3 Bottleneck Stability

Generally, a persistence diagram is a countable multiset of points in triangular region $\{(s, t) \in \mathbb{R}^2 \mid 0 \leq s, t \leq T \text{ and } s \leq t\}$ along with \mathfrak{D} (Mileyko et al., 2011, Definition 2).

The collection of all persistence diagrams is denoted as \mathcal{D} . Obviously, all the $\text{Dgm}_k(\mathbb{K}; \varphi)$ defined in Eq. (B.3) is in \mathcal{D} . The following definition and stability result of the *bottleneck distance* are from Cohen-Steiner et al. (2007), and they play important roles in the proofs of Theorems 3.2 and C.3.

Definition B.1. *Let \mathbb{K} be a compact topological space. φ_1 and φ_2 are two continuous real-valued functions on \mathbb{K} such that \mathbb{K} is tame with respect to both φ_1 and φ_2 . The bottleneck distance between PDs $\text{Dgm}_k(\mathbb{K}; \varphi_1)$ and $\text{Dgm}_k(\mathbb{K}; \varphi_2)$ is defined as*

$$W_\infty \left(\text{Dgm}_k(\mathbb{K}; \varphi_1), \text{Dgm}_k(\mathbb{K}; \varphi_2) \right) \stackrel{\text{def}}{=} \inf_\gamma \left(\sup \left\{ \|\xi - \gamma(\xi)\|_{l^\infty} \mid \xi \in \text{Dgm}_k(\mathbb{K}; \varphi_1) \right\} \right),$$

where γ ranges over bijections from $\text{Dgm}_k(\mathbb{K}; \varphi_1)$ to $\text{Dgm}_k(\mathbb{K}; \varphi_2)$, and

$$\|\xi\|_{l^\infty} \stackrel{\text{def}}{=} \max\{|\xi_1|, |\xi_2|\}, \quad \text{for all } \xi = (\xi_1, \xi_2)^\top \in \mathbb{R}^2. \quad (\text{B.4})$$

Theorem B.1. *Let \mathbb{K} be a compact and finitely triangulable topological space. φ_1 and φ_2 are two continuous real-valued functions on \mathbb{K} such that \mathbb{K} is tame with respect to both φ_1 and φ_2 . Then, we have the bottleneck stability as follows*

$$W_\infty\left(\text{Dgm}_k(\mathbb{K}; \varphi_1), \text{Dgm}_k(\mathbb{K}; \varphi_2)\right) \leq \sup_{x \in \mathbb{K}} |\varphi_1(x) - \varphi_2(x)|.$$

C Additional Theorems

In this section, we provide some further theorems and lemmas which may deepen our understanding of the SECT framework. The proofs of these theorems and lemmas are given in Appendix L.

- The following theorem shows that $C(\mathbb{S}^{d-1}; H_0^1([0, T]))$ is a separable Banach space, hence, a Polish space.

Theorem C.1. *(i) Let \mathcal{H} be a separable Hilbert space. Then, $C(\mathbb{S}^{d-1}; \mathcal{H})$ is separable.
(ii) Let \mathcal{H} be a separable Hilbert space. Then, $C(\mathbb{S}^{d-1}; \mathcal{H})$ is a Banach space.
(iii) $C(\mathbb{S}^{d-1}; H_0^1([0, T]))$ is a separable Banach space.*

Remark: The results in Theorem C.1 are well-known. The proof of Theorem C.1 is provided in Appendix L for the convenience of the reader.

- The following boundedness can be derived from Condition 3.1.

Theorem C.2. *If $K \in \mathcal{S}_{R,d}^M$, we have*

$$\sup_{\nu \in \mathbb{S}^{d-1}} \left\{ \sup_{0 \leq t \leq T} |\chi_t^\nu(K)| \right\} \leq M.$$

- Lemma 3.1 states that $t \mapsto \chi(K_t^\nu)$, for each $\nu \in \mathbb{S}^{d-1}$, is a piecewise constant function with only finitely many discontinuities. The following result that follows directly from Ji et al. (2023) clarifies the behaviors of $t \mapsto \chi(K_t^\nu)$ at the discontinuities.

Lemma C.1. *For any shape $K \in \mathcal{S}_d$ and fixed direction $\nu \in \mathbb{S}^{d-1}$, the function $t \mapsto \chi(K_t^\nu)$ is right continuous.*

- The following lemma indicates that the SECT is uniformly bounded.

Lemma C.2. *For any $K \in \mathcal{S}_{R,d}^M$, we have*

$$\|\text{SECT}(K)\|_{C(\mathbb{S}^{d-1}; \mathcal{H})} \leq 2M \cdot \sqrt{T}.$$

- Lemma 3.2 is a special case of the following lemma.

Lemma C.3. *For any fixed $K \in \mathcal{S}_{R,d}^M$ and $\nu \in \mathbb{S}^{d-1}$, the function $\text{SECT}(K)(\nu)$ (i.e., $t \mapsto \text{SECT}(K)(\nu, t)$ with fixed ν) belongs to $W_0^{1,p}([0, T]) \subseteq \mathcal{B}$ for all $p \in [1, \infty)$.*

Here, $W_0^{1,p}([0, T])$ is a Sobolev space defined as

$$W_0^{1,p}([0, T]) \stackrel{\text{def}}{=} \left\{ f \in L^p([0, T]) \mid \text{weak derivative } f' \in L^p([0, T]) \text{ and } f(0) = f(T) = 0 \right\}$$

(see Brezis, 2011, Theorem 8.12). We focus on the case $p = 2$ where $\mathcal{H} = H_0^1([0, T]) = W_0^{1,2}([0, T])$, which implies Lemma 3.2.

- The following theorem is a companion result of Theorem 3.2.

Theorem C.3. *For each $K \in \mathcal{S}_{R,d}^M$, we have the following:*

There exists a constant $C_{M,R,d}^$ depending only on M , R , and d such that the following inequality holds for any two directions $\nu_1, \nu_2 \in \mathbb{S}^{d-1}$,*

$$\left(\int_0^T \left| \chi_\tau^{\nu_1}(K) - \chi_\tau^{\nu_2}(K) \right|^2 d\tau \right)^{1/2} \leq C_{M,R,d}^* \cdot \sqrt{\|\nu_1 - \nu_2\|}. \quad (\text{C.1})$$

Furthermore, the constant \tilde{C}_T in Eq. (2.1) provides the following inequality

$$\begin{aligned} & \left| \text{SECT}(K)(\nu_1; t_1) - \text{SECT}(K)(\nu_2; t_2) \right| \\ & \leq \tilde{C}_T \left\{ 2M\sqrt{T} \cdot \sqrt{|t_1 - t_2|} + C_{M,R,d}^* \cdot \sqrt{\|\nu_1 - \nu_2\| + \|\nu_1 - \nu_2\|^2} \right\}, \end{aligned} \quad (\text{C.2})$$

for all $\nu_1, \nu_2 \in \mathbb{S}^{d-1}$ and $t_1, t_2 \in [0, T]$, which implies that $(\nu, t) \mapsto \text{SECT}(K)(\nu, t)$, as a function on $\mathbb{S}^{d-1} \times [0, T]$, belongs to $C^{0, \frac{1}{2}}(\mathbb{S}^{d-1} \times [0, T]; \mathbb{R})$.

- For any given o-minimal structure \mathcal{S} , elements of \mathcal{S} are called definable sets. Furthermore, compact definable sets are called constructible sets. The collection of constructible subsets of \mathbb{R}^d is denoted by $\text{CS}(\mathbb{R}^d)$ (e.g., see [Curry et al., 2022](#), Section 2). If the o-minimal structure \mathcal{S} satisfies Assumption 1, it is straightforward that our proposed $\mathcal{S}_{R,d}^M$ is a subset of $\text{CS}(\mathbb{R}^d)$.

Using the results originated from Euler calculus ([Schapira, 1988](#); [Viro, 1988](#); [Schapira, 1991, 1995](#); [van den Dries, 1998](#)), particularly the ‘‘Schapira’s inversion formula’’ ([Schapira, 1995](#)), [Ghrist et al. \(2018\)](#) and [Curry et al. \(2022\)](#) independently proved the following injectivity of the ECT.

Theorem C.4 (Theorem 1 of [Ghrist et al. \(2018\)](#) or Theorem 3.5 of [Curry et al. \(2022\)](#)). *The following map is injective for all dimensions d*

$$\begin{aligned} \text{ECT} : \text{CS}(\mathbb{R}^d) &\rightarrow \mathbb{Z}^{\mathbb{S}^{d-1} \times \mathbb{R}}, \\ K &\mapsto \{\chi(K_t^\nu)\}_{(\nu,t) \in \mathbb{S}^{d-1} \times \mathbb{R}}. \end{aligned}$$

The following result from [Ghrist et al. \(2018\)](#) is a corollary of Theorem C.4, and it guarantees the injectivity of the SECT.

Corollary C.1 (Corollary 1 of [Ghrist et al. \(2018\)](#)). *The smooth Euler characteristic transform of [Crawford et al. \(2020\)](#) is injective on constructible subsets of \mathbb{R}^d for all dimensions d .*

- We introduce another topological summary — the primitive Euler characteristic transform (PECT) — which is related to the SECT.

The PECT is defined as follows

$$\text{PECT} : \mathcal{S}_{R,d}^M \rightarrow C(\mathbb{S}^{d-1}; \mathcal{H}_{BM}), \quad K \mapsto \text{PECT}(K) \stackrel{\text{def}}{=} \{\text{PECT}(K)(\nu)\}_{\nu \in \mathbb{S}^{d-1}}, \quad (\text{C.3})$$

where $\text{PECT}(K)(\nu) \stackrel{\text{def}}{=} \left\{ \int_0^t \chi_\tau^\nu(K) d\tau \right\}_{t \in [0, T]}$,

and $\mathcal{H}_{BM} \stackrel{\text{def}}{=} \{f \in L^2([0, T]) \mid \text{weak derivative } f' \text{ exists, } f' \in L^2([0, T]), \text{ and } f(0) = 0\}$ is a separable Hilbert space equipped with the inner product

$$\langle f, g \rangle_{\mathcal{H}_{BM}} = \int_0^T f'(t)g'(t)dt.$$

Eq. (C.1), together with Lemma L.1, implies that

$$\|\text{PECT}(K)(\nu_1) - \text{PECT}(K)(\nu_2)\|_{\mathcal{H}_{BM}} \leq C_{M,R,d}^* \cdot \sqrt{\|\nu_1 - \nu_2\|},$$

for any $\nu_1, \nu_2 \in \mathbb{S}^{d-1}$. Therefore, we have $\text{PECT}(K) \in C(\mathbb{S}^{d-1}; \mathcal{H}_{BM})$ in Eq. (C.3).

Section L.10 shows that the following map is continuous, hence, measurable

$$\text{PECT} : \mathcal{S}_{R,d}^M \rightarrow \mathbb{R},$$

$$K \mapsto \text{PECT}(K)(\nu, t).$$

Then, for each fixed direction $\nu \in \mathbb{S}^{d-1}$, $\text{PECT}(\nu) \stackrel{\text{def}}{=} \{\text{PECT}(\nu, t)\}_{t \in [0, T]}$ is a stochastic process.

The following theorem regarding the PECT indicates that the stochastic process $\text{SECT}(\nu) = \{\text{SECT}(\nu, t)\}_{t \in [0, T]}$ tends to be non-Gaussian for every fixed direction ν .

Theorem C.5. *Let $\nu \in \mathbb{S}^{d-1}$ be a fixed direction. If the stochastic processes $\{\chi_t^\nu \mid t_0 < t \leq t_1\}$, $\{\chi_t^\nu \mid t_1 < t \leq t_2\}$, \dots , $\{\chi_t^\nu \mid t_{l-1} < t \leq t_l\}$ are independent for any partition $0 = t_0 < t_1 < \dots < t_l = T$ of $[0, T]$, the stochastic process $\text{PECT}(\nu) = \{\text{PECT}(\nu, t)\}_{t \in [0, T]}$ is a Gaussian process.*

Remark C.1. *The independence condition in Theorem C.5 cannot hold, because the sample paths of the stochastic process $\{\chi_t^\nu\}_{t \in [0, T]}$ are piecewise constant functions (see*

Lemmas 3.1 and C.1). Hence, there is no guarantee for the Gaussianity of the PECT.

Note that the PECT relates to the SECT via the following

$$\text{SECT}(K)(\nu, t) = \text{PECT}(K)(\nu, t) - \frac{t}{T} \text{PECT}(K)(\nu, T), \quad (\text{C.4})$$

for all $\nu \in \mathbb{S}^{d-1}$ and $t \in [0, T]$. The Gaussianity of the SECT is not guaranteed.

- The following lemma provides several properties of the mean m_ν and covariance Ξ_ν that validate our KL expansion of SECT(ν) in Section 5 (also see Hsing and Eubank, 2015, Section 7.2).

Lemma C.4. *i) For each ν , the function $m_\nu \stackrel{\text{def}}{=} \{m_\nu(t)\}_{t \in [0, T]}$ of t is in \mathcal{H} .*

ii) The map $(K, t) \mapsto \text{SECT}(K)(\nu, t)$ is in

$$L^2\left(\mathcal{S}_{R,d}^M \times [0, T], \mathcal{F} \otimes \mathcal{B}([0, T]), \mathbb{P}(dK) \otimes dt\right),$$

where $\mathbb{P}(dK) \otimes dt$ denotes the product measure generated by $\mathbb{P}(dK)$ and the Lebesgue measure dt .

iii) SECT(ν) is mean-square continuous, i.e.,

$$\lim_{\epsilon \rightarrow 0} \mathbb{E} |\text{SECT}(\nu, t + \epsilon) - \text{SECT}(\nu, t)|^2 = 0.$$

iv) $(s, t) \mapsto \Xi_\nu(s, t)$ is continuous on $[0, T]^2$.

v) The map $\nu \mapsto m_\nu$ is an element of $C(\mathbb{S}^{d-1}; \mathcal{H})$.

Remark: Although the mean $\mathbf{m} \stackrel{\text{def}}{=} \{m_\nu\}_{\nu \in \mathbb{S}^{d-1}}$ of SECT belongs to $C(\mathbb{S}^{d-1}; \mathcal{H})$ (see Lemma C.4), it may not belong to $\text{SECT}(\mathcal{S}_{R,d}^M)$ (note that the SECT is not surjective). Hence, there does not necessarily exist a shape in $\mathcal{S}_{R,d}^M$ whose SECT is \mathbf{m} . Under some topological conditions, the ‘‘Schapira’s inversion formula’’ (Schapira, 1995) can

be applied to obtain a pseudo-inverse $\text{SECT}^{-1}(\mathbf{m})$. However, the $\text{SECT}^{-1}(\mathbf{m})$ can be a “grayscale image” (e.g., shape with blurred boundary) instead of a shape in $\mathcal{S}_{R,d}^M$. Specifically, Meng et al. (2023) generalized the SECT from shapes to grayscale images, enlarging the image of the SECT. The mean \mathbf{m} may correspond to a grayscale image under some conditions. Detailed discussions on the relationship between the SECT and grayscale images are provided in Meng et al. (2023). In addition, a relevant discussion from the Fréchet mean viewpoint is given in Appendix D.2. Complete studies on the pseudo-inverse $\text{SECT}^{-1}(\mathbf{m})$ are left for future research.

D Proof-of-Concept Simulation Examples

In Section D.1, we provide proof-of-concept examples to visually illustrate the SECT of deterministic shapes and support the $\frac{1}{2}$ -Hölder regularity stated in Theorems 3.2 and C.3. Then, in Section D.2, we provide proof-of-concept examples to illustrate random shapes and their SECT representations visually; the examples in Section D.2 provide potential relationships between the Fréchet mean (Fréchet, 1948), Fréchet regression (Petersen and Müller, 2019), Wasserstein regression (Chen et al., 2023), and manifold learning (Dunson and Wu, 2021; Meng and Eloyan, 2021; Li et al., 2022). Lastly, in Section D.3, we provide an approach to approximately computing the SECT, which is implemented in Sections 6, D.1, and D.2 to compute the SECT values.

D.1 Proof-of-Concept Simulation Examples I: Deterministic Shapes

In this subsection, we compute the SECT of two simulated shapes $K^{(1)}$ and $K^{(2)}$ of dimension $d = 2$. These shapes are defined as the following and presented in Supplementary

Figures D.1(a) and (g), respectively:

$$\begin{aligned}
K^{(j)} &= \left\{ x \in \mathbb{R}^2 \mid \inf_{y \in S^{(j)}} \|x - y\| \leq \frac{1}{5} \right\}, \quad \text{where } j \in \{1, 2\}, \\
S^{(1)} &= \left\{ \left(\frac{2}{5} + \cos t, \sin t \right) \mid \frac{\pi}{5} \leq t \leq \frac{9\pi}{5} \right\} \cup \left\{ \left(-\frac{2}{5} + \cos t, \sin t \right) \mid \frac{6\pi}{5} \leq t \leq \frac{14\pi}{5} \right\}, \\
S^{(2)} &= \left\{ \left(\frac{2}{5} + \cos t, \sin t \right) \mid 0 \leq t \leq 2\pi \right\} \cup \left\{ \left(-\frac{2}{5} + \cos t, \sin t \right) \mid \frac{6\pi}{5} \leq t \leq \frac{14\pi}{5} \right\}.
\end{aligned} \tag{D.1}$$

We compute $\text{SECT}(K^{(j)})(\nu, t)$ across directions $\nu \in \mathbb{S}^1$ and sublevel sets $t \in [0, T]$ with $T = 3$. For the following visualization, we identify $\nu \in \mathbb{S}^1$ through the parametrization $\nu = (\cos \vartheta, \sin \vartheta)$ with $\vartheta \in [0, 2\pi)$.

- The surfaces of the bivariate maps $(\vartheta, t) \mapsto \text{SECT}(K^{(j)})(\nu, t)$, for $j \in \{1, 2\}$, are presented in Supplementary Figures D.1(b), (c), (h), and (i).
- The curves of the univariate maps $t \mapsto \text{SECT}(K^{(j)})((1, 0)^\top; t)$, for $j \in \{1, 2\}$, are presented by the black solid lines in Supplementary Figures D.1(d) and (j); while the curves of the univariate maps $t \mapsto \text{SECT}(K^{(j)})((0, 1)^\top; t)$, for $j \in \{1, 2\}$, are presented by black solid lines in Supplementary Figures D.1(e) and (k).
- Lastly, the curves of the univariate maps $\vartheta \mapsto \text{SECT}(K^{(j)})((\cos \vartheta, \sin \vartheta)^\top; \frac{3}{2})$, for $j \in \{1, 2\}$, are presented by the black solid lines in Supplementary Figures D.1(f) and (l).

These figures illustrate the continuity of $(\nu, t) \mapsto \text{SECT}(K^{(j)})(\nu, t)$ stated in Theorem C.3 (Eq. (C.2) therein). Specifically, the curves and surfaces in these figures look smoother than the sample path of Brownian motions, while they are not differentiable everywhere. With probability one, the sample paths of a Brownian motion are not locally $C^{0, \frac{1}{2}}$ -continuous (Klenke, 2013, Remark 22.4). Hence, based on Supplementary Figure D.1,

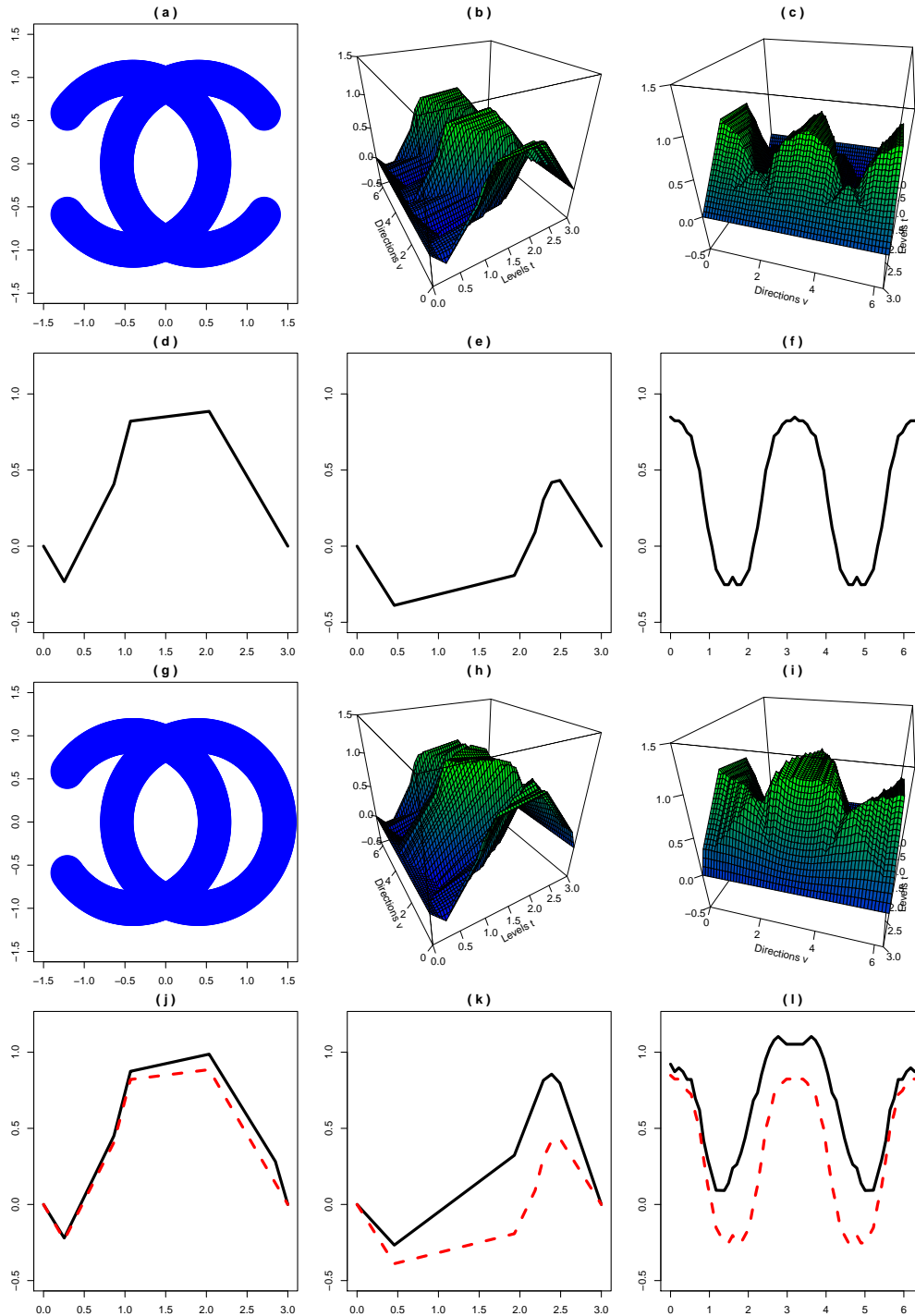


Figure D.1: Visualizations of $\text{SECT}(K^{(j)})$ for $j \in \{1, 2\}$, where $K^{(1)}$ and $K^{(2)}$ are defined in Eq. (D.1).

Panels (b) and (c) present the same surface from different angles. Panels (h) and (i) present the same surface from different angles. The similarity between the curves in panel (j) partially indicates that the SECT in only one direction does not preserve all the geometric information of a shape. Panels (g) and (h) also appear in the main text under Figure 3.1.

the regularity of $(\nu, t) \mapsto \text{SECT}(K^{(j)})(\nu, t)$ is likely to be better than that of Brownian motion sample paths, but worse than continuously differentiable functions. Therefore, Supplementary Figure D.1 supports the $C^{0, \frac{1}{2}}$ -continuity in Theorem C.3.

Theorem 3.3 (i.e., the SECT as a map is injective) indicates that all information of $K^{(1)}$ and $K^{(2)}$ is stored in the surfaces presented by Supplementary Figures D.1(b), (c), (h), and (i). The red dashed curves in Supplementary Figures D.1(j), (k), and (l) are the counterparts of $K^{(1)}$ (see the curves in Supplementary Figures D.1(d), (e), and (f)). The discrepancy between the solid black and dashed red curves illustrates the ability of the SECT to distinguish shapes, which motivates us to develop the hypothesis testing approach in Section 5.

D.2 Proof-of-Concept Simulation Examples II: Random Shapes

In this subsection, we compute the SECT for a collection of random shapes $\{K_i\}_{i=1}^n$ of dimension $d = 2$. These shapes are randomly generated as follows

$$\begin{aligned}
 K_i &= \left\{ x \in \mathbb{R}^2 \left| \inf_{y \in S_i} \|x - y\| \leq \frac{1}{5} \right. \right\}, \quad \text{where} \\
 S_i &= \left\{ \left(\frac{2}{5} + a_{1,i} \times \cos t, \quad b_{1,i} \times \sin t \right) \left| \frac{\pi}{5} \leq t \leq \frac{9\pi}{5} \right. \right\} \\
 &\quad \cup \left\{ \left(-\frac{2}{5} + a_{2,i} \times \cos t, \quad b_{2,i} \times \sin t \right) \left| \frac{6\pi}{5} \leq t \leq \frac{14\pi}{5} \right. \right\},
 \end{aligned} \tag{D.2}$$

and $\{a_{1,i}, a_{2,i}, b_{1,i}, b_{2,i}\}_{i=1}^n \stackrel{\text{i.i.d.}}{\sim} N(1, 0.05^2)$ follow a normal distribution. One element of the shape collection $\{K_i\}_{i=1}^n$ is presented in Supplementary Figure D.2(a). The underlying distribution on $\mathcal{S}_{R,d}^M$ generating $\{K_i\}_{i=1}^n$ is denoted by \mathbb{P} , and the expectation associated with \mathbb{P} is denoted by \mathbb{E} . We estimate the expected value $\mathbb{E}\{\text{SECT}(\nu, t)\}$ by the sample average $\frac{1}{n} \sum_{i=1}^n \text{SECT}(K_i)(\nu, t)$ with $n = 100$. We identify each direction $\nu \in \mathbb{S}^1$ through the parametrization $\nu = (\cos \vartheta, \sin \vartheta)$ with some $\vartheta \in [0, 2\pi)$ as we did in Section D.1.

- The surface of the map $(\vartheta, t) \mapsto \mathbb{E}\{\text{SECT}(\nu, t)\}$ is presented in Supplementary Figures [D.2\(b\)](#) and [\(c\)](#).
- The black solid curves in Supplementary Figure [D.2\(d\)](#) present the 100 sample paths $t \mapsto \text{SECT}(K_i)((1, 0)^\top, t)$; the black solid curves in Supplementary Figure [D.2\(e\)](#) present sample paths $t \mapsto \text{SECT}(K_i)((0, 1)^\top, t)$; and the black solid curves in Supplementary Figure [D.2\(f\)](#) present paths $\vartheta \mapsto \text{SECT}(K_i)((\cos \vartheta, \sin \vartheta)^\top, \frac{3}{2})$, for $i \in \{1, \dots, 100\}$.
- The red solid curves in Supplementary Figures [D.2\(d\)](#), [\(e\)](#), and [\(f\)](#) present mean curves

$$\begin{aligned}
 & t \mapsto \mathbb{E}\{\text{SECT}((1, 0)^\top, t)\}, \\
 & t \mapsto \mathbb{E}\{\text{SECT}((0, 1)^\top, t)\}, \text{ and} \\
 & \vartheta \mapsto \mathbb{E}\left\{\text{SECT}\left((\cos \vartheta, \sin \vartheta)^\top, \frac{3}{2}\right)\right\},
 \end{aligned}$$

respectively.

The smoothness of the red solid curves in Supplementary Figures [D.2\(d\)](#) and [\(e\)](#) supports the regularity of $\{m_\nu(t)\}_{t \in [0, T]}$ in Lemma [C.4](#). The finite variance of $\text{SECT}(\nu, t)$ for $\nu = (1, 0)^\top, (0, 1)^\top$ and $t = 3/2$, visually presented in Supplementary Figures [D.2\(d\)](#), [\(e\)](#), and [\(f\)](#), supports Lemma [4.1](#).

In addition, the blue dashed curves in Supplementary Figures [D.2\(d\)](#), [\(e\)](#), and [\(f\)](#) present curves

$$\begin{aligned}
 & t \mapsto \text{SECT}(K^{(1)}((1, 0)^\top, t), \\
 & t \mapsto \text{SECT}(K^{(1)}((0, 1)^\top, t), \text{ and} \\
 & \vartheta \mapsto \text{SECT}(K^{(1)}((\cos \vartheta, \sin \vartheta)^\top, \frac{3}{2})),
 \end{aligned}$$

respectively, where shape $K^{(1)}$ is defined in Eq. (D.1). Since $\mathbb{E}\{a_{1,i}\} = \mathbb{E}\{a_{2,i}\} = \mathbb{E}\{b_{1,i}\} = \mathbb{E}\{b_{2,i}\} = 1$, the shape $K^{(1)}$ defined in Eq. (D.1) can be somewhat viewed as the “mean shape” of the random collection $\{K_i\}_{i=1}^n$. The similarity between the red solid curves and blue dashed curves in D.2(d), (e), and (f) supports the “mean shape” role of $K^{(1)}$. The rigorous definition of a “mean shape” and its relationship to the mean function $\mathbb{E}\{\text{SECT}(\nu, t)\}$ is outside the scope of this work. A potential approach for defining mean shapes is through the following Fréchet mean (Fréchet, 1948)

$$K_{\oplus} \stackrel{\text{def}}{=} \underset{K \in \mathcal{S}_{R,d}^M}{\text{argmin}} \mathbb{E} [\{\rho(\cdot, K)\}^2] = \underset{K \in \mathcal{S}_{R,d}^M}{\text{argmin}} \left[\int_{\mathcal{S}_{R,d}^M} \{\rho(K', K)\}^2 \mathbb{P}(dK') \right], \quad (\text{D.3})$$

where ρ can be either the metric on $\mathcal{S}_{R,d}^M$ defined in Eq. (4.1) or any other metrics generating σ -algebras satisfying Assumption 2.

The existence and uniqueness of the minimizer K_{\oplus} in Eq. (D.3), the relationship between $\text{SECT}(K_{\oplus})$ and $\mathbb{E}\{\text{SECT}\}$, and the extension of Eq. (D.3) to Fréchet and Wasserstein regression (Petersen and Müller, 2019; Chen et al., 2023) for random shapes are left for future research. The study of the existence of K_{\oplus} will be an analog of Section 4 in Mileyko et al. (2011).

In the scenarios where the SECT of shapes from distribution \mathbb{P} are computed only in finitely many directions and at finitely many levels (see the end of Section 4), the mean surface $(\vartheta, t) \mapsto \mathbb{E}\{\text{SECT}(\nu, t)\}$ in Supplementary Figures D.2(b) and (c) can also be potentially estimated using manifold learning methods (Dunson and Wu, 2021; Meng and Eloyan, 2021; Li et al., 2022).

D.3 Computation of SECT

Here, we present an approach to computing the SECT of the shapes in Figures D.1 and D.2. Let $K \subseteq \mathbb{R}^d$ be a shape of interest. Suppose a finite set of points $\{x_i\}_{i=1}^I \subseteq K$ and a

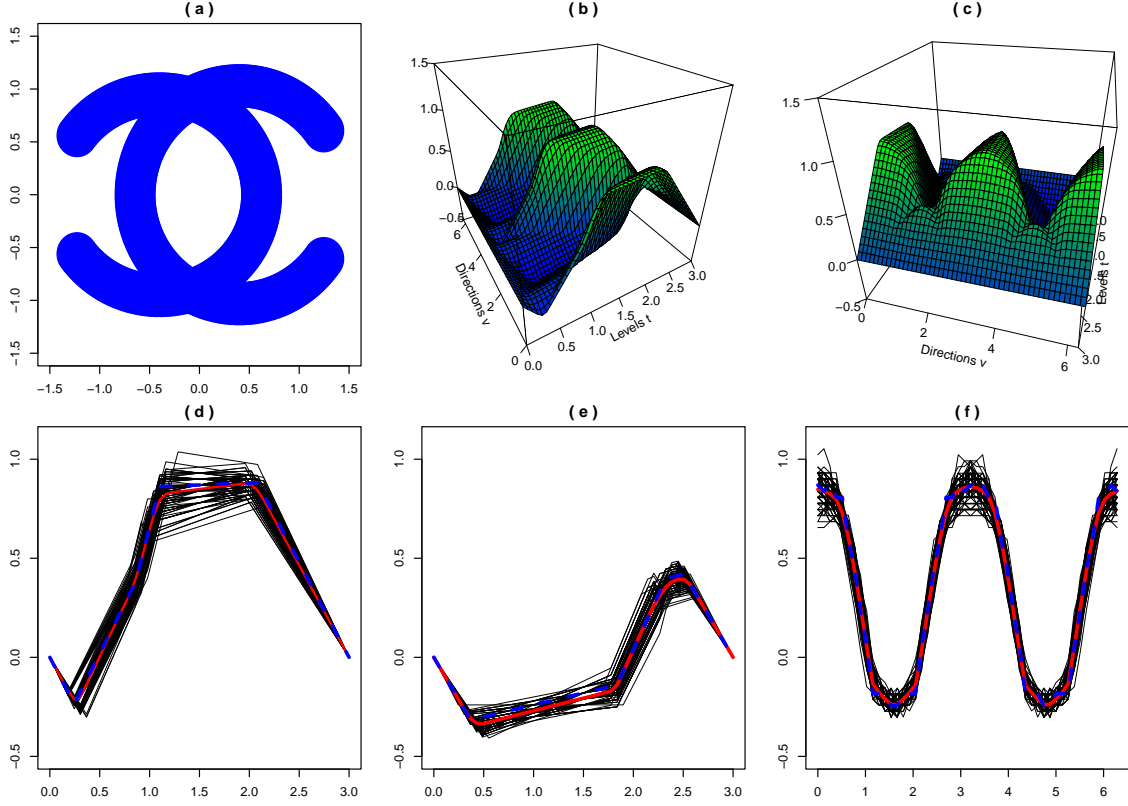


Figure D.2: Panel (a) presents a shape generated from the distribution in Eq. (D.2). Panels (b) and (c) present the mean surface $(\vartheta, t) \mapsto \mathbb{E}\{\text{SECT}(\nu, t)\}$ from different angles. Panels (d), (e), and (f) present the sample paths $\{\text{SECT}(K_i)(\nu, t)\}_{i=1}^n$ with $\nu = (1, 0)^\top$, $\nu = (0, 1)^\top$, and $t = 3/2$, respectively.

radius $r > 0$ are properly chosen such that

$$K_t^\nu = \{x \in K \mid x \cdot \nu \leq t - R\} \approx \bigcup_{i \in \mathfrak{J}_t^\nu} \overline{B(x_i, r)}, \quad \text{for all } t \in [0, T] \text{ and } \nu \in \mathbb{S}^{d-1}, \quad (\text{D.4})$$

$$\text{where } \mathfrak{J}_t^\nu \stackrel{\text{def}}{=} \left\{ i \in \mathbb{N} \mid 1 \leq i \leq I \text{ and } x_i \cdot \nu \leq t - R \right\},$$

and $\overline{B(x_i, r)} \stackrel{\text{def}}{=} \{x \in \mathbb{R}^d : \|x - x_i\| \leq r\}$ denotes a closed ball centered at x_i with radius r .

For example, when $d = 2$, centers x_i may be chosen as a subset of the grid points

$$\left\{ y_{j,j'} \stackrel{\text{def}}{=} (-R + j \cdot \delta, -R + j' \cdot \delta)^\top \right\}_{j,j'=1}^J$$

of the square $[-R, R]^2$ containing shape K , where $\delta = \frac{2R}{J}$ and radius $r = \delta$. Specifically,

$$K_t^\nu \approx \bigcup_{y_{j,j'} \in K_t^\nu} \overline{B(y_{j,j'}, \delta)} \quad \text{for all } t \in [0, T] \text{ and } \nu \in \mathbb{S}^{d-1}, \quad (\text{D.5})$$

which is a special case of Eq. (D.4). The shape approximation in Eq. (D.5) is illustrated by Supplementary Figures D.3(a) and (b).

Čech complexes The Čech Complex determined by the point set $\{x_i\}_{i \in \mathcal{I}_t^\nu}$ and radius r in Eq. (D.4) is defined as the following simplicial complex

$$\check{C}_r(\{x_i\}_{i \in \mathcal{I}_t^\nu}) \stackrel{\text{def}}{=} \left\{ \text{conv}(\{x_i\}_{i \in s}) \mid s \in 2^{\mathcal{I}_t^\nu} \text{ and } \bigcap_{i \in s} \overline{B(x_i, r)} \neq \emptyset \right\},$$

where $\text{conv}(\{x_i\}_{i \in s})$ denotes the convex hull generated by points $\{x_i\}_{i \in s}$. The nerve theorem (Edelsbrunner and Harer, 2010, Chapter III) indicates that the Čech Complex $\check{C}_r(\{x_i\}_{i \in \mathcal{I}_t^\nu})$ and the union $\bigcup_{i \in \mathcal{I}_t^\nu} \overline{B(x_i, r)}$ have the same homotopy type. Hence, they share the same Betti numbers, i.e.,

$$\beta_k(\check{C}_r(\{x_i\}_{i \in \mathcal{I}_t^\nu})) = \beta_k\left(\bigcup_{i \in \mathcal{I}_t^\nu} \overline{B(x_i, r)}\right), \quad \text{for all } k \in \mathbb{Z}.$$

Using the shape approximation in Eq. (D.4), we have the following approximation for ECC

$$\chi_t^\nu(K) \approx \sum_{k=0}^{d-1} (-1)^k \cdot \beta_k(\check{C}_r(\{x_i\}_{i \in \mathcal{I}_t^\nu})), \quad t \in [0, T]. \quad (\text{D.6})$$

The method of computing the Betti numbers of simplicial complexes in Eq. (D.6) is standard and can be found in the literature (Edelsbrunner and Harer, 2010; Niyogi et al., 2008). Then, the SECT of K is estimated using Eq. (3.3). The smoothing effect of the integrals in Eq. (3.3) reduces the estimation error.

Computing the SECT for our proof-of-concept and simulation examples For the shape $K^{(1)}$ defined in Eq. (D.1) of Section D.1, we estimate the SECT of $K^{(1)}$ using the aforementioned Čech complex approach with the following setup: $R = \frac{3}{2}$, $r = \frac{1}{5}$, and

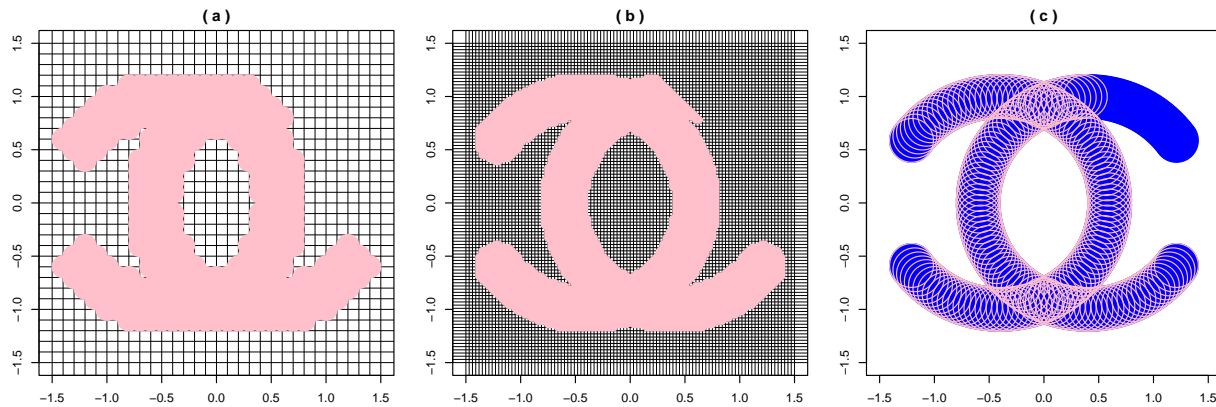


Figure D.3: Illustrations of the shape approximation in Eq. (D.4). The shape K of interest herein is equal to the $K^{(1)}$ defined in Eq. (D.1) (see Supplementary Figure D.1(a) and the blue shape in the panel (c) herein). We set $R = \frac{3}{2}$, $t = 1$, and $\nu = (\sqrt{2}/2, \sqrt{2}/2)^\top$. Panels (a) and (b) specifically illustrate the approximation in Eq. (D.5) using grid points, and the pink shapes in the two panels present the union $\bigcup_{y_j, y_{j'} \in K_t^\nu} \overline{B(y_j, y_{j'}, \delta)}$ in Eq. (D.5); in panel (a), $J = 30$ (i.e., $\delta = 0.1$); in panel (b), $J = 100$ (i.e., $\delta = 0.03$). Panel (c) illustrates the approximation in Eq. (D.4) with centers $\{x_i\}_i$ being the points in Eq. (D.7) and $r = \frac{1}{5}$. Each pink circle in panel (c) presents a ball $\overline{B(x_i, r)}$.

the point set $\{x_i\}_i$ is equal to the following collection

$$\left\{ \left(\frac{2}{5} + \cos t_j, \sin t_j \right) \mid t_j = \frac{\pi}{5} + \frac{j}{J} \cdot \frac{8\pi}{5} \right\}_{j=1}^J \cup \left\{ \left(-\frac{2}{5} + \cos t_j, \sin t_j \right) \mid \frac{6\pi}{5} + \frac{j}{J} \cdot \frac{8\pi}{5} \right\}_{j=1}^J, \quad (\text{D.7})$$

where J is a sufficiently large integer. We implement $J = 100$ in our proof-of-concept example. Supplementary Figure D.3(c) illustrates the shape approximation using this setup. The SECT for other shapes in our proof-of-concept/simulation examples is estimated in the similar way.

E Alignment

In this subsection, we introduce an important preprocessing step based on the ECT to align shapes and discuss its motivation.

E.1 Motivation

It is widely accepted in geometric morphometrics that the intrinsic information of a shape does not change if one translates, rotates, or reflects (if handedness is ignored) the shape, which is mathematically represented as follows. Let $E(d)$ be the group of rigid motions in \mathbb{R}^d (i.e., the Euclidean group, it comprises translations, rotations, reflections, and finite combinations of them). Shapes K and K' are identified as the same if there exists $\varphi \in E(d)$ such that $K = \varphi(K')$ (denoted as $K \sim K'$). One can verify that \sim is an equivalence relation and the shape collection of interest is the quotient space $\mathcal{S}_{R,d}^M / \sim$. Since the ρ in Eq. (4.1) is a metric, we may detect the equivalence between K and K' via the following

$$\tilde{\rho}(K, K') \stackrel{\text{def}}{=} \inf_{\varphi \in E(d)} \{\rho(K, \varphi(K'))\}. \quad (\text{E.1})$$

That is, $K \sim K'$ if $\tilde{\rho}(K, K') = 0$. Eq. (E.1) resembles the Procrustes distance in statistical shape analysis (Gao et al., 2019a, Section 2.1).

To compute the $\tilde{\rho}$ in Eq. (E.1), one needs $\text{ECT}(\varphi(K)) = \{\chi_t^\nu(\varphi(K)) \mid (\nu, t) \in \mathbb{S}^{d-1} \times [0, T]\}$ for all $\varphi \in E(d)$. Computing the ECT of every shape $\varphi(K)$ for all $\varphi \in E(d)$ can be computationally expensive. We may implement the following to bypass the infeasible computation: We compute the ECT of only one shape K ; we apply the “dual motion” φ_* to the computed $\text{ECT}(K)$ such that $\varphi_* \text{ECT}(K) = \text{ECT}(\varphi(K))$. Then, it suffices to derive the dual motion φ_* and show that φ_* is computationally efficient for every $\varphi \in E(d)$. By the structure of $E(d)$, we only need to derive the dual motions of translations and $O(d)$ -actions, where $O(d)$ is the orthogonal group in dimension d (rotations and reflections).

We first consider translations. For any $\eta \in \mathbb{R}^d$, denote $K + \eta \stackrel{\text{def}}{=} \{x + \eta \mid x \in K\}$ and assume $K + \eta \subseteq B(0, R)$ without loss of generality. One can then show the following

$$\chi_t^\nu(K + \eta) = \chi_{t-\eta}^\nu(K). \quad (\text{E.2})$$

That is, if $\varphi : x \mapsto x + \eta$, then its dual $\varphi_* : \chi_t^\nu \mapsto \chi_{t-\eta}^\nu$. Secondly, we consider $O(d)$ -actions. For any $\mathbf{A} \in O(d)$, denote $\mathbf{A}K \stackrel{\text{def}}{=} \{\mathbf{A}x \mid x \in K\}$. One can show the following

$$\chi_t^\nu(\mathbf{A}K) = \chi_t^{\mathbf{A}^{-1}\nu}(K) \quad (\text{E.3})$$

(for a generalized version, see [Meng et al., 2023](#)). That is, if $\varphi : x \mapsto \mathbf{A}x$, then $\varphi_* : \chi_t^\nu \mapsto \chi_t^{\mathbf{A}^{-1}\nu}$. Furthermore, Eq. (E.2) and Eq. (E.3) imply that rigid motions do not influence the qualitative properties of SECT (e.g., measurability, Sobolev-regularity, and $\frac{1}{2}$ -Hölder continuity).

E.2 ECT Alignment

In almost all shape analysis studies, the initial step is to align the shapes. The objective of the alignment is to mitigate the difference between two shapes caused by rigid motions. Suppose K^\diamond is the “standard shape” as a template. Motivated by Eq. (E.1), we align each shape K to be $\varphi^\diamond(K)$ before any statistical inference, where

$$\varphi^\diamond \stackrel{\text{def}}{=} \operatorname{argmin}_{\varphi \in \mathbb{E}(d)} \{\rho(K^\diamond, \varphi(K))\}. \quad (\text{E.4})$$

Following the discussion at the end of Section E.1, the ECT alignment defined in Eq. (E.4) does not change the qualitative properties of the SECT. A numerical approach for the minimization in Eq. (E.4), as well as its proof-of-concept studies, is provided in Supplementary Material of [Wang et al. \(2021\)](#) (Section 4). We apply this numerical approach in our paper.

F Numerical Foundation for Hypothesis Testing

In Section 5, we proposed a fdANOVA approach to testing the hypotheses in Eq. (5.2) based on the $\{\xi_{l,i}\}_l$ defined in Eq. (5.6). In applications, neither the mean $m_{\nu}^{(j)}(t)$ nor the covariance $\Xi_{\nu}(s, t)$ is known. Hence, the corresponding KL expansion in Eq. (5.4) is unavailable, and the proposed hypothesis testing approach is not directly applicable. Here, motivated by Section 4.3.2 of Rasmussen and Williams (2006), we propose a method for estimating the $\{\xi_{l,i}\}_l$ defined in Eq. (5.6).

For random shapes $\{K_i^{(j)}\}_{i=1}^n \stackrel{\text{i.i.d.}}{\sim} \mathbb{P}^{(j)}$, with $j \in \{1, 2\}$, we compute their corresponding SECT in finitely many directions and sublevel sets as discussed at the end of Section 4 to get $\{\text{SECT}(K_i^{(j)})(\nu_p; t_q) \mid p = 1, \dots, \Gamma \text{ and } q = 1, \dots, \Delta\}_{i=1}^n$ for $j \in \{1, 2\}$, where $t_q = \frac{T}{\Delta}q$. The SECT of all shapes $K_i^{(j)}$ in the two collections are computed in the same collection of directions $\{\nu_p\}_{p=1}^{\Gamma}$ and at the same collection of sublevel sets $\{t_q\}_{q=1}^{\Delta}$. Using Eq. (5.3) of Zhang (2013), we estimate the mean $\widehat{m}_{\nu_p}^{(j)}(t_q)$ of $m_{\nu_p}^{(j)}(t_q)$ at level t_q by taking the sample mean of $\{\text{SECT}(K_i^{(j)})(\nu_p; t_q)\}_{i=1}^n$ across $i \in \{1, \dots, n\}$. Then, we estimate the distinguishing direction ν^* by

$$\widehat{\nu}^* \stackrel{\text{def}}{=} \underset{\nu_p}{\operatorname{argmax}} \left[\max_{t_q} \left\{ \left| \widehat{m}_{\nu_p}^{(1)}(t_q) - \widehat{m}_{\nu_p}^{(2)}(t_q) \right| \right\} \right]. \quad (\text{F.1})$$

Under Assumption 3, we estimate the covariance matrix $(\Xi_{\nu^*}(t_{q'}, t_q))_{q, q'=1, \dots, \Delta}$ using the pooled sample covariance matrix $\mathbf{C} = \left(\widehat{\Xi}_{\nu^*}(t_{q'}, t_q) \right)_{q, q'=1, \dots, \Delta}$ defined by

$$\widehat{\Xi}_{\nu^*}(t_{q'}, t_q) \stackrel{\text{def}}{=} \frac{1}{2n-1} \sum_{j=1}^2 \sum_{i=1}^n \left(\text{SECT}(K_i^{(j)})(\widehat{\nu}^*, t_{q'}) - \widehat{m}_{\widehat{\nu}^*}^{(j)}(t_{q'}) \right) \cdot \left(\text{SECT}(K_i^{(j)})(\widehat{\nu}^*, t_q) - \widehat{m}_{\widehat{\nu}^*}^{(j)}(t_q) \right), \quad (\text{F.2})$$

which is based on Eq. (5.3) of Zhang (2013).

Since the eigenfunctions $\{\phi_l\}_{l=1}^{\infty}$ and eigenvalues $\{\lambda_l\}_{l=1}^{\infty}$ satisfy $\lambda_l \phi_l = \int_0^T \phi_l(s) \cdot \Xi_{\nu^*}(s, \cdot) ds$,

we have the following approximation

$$\lambda_l \phi_l(t_q) = \int_0^T \phi_l(s) \cdot \Xi_{\nu^*}(s, t_q) ds \approx \frac{T}{\Delta} \sum_{q'=1}^{\Delta} \phi_l(t_{q'}) \cdot \Xi_{\nu^*}(t_{q'}, t_q) \approx \frac{T}{\Delta} \sum_{q'=1}^{\Delta} \phi_l(t_{q'}) \cdot \widehat{\Xi}_{\nu^*}(t_{q'}, t_q),$$

which is represented in the following matrix form

$$\lambda_l \begin{pmatrix} \phi_l(t_1) \\ \vdots \\ \phi_l(t_\Delta) \end{pmatrix} \approx \frac{T}{\Delta} \begin{pmatrix} \widehat{\Xi}_{\nu^*}(t_1, t_1) & \dots & \widehat{\Xi}_{\nu^*}(t_\Delta, t_1) \\ \vdots & \ddots & \vdots \\ \widehat{\Xi}_{\nu^*}(t_\Delta, t_2) & \dots & \widehat{\Xi}_{\nu^*}(t_\Delta, t_\Delta) \end{pmatrix} \begin{pmatrix} \phi_l(t_1) \\ \vdots \\ \phi_l(t_\Delta) \end{pmatrix}. \quad (\text{F.3})$$

We denote the eigenvectors and eigenvalues of \mathbf{C} as $\{\mathbf{v}_l = (v_{l,1}, \dots, v_{l,\Delta})^\top\}_{l=1}^{\Delta}$ and $\{\Lambda_l\}_{l=1}^{\Delta}$, respectively. The following equation motivates the estimator $\phi_l(t_q) \approx \widehat{\phi}_l(t_q) \stackrel{\text{def}}{=} \sqrt{\frac{\Delta}{T}} \cdot v_{l,q}$, for all $l \in \{1, \dots, \Delta\}$,

$$\sum_{q=1}^{\Delta} v_{l,q}^2 = \|\mathbf{v}_l\|^2 = 1 = \int_0^T |\phi_l(t)|^2 dt \approx \frac{T}{\Delta} \sum_{q=1}^{\Delta} (\phi_l(t_q))^2 = \sum_{q=1}^{\Delta} \left(\sqrt{\frac{T}{\Delta}} \cdot \phi_l(t_q) \right)^2.$$

The following equation motivates the estimator $\lambda_l \approx \widehat{\lambda}_l \stackrel{\text{def}}{=} \frac{T}{\Delta} \Lambda_l$, for all $l \in \{1, \dots, \Delta\}$,

$$\begin{aligned} \lambda_l \left(\widehat{\phi}_l(t_1), \dots, \widehat{\phi}_l(t_\Delta) \right)^\top &\approx \frac{T}{\Delta} \mathbf{C} \left(\widehat{\phi}_l(t_1), \dots, \widehat{\phi}_l(t_\Delta) \right)^\top \\ &= \sqrt{\frac{T}{\Delta}} \mathbf{C} \mathbf{v}_l \\ &= \sqrt{\frac{T}{\Delta}} \Lambda_l \mathbf{v}_l \\ &= \left(\frac{T}{\Delta} \Lambda_l \right) \left(\widehat{\phi}_l(t_1), \dots, \widehat{\phi}_l(t_\Delta) \right)^\top. \end{aligned}$$

Additionally, we estimate the L defined in Eq. (5.7) by the following

$$L \approx \widehat{L} \stackrel{\text{def}}{=} \max\{1, \widehat{\mathcal{L}}\}, \quad \widehat{\mathcal{L}} \stackrel{\text{def}}{=} \min \left\{ l = 1, \dots, \Delta \left| \frac{\sum_{l'=1}^l \max\{\widehat{\lambda}_{l'}, 0\}}{\sum_{l''=1}^{\Delta} \max\{\widehat{\lambda}_{l''}, 0\}} > 0.95 \right. \right\}, \quad (\text{F.4})$$

where we use $\max\{\widehat{\lambda}_{l''}, 0\}$ to compensate for when the estimated eigenvalues may be numerically negative in applications. We estimate the $\xi_{l,i}$ defined in Eq. (5.6) by the following

$$\xi_{l,i} \approx \widehat{\xi}_{l,i} \stackrel{\text{def}}{=} \frac{1}{\sqrt{2\widehat{\lambda}_l}} \cdot \frac{T}{\Delta} \sum_{q=1}^{\Delta} \left\{ \text{SECT}(K_i^{(1)})(\widehat{\nu}^*, t_q) - \text{SECT}(K_i^{(2)})(\widehat{\nu}^*, t_q) \right\} \widehat{\phi}_l(t_q), \quad (\text{F.5})$$

for $l = 1, \dots, \widehat{L}$ and $i = 1, \dots, n$. Then, we implement the χ^2 -test in Eq. (5.9) as follows

$$\sum_{l=1}^{\widehat{L}} \left(\frac{1}{\sqrt{n}} \sum_{i=1}^n \widehat{\xi}_{l,i} \right)^2 > \chi_{\widehat{L}, 1-\alpha}^2 = \text{the } 1 - \alpha \text{ lower quantile of the } \chi_{\widehat{L}}^2 \text{ distribution.} \quad (\text{F.6})$$

We encapsulate the numerical procedures for the χ^2 -test above by Algorithm 1.

Algorithm 1 : χ^2 -test.

Input: (i) SECT of two collection of shapes $\{\text{SECT}(K_i^{(j)})(\nu_p, t_q) : p = 1, \dots, \Gamma \text{ and } q = 1, \dots, \Delta\}_{i=1}^n$ for $j \in \{1, 2\}$; (ii) confidence level $1 - \alpha$ with $\alpha \in (0, 1)$.

Output: Accept or Reject the null hypothesis H_0 in Eq. (5.2).

- 1: For each $j \in \{1, 2\}$, compute $\widehat{m}_{\nu_p}^{(j)}(t_q) \stackrel{\text{def}}{=} \text{sample mean of } \{\text{SECT}(K_i^{(j)})(\nu_p; t_q)\}_{i=1}^n$ across $i \in \{1, \dots, n\}$.
 - 2: Compute the estimated distinguishing direction $\widehat{\nu}^*$ using Eq. (F.1).
 - 3: Compute $\mathbf{C} = (\widehat{\Xi}_{\nu^*}(t_{q'}, t_q))_{q, q'=1, \dots, \Delta}$ using Eq. (F.2).
 - 4: Compute the eigenvectors $\{\mathbf{v}_l\}_{l=1}^{\Delta}$ and eigenvalues $\{\Lambda_l\}_{l=1}^{\Delta}$ of the matrix \mathbf{C} .
 - 5: Compute $\widehat{\phi}_l(t_q) \stackrel{\text{def}}{=} \sqrt{\frac{\Delta}{T}} v_{l,q}$ and $\widehat{\lambda}_l \stackrel{\text{def}}{=} \frac{T}{\Delta} \Lambda_l$ for all $l = 1, \dots, \Delta$.
 - 6: Compute \widehat{L} using Eq. (F.4).
 - 7: Compute $\{\xi_{l,i} : l = 1, \dots, \widehat{L}\}_{i=1}^n$ using Eq. (F.5), test null H_0 using Eq. (F.6), and report the output.
-

In addition to the χ^2 -test detailed in Algorithm 1, we also propose a permutation-based test as an alternative approach for assessing the statistical hypotheses in Eq. (5.2). The main idea behind the permutation test is that, under the null hypothesis, shuffling the group labels of shapes should not heavily change the test statistic of interest. To perform the permutation-based test, we first apply Algorithm 1 to our original data and then repeatedly re-apply Algorithm 1 to shapes with shuffled labels.^{§*} We then compare how

^{§*}: When we apply Algorithm 1 to the original SECT, the result of Eq. (F.4) is denoted as \widehat{L}_0 . When we apply Algorithm 1 to the shuffled SECT, the \widehat{L} resulting from Eq. (F.4) may differ from \widehat{L}_0 . To make

the test statistics derived from the original differ from those computed on the shuffled data. The details of this permutation-based approach are provided in Algorithm 2. Simulation studies in Section 6 show that Algorithm 2 can eliminate the moderate type I error inflation of Algorithm 1; however, the power under the alternative for Algorithm 2 is moderately weaker than that of Algorithm 1.

Algorithm 2 : Permutation-based χ^2 -test.

Input: (i) SECT of two collections of shapes $\{\text{SECT}(K_i^{(j)})(\nu_p, t_q) : p = 1, \dots, \Gamma \text{ and } q = 1, \dots, \Delta\}_{i=1}^n$ for $j \in \{1, 2\}$; (ii) desired confidence level $1 - \alpha$ with significance $\alpha \in (0, 1)$; (iii) the number of permutations Π .

Output: Accept or Reject the null hypothesis H_0 in Eq. (5.2).

- 1: Apply Algorithm 1 to the original input SECT data, compute \widehat{L}_0 using Eq. (F.4) (see footnote §), and compute the χ^2 -test statistic denoted as \mathfrak{S}_0 using Eq. (F.6).
 - 2: **for all** $k = 1, \dots, \Pi$, **do**
 - 3: Randomly permute the group labels $j \in \{1, 2\}$ of the input SECT data.
 - 4: Apply Algorithm 1 to the permuted SECT data while setting \widehat{L} to be the \widehat{L}_0 , instead of using Eq. (F.4), and compute a χ^2 -test statistic \mathfrak{S}_k using Eq. (F.6).
 - 5: **end for**
 - 6: Sort the sequence $\{\mathfrak{S}_k\}_{k=1}^{\Pi}$ into ascending order, i.e., we have the ordered values $\{\mathfrak{S}_{(k)}\}_{k=1}^{\Pi}$ such that $\mathfrak{S}_{(1)} \leq \mathfrak{S}_{(2)} \leq \dots \leq \mathfrak{S}_{(\Pi)}$.
 - 7: Compute $k^* \stackrel{\text{def}}{=} \lceil (1 - \alpha) \cdot \Pi \rceil \stackrel{\text{def}}{=} \text{the largest integer smaller than } (1 - \alpha) \cdot \Pi$.
 - 8: **Reject** the null hypothesis H_0 if $\mathfrak{S}_0 > \mathfrak{S}_{(k^*)}$ and report the output.
-

the comparison between \mathfrak{S}_0 and $\mathfrak{S}_{(k^*)}$ fair (see the last step of Algorithm 2), we set \widehat{L} to be \widehat{L}_0 .

G Randomization-style Null Hypothesis

Significance Test

In Section 6, we compare our proposed Algorithms 1 and 2 with the “randomization-style null hypothesis significance test (NHST)” (Robinson and Turner, 2017, particularly Section 5.3 therein), which is designed to test the following hypotheses

$$H_0: \mathbb{P}^{(1)} = \mathbb{P}^{(2)} \quad \text{vs.} \quad H_1: \mathbb{P}^{(1)} \neq \mathbb{P}^{(2)}, \quad (\text{G.1})$$

The randomization-style NHST is based on the permutation test and the following loss function

$$F\left(\{K_i^{(1)}\}_{i=1}^n, \{K_i^{(2)}\}_{i=1}^n\right) \stackrel{\text{def}}{=} \frac{1}{2n(n-1)} \sum_{k,l=1}^n \left\{ \rho\left(K_k^{(1)}, K_l^{(1)}\right) + \rho\left(K_k^{(2)}, K_l^{(2)}\right) \right\}, \quad (\text{G.2})$$

where ρ is the distance function defined in Eq. (4.1).

For a given discrete ECT, where $\{\text{ECT}(K_i^{(j)})(\nu_p, t_q) : p = 1, \dots, \Gamma \text{ and } q = 1, \dots, \Delta\}_{i=1}^n$, we may adopt the following approximation

$$\rho\left(K_k^{(j)}, K_l^{(j)}\right) \approx \sup_{p=1, \dots, \Gamma} \left(\sum_{q=1}^{\Delta} \left| \text{ECT}(K_k^{(j)})(\nu_p, t_q) - \text{ECT}(K_l^{(j)})(\nu_p, t_q) \right|^2 \right)^{1/2}. \quad (\text{G.3})$$

We apply Algorithm 3 to implement the randomization-style NHST.

H Landmark-based Permutation Test

Landmarks are widely used in geometric morphometrics (Kendall, 1977, 1984, 1989; Gao et al., 2019b,a). In this section, we introduce a landmark-based hypothesis testing approach for distinguishing between shape collections. We compare this approach with our proposed Algorithm 1 and 2 using the mandibular molar data presented in Figure 1.1 (see Section 7). This section is divided into the following two subsections:

Algorithm 3 : Randomization-style NHST

Input: (i) ECT of two collection of shapes $\{\text{ECT}(K_i^{(j)})(\nu_p, t_q) : p = 1, \dots, \Gamma \text{ and } q = 1, \dots, \Delta\}_{i=1}^n$ for $j \in \{1, 2\}$; (ii) confidence level $1 - \alpha$ with $\alpha \in (0, 1)$; (iii) the number of permutations Π .

Output: Accept or Reject the null hypothesis H_0 in Eq. (G.1).

- 1: Apply Eq. (G.2) and Eq. (G.3) to the original input ECT data and compute the value of the loss $\mathfrak{S}_0 \stackrel{\text{def}}{=} F(\{K_i^{(1)}\}_{i=1}^n, \{K_i^{(2)}\}_{i=1}^n)$.
 - 2: **for all** $k = 1, \dots, \Pi$, **do**
 - 3: Randomly permute the group labels $j \in \{1, 2\}$ of the input ECT data.
 - 4: Apply Eq. (G.2) and Eq. (G.3) to the permuted ECT data and compute the corresponding value of the loss function F ; denote the value of the loss by \mathfrak{S}_k .
 - 5: **end for**
 - 6: Sort the sequence $\{\mathfrak{S}_k\}_{k=1}^{\Pi}$ into ascending order, i.e., we have the ordered values $\{\mathfrak{S}_{(k)}\}_{k=1}^{\Pi}$ such that $\mathfrak{S}_{(1)} \leq \mathfrak{S}_{(2)} \leq \dots \leq \mathfrak{S}_{(\Pi)}$.
 - 7: Compute $k^* \stackrel{\text{def}}{=} \lceil \alpha \cdot \Pi \rceil \stackrel{\text{def}}{=} \text{the largest integer smaller than } \alpha \cdot \Pi$.
 - 8: **Reject** the null hypothesis H_0 if $\mathfrak{S}_0 < \mathfrak{S}_{(k^*)}$ and report the output.
-

- In Section H.1, motivated by Robinson and Turner (2017), we propose a permutation test based on Procrustes distances, which is presented in Algorithm 4.
- In Section H.2, we first use the ‘‘Gaussian process landmarking (GPL) algorithm’’ (Gao et al., 2019b,a) to generate landmarks on the mandibular molars analyzed in Section 7. Then, we apply the ‘‘bounded distortion Gaussian process landmark matching’’ method (Gao et al., 2019a, Section 4.2) to generate the correspondence between each pair of mandibular molars. Lastly, we implement the continuous Procrustes distance ϱ_P induced by the correspondence. The Procrustes distance ϱ_P can

be used as an input to Algorithm 4.

H.1 Permutation Test Using Landmark-based Distances

In this subsection, to test the hypotheses in Eq. (G.1), we propose a permutation test using landmark-based distances. Similar to Algorithm 3, we need the following loss function

$$G\left(\{K_i^{(1)}\}_{i=1}^n, \{K_i^{(2)}\}_{i=1}^n\right) \stackrel{\text{def}}{=} \frac{1}{2n(n-1)} \sum_{k,l=1}^n \left\{ \varrho\left(K_k^{(1)}, K_l^{(1)}\right) + \varrho\left(K_k^{(2)}, K_l^{(2)}\right) \right\}, \quad (\text{H.1})$$

where $\{K_i^{(j)}\}_{i=1}^n \stackrel{\text{i.i.d.}}{\sim} \mathbb{P}^{(j)}$, for $j \in \{1, 2\}$, and the ϱ is a landmark-based distance. A comprehensive description of the permutation test using landmark-based distances is given in Algorithm 4. An example of the landmark-based distance ϱ is the continuous Procrustes distance ϱ_P defined in Section H.2.

H.2 Gaussian Process-based Landmarks and Correspondence

This subsection is designed for the landmark-based analysis of mandibular molars presented in Section 7. In this section, we briefly introduce the ‘‘Gaussian process landmarking (GPL) algorithm’’ and ‘‘bounded distortion GPL matching’’ method that were developed in Gao et al. (2019b) and Gao et al. (2019a). Following this, a continuous Procrustes distance (Alifari et al., 2013) is defined to measure the dissimilarity between each pair of mandibular molars.

H.2.1 Gaussian process landmarking algorithm

The GPL algorithm and its applications to the anatomical surfaces represented by discrete triangular meshes have been developed in Gao et al. (2019b) and Gao et al. (2019a). The algorithm is comprehensively described in Algorithm 2.1 of Gao et al. (2019a), which is the one implemented in our paper. Briefly, the GPL algorithm takes a triangular mesh of

Algorithm 4 : Permutation test using landmark-based Procrustes distances

Input: (i) Landmark-based distance ϱ ; (ii) confidence level $1 - \alpha$ with significance $\alpha \in (0, 1)$; (iii) the number of permutations Π .

Output: Accept or Reject the null hypothesis H_0 in Eq. (G.1).

- 1: Compute the value of the loss function in Eq. (H.1) using the original (un-shuffled) shapes. That is, compute the distances $\{\varrho(K_k^{(1)}, K_l^{(1)})\}_{k,l=1}^n$ and $\{\varrho(K_k^{(2)}, K_l^{(2)})\}_{k,l=1}^n$; then, compute the value $\mathfrak{S}_0 \stackrel{\text{def}}{=} G(\{K_i^{(1)}\}_{i=1}^n, \{K_i^{(2)}\}_{i=1}^n)$ using Eq. (H.1).
 - 2: **for all** $k = 1, \dots, \Pi$, **do**
 - 3: Randomly permute the group labels $j \in \{1, 2\}$ of the shapes $\{K_i^{(j)}\}_{i,j}$.
 - 4: Apply Eq. (H.1) to the permuted shapes and compute the corresponding value of the loss function G ; denote the value of the loss by \mathfrak{S}_k .
 - 5: **end for**
 - 6: Sort the sequence $\{\mathfrak{S}_k\}_{k=1}^\Pi$ into ascending order, i.e., we have the ordered values $\{\mathfrak{S}_{(k)}\}_{k=1}^\Pi$ such that $\mathfrak{S}_{(1)} \leq \mathfrak{S}_{(2)} \leq \dots \leq \mathfrak{S}_{(\Pi)}$.
 - 7: Compute $k^* \stackrel{\text{def}}{=} \lceil \alpha \cdot \Pi \rceil \stackrel{\text{def}}{=} \text{the largest integer smaller than } \alpha \cdot \Pi$.
 - 8: **Reject** the null hypothesis H_0 if $\mathfrak{S}_0 < \mathfrak{S}_{(k^*)}$ and report the output.
-

interest and the number of desired landmarks (which is set to be 40 in both Gao et al. (2019a) and our paper) as inputs; it returns feature vertices (called landmarks) of the triangular mesh as the output. Figure 1 of Gao et al. (2019a) gives an example visually showing the performance of the GPL algorithm.

H.2.2 Procrustes distance induced by the Gaussian Process-based Landmarks and Correspondence

In addition to the GPL algorithm, Gao et al. (2019a) also introduced the “bounded distortion GPL matching” method (Section 4.2 therein) to construct a correspondence map

f using the sampled landmarks. Specifically, suppose we are interested in two anatomical surfaces K_1 and K_2 , which are the shapes of interest; landmarks $\{\zeta_i^{(1)}\}_{i=1}^{40}$ and $\{\zeta_i^{(2)}\}_{i=1}^{40}$ are sampled from the K_1 and K_2 , respectively, using the GPL algorithm;* the bounded distortion GPL matching method returns a correspondence map $f : K_1 \rightarrow K_2$ using these landmarks as input.

With the obtained correspondence map $f : K_1 \rightarrow K_2$, we may compute the following continuous Procrustes distance (also see [Al-Aifari et al. \(2013\)](#) and Eq. (4.3) of [Gao et al. \(2019a\)](#))

$$\varrho_P(K_1, K_2) \stackrel{\text{def}}{=} \left(\inf_{\varphi \in \mathbb{E}(3)} \int_{K_1} \|f(x) - \varphi(x)\|^2 d\text{vol}_{K_1}(x) \right)^{1/2}, \quad (\text{H.2})$$

where $d\text{vol}_{K_1}$ denotes the volume form of the surface K_1 .

In this paper, we compute ϱ_P using the approach proposed in [Gao et al. \(2019a\)](#). Specifically, we implement the code provided in the GitHub repository of the authors.

I Applications to Silhouette Database

We use a subset of the silhouette database that includes three classes of shapes: apples, hearts, and children (see Supplementary Figure [I.1](#); each class has 20 shapes). For each shape shown in Supplementary Figure [I.1](#), we compute its SECT. Specifically, we compute the ECCs for 72 directions, evenly sampled over the interval $[0, 2\pi]$. For each direction, we analyze 100 sublevel sets. We apply Algorithm [1](#) and [2](#) to test the hypothesis that shapes differ between classes and present the results in Table [I.1](#). The p-values in Table [I.1](#) are either χ^2 -test p-values (from Algorithm [1](#)) or permutation-test p-values (from Algorithm [2](#) with $\Pi = 1000$). In addition to testing differences between shape classes, we also apply

*[Gao et al. \(2019a\)](#) set the number of landmarks on each anatomical surface to be 40 in the examples illustrated therein; we adopt the same choice.

the algorithms within each individual shape class. Specifically, for each shape class, we randomly split the class into two halves and test for differences between them using the algorithms. We repeat this random splitting procedure 100 times and present the corresponding p-values in Table I.1 (rows 4-6). For each shape class, we summarize the 100 p-values by reporting their mean with the standard deviation given in parentheses.

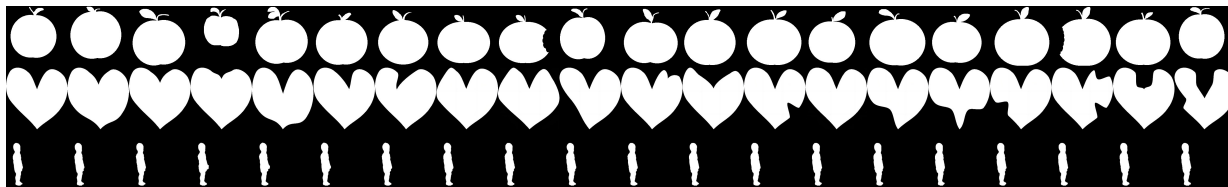


Figure I.1: Each row corresponds to one of the shape classes: apples, hearts, and children.

Table I.1: P-values of Algorithm 1 and 2 for the silhouette database.

	Algorithm 1	Algorithm 2
Apples vs. Hearts	< 0.01	< 0.01
Apples vs. Children	< 0.01	< 0.01
Hearts vs. Children	< 0.01	< 0.01
Apples vs. Apples	0.26 (0.23)	0.46 (0.27)
Hearts vs. Hearts	0.17 (0.16)	0.47 (0.29)
Children vs. Children	0.39 (0.28)	0.49 (0.30)

Rows 1-3 of Table I.1 show that our proposed Algorithm 1 and 2 can distinguish the shape classes of apples, hearts, and children presented in Supplementary Figure I.1. Rows 4-6 show that our proposed algorithms tend to minimize type I errors for the shape-valued data presented in Supplementary Figure I.1. The within-class p-values for each shape class reflect its homogeneity or heterogeneity (e.g., the class of children has the highest homogeneity among all three shape classes). Algorithm 2 tends to have larger p-values

than Algorithm 1 when applied within each shape class, which is essentially due to the permutation procedure implemented in Algorithm 2.

J Numerical Experiments on the ANOVA for Functional Data — Existing Methods vs. Our Proposed Methods

In this section, we compare our proposed Algorithms 1 and 2 with twelve existing fdANOVA methods, which are listed below (also see [Górecki and Smaga, 2019](#)):

- FP: permutation test based on a basis function representation and an F-statistic ([Górecki and Smaga, 2015](#)).
- CH and CS: L^2 -norm-based parametric bootstrap tests for homoscedastic and heteroscedastic samples, respectively ([Cuevas et al., 2004](#)).
- L2N and L2B: L^2 -norm-based test with naive and bias-reduced method of estimation, respectively ([Faraway, 1997](#); [Zhang and Chen, 2007](#); [Zhang, 2013](#)).
- L2b: L^2 -norm-based bootstrap test ([Zhang, 2013](#)).
- FN and FB: F-type test with naive and bias-reduced method of estimation, respectively ([Shen and Faraway, 2004](#); [Zhang, 2011](#)).
- Fb: F-type bootstrap test ([Zhang, 2013](#)).
- TRP: tests based on random projections ([Cuesta-Albertos and Febrero-Bande, 2010](#)). TRP-ANOVA indicates the TRP test using the ANOVA F statistic; TRP-ATS indicates the TRP test using the ANOVA-type statistic (ATS) proposed by [Brunner](#)

et al. (1997). TRP-WTPS indicates the TRP test using the Wald-type permutation statistic (WTPS) of Pauly et al. (2014).

These existing methods are implemented using the R package `fdANOVA` (Górecki and Smaga, 2019). Further details regarding these methods are available in Górecki and Smaga (2019). As stated within Górecki and Smaga (2019): “satisfactory results are usually obtained by using the default values”; as a result, we use the default parameters provided by the package `fdANOVA`.

The application of the `fdANOVA` methods to the SECT is described in Section 5. The distributions that generate the simulated shapes in our numerical experiments are described in Section 6, particularly in Eq. (6.1). The rejection rates of Algorithms 1, 2, 3, and the existing `fdANOVA` methods in different settings are presented in Table J.1, which complements the results in Table 6.1. Notably, $\varepsilon = 0$ indicates that the simulated shapes are generated under the null hypothesis. These rejection rates are also depicted in Figure 6.1.

K Trade-off Studies for Algorithms 1 and 2 — Numbers of Directions and Levels, Sample Sizes, and Computational Cost

In this section, we study the trade-offs among the following quantities using simulations:

- Runtimes/computational cost.
- Number Γ of directions.
- Number Δ of levels.

Table J.1: Rejection rates (from 1000 experiments) for different indices ε (significance $\alpha = 0.05$).

Indices ε	0.00	0.01	0.02	0.03	0.04	0.05	0.06	0.08	0.10
Algorithm 1	0.118	0.161	0.315	0.519	0.785	0.910	0.975	0.990	1.000
Algorithm 2	0.046	0.054	0.162	0.343	0.612	0.789	0.931	0.994	1.000
Algorithm 3	0.050	0.050	0.111	0.185	0.335	0.535	0.739	0.983	0.999
FP	0.136	0.153	0.308	0.539	0.810	0.924	0.986	0.997	1.000
CH	0.136	0.141	0.309	0.539	0.806	0.927	0.985	0.997	1.000
CS	0.139	0.148	0.318	0.547	0.807	0.933	0.985	0.997	1.000
L2N	0.138	0.147	0.319	0.550	0.809	0.931	0.985	0.997	1.000
L2B	0.139	0.155	0.321	0.557	0.810	0.933	0.985	0.997	1.000
L2b	0.138	0.147	0.319	0.551	0.803	0.929	0.985	0.997	1.000
FN	0.136	0.144	0.316	0.544	0.807	0.929	0.985	0.997	1.000
FB	0.138	0.147	0.318	0.546	0.808	0.929	0.985	0.997	1.000
Fb	0.138	0.139	0.309	0.541	0.802	0.925	0.984	0.997	1.000
TRP-ANOVA	0.073	0.091	0.256	0.510	0.782	0.931	0.980	0.997	1.000
TRP-ATS	0.076	0.093	0.258	0.519	0.785	0.932	0.982	0.997	1.000
TRP-WTPS	0.075	0.091	0.261	0.515	0.790	0.929	0.980	0.997	1.000

- Number n of shape pairs.

Using the random shape-generating mechanism introduced in Section 6, we simulate a data set for each fixed sample size $n \in \{25, 50, 100\}$ and fixed $\varepsilon \in \{0, 0.05\}$. Specifically, the simulated data set is given by $\{(K_i^{(0)}, K_i^{(\varepsilon)})\}_{i=1}^n \stackrel{iid}{\sim} \mathbb{P}^{(0)} \otimes \mathbb{P}^{(\varepsilon)}$. Using the simulated data set, we then apply Algorithm 1 and 2 to test the following the hypotheses, considering different combinations of $\Gamma \in \{2, 4, 8\}$ and $\Delta \in \{25, 50, 100\}$.

$$H_0 : m_\nu^{(0)}(t) = m_\nu^{(\varepsilon)}(t) \text{ for all } (\nu, t) \in \mathbb{S}^{d-1} \times [0, T] \quad (\text{K.1})$$

$$\text{vs. } H_1 : m_\nu^{(0)}(t) \neq m_\nu^{(\varepsilon)}(t) \text{ for some } (\nu, t).$$

We repeat this procedure 20 times and explore all the combinations of $n \in \{25, 50, 100\}$, $\Gamma \in \{2, 4, 8\}$, and $\Delta \in \{25, 50, 100\}$. The simulation results are presented in Tables K.1, K.2, and K.3 and summarized as follows:

- i) For each input combination of n , Γ , and Δ for each algorithm, the mean and standard deviation (in parentheses) of the runtimes across the 20 simulations are presented in Table K.1.
- ii) For each input combination of n , Γ , and Δ for each algorithm and when $\epsilon = 0.05$, the mean and standard deviation (in parentheses) of the p-values across the 20 simulations are presented in Table K.2. This table presents the trade-offs between the accuracy of our algorithms (in terms of p-values), sample size n , number Γ of directions, and number Δ of levels under the alternative hypothesis H_1 in Eq. (K.1) with $\epsilon = 0.05$. The p-values in Table K.2 demonstrate that the larger the n , Δ , and Γ , the more likely Algorithm 1 and 2 reject the null hypothesis H_0 in Eq. (K.1). Particularly, with a significance of $\alpha = 0.05$, only $\Gamma = 4$ directions are sufficient for Algorithm 1 and 2 to reject H_0 when $\Delta = 100$ and $n = 50$. Therefore, we adopt $\Gamma = 4$ for the proof-of-concept purpose in our simulation studies presented in Section 6.
- iii) For each input combination of n , Γ , and Δ for each algorithm and when $\epsilon = 0$, the mean and standard deviation (in parentheses) of the p-values across the 20 simulations are presented in Table K.3. This table presents the trade-offs between the accuracy of our algorithms (in terms of p-values), sample size n , number Γ of directions, and number Δ of levels under the null hypothesis $H_0 : \mathbb{P}^{(0)} = \mathbb{P}^{(\epsilon)}$ with $\epsilon = 0$. The p-values in Table K.3 demonstrate that no matter how small or large the n , Δ , and Γ are, neither Algorithm 1 nor 2 tends to distinguish $\mathbb{P}^{(0)}$ and $\mathbb{P}^{(\epsilon)}$ with $\epsilon = 0$ falsely.

The source code for the this study is publically available online through the link provided in the “Software Availability” section. This study is conducted on a computer with an AMD Ryzen 7 5800H processor running at 3200 MHz using 16 GB of RAM, running Windows version 21H2.

Table K.1: Runtimes of Algorithm 1 and 2 (in seconds) based on Γ , Δ , and n .

Algorithm 1				
Number of directions	Number of levels	$n = 25$	$n = 50$	$n = 100$
$\Gamma = 2$	$\Delta = 25$	0.75 (0.10)	1.40 (0.08)	2.23 (0.09)
	$\Delta = 50$	1.26 (0.09)	2.36 (0.08)	4.25 (0.10)
	$\Delta = 100$	2.32 (0.09)	4.52 (0.15)	8.10 (0.21)
$\Gamma = 4$	$\Delta = 25$	1.25 (0.09)	2.26 (0.08)	4.13 (0.15)
	$\Delta = 50$	2.26 (0.09)	4.29 (0.14)	8.00 (0.18)
	$\Delta = 100$	4.28 (0.13)	8.31 (0.17)	15.77 (0.29)
$\Gamma = 8$	$\Delta = 25$	2.27 (0.10)	4.25 (0.12)	8.06 (0.21)
	$\Delta = 50$	4.32 (0.13)	8.39 (0.17)	15.81 (0.14)
	$\Delta = 100$	8.38 (0.12)	16.69 (0.34)	32.69 (1.16)
Algorithm 2				
Number of directions	Number of levels	$n = 25$	$n = 50$	$n = 100$
$\Gamma = 2$	$\Delta = 25$	1.53 (0.14)	2.89 (0.11)	4.20 (0.13)
	$\Delta = 50$	2.69 (0.12)	4.18 (0.15)	7.34 (0.24)
	$\Delta = 100$	4.89 (0.25)	9.12 (0.26)	13.89 (0.83)
$\Gamma = 4$	$\Delta = 25$	2.07 (0.17)	3.55 (0.15)	6.16 (0.18)
	$\Delta = 50$	3.52 (0.21)	6.31 (0.13)	11.19 (0.28)
	$\Delta = 100$	6.97 (0.22)	12.60 (0.67)	21.62 (1.39)
$\Gamma = 8$	$\Delta = 25$	3.12 (0.13)	5.64 (0.19)	10.22 (0.22)
	$\Delta = 50$	5.64 (0.17)	10.46 (0.16)	19.36 (0.48)
	$\Delta = 100$	11.05 (0.17)	20.42 (0.31)	37.85 (1.87)

Table K.2: P-value of Algorithm 1 and 2 based on Γ , Δ , and n . ($\varepsilon = 0.05$)

Algorithm 1				
Number of directions	Number of levels	$n = 25$	$n = 50$	$n = 100$
$\Gamma = 2$	$\Delta = 25$	0.3487 (0.2618)	0.1804 (0.2659)	0.0612 (0.1072)
	$\Delta = 50$	0.1696 (0.2205)	0.1502 (0.2350)	0.0179 (0.0357)
	$\Delta = 100$	0.1224 (0.1383)	0.0565 (0.0948)	0.0123 (0.0251)
$\Gamma = 4$	$\Delta = 25$	0.1909 (0.1964)	0.1367 (0.1626)	0.0656 (0.0933)
	$\Delta = 50$	0.1414 (0.1693)	0.1250 (0.1861)	0.0070 (0.0119)
	$\Delta = 100$	0.1747 (0.2432)	0.0517 (0.0703)	0.0056 (0.0147)
$\Gamma = 8$	$\Delta = 25$	0.2773 (0.2425)	0.1130 (0.1770)	0.0294 (0.0561)
	$\Delta = 50$	0.1064 (0.1140)	0.0533 (0.0929)	0.0179 (0.0235)
	$\Delta = 100$	0.1371 (0.2053)	0.0296 (0.0694)	0.0044 (0.0125)
Algorithm 2				
Number of directions	Number of levels	$n = 25$	$n = 50$	$n = 100$
$\Gamma = 2$	$\Delta = 25$	0.3582 (0.2710)	0.1942 (0.1807)	0.0600 (0.1052)
	$\Delta = 50$	0.2156 (0.1863)	0.1704 (0.2030)	0.0385 (0.0950)
	$\Delta = 100$	0.2067 (0.1984)	0.0883 (0.1186)	0.0601 (0.2046)
$\Gamma = 4$	$\Delta = 25$	0.3102 (0.2727)	0.3664 (0.2714)	0.1970 (0.2644)
	$\Delta = 50$	0.3282 (0.3152)	0.1445 (0.1841)	0.0364 (0.1141)
	$\Delta = 100$	0.3250 (0.3197)	0.0728 (0.1225)	0.0194 (0.0676)
$\Gamma = 8$	$\Delta = 25$	0.3704 (0.3408)	0.2533 (0.2406)	0.2138 (0.2670)
	$\Delta = 50$	0.2108 (0.2354)	0.1437 (0.2147)	0.0373 (0.0665)
	$\Delta = 100$	0.2107 (0.2843)	0.1613 (0.2141)	0.0186 (0.0567)

Table K.3: P-value of Algorithm 1 and 2 based on Γ , Δ , and n . ($\varepsilon = 0$)

Algorithm 1				
Number of directions	Number of levels	$n = 25$	$n = 50$	$n = 100$
$\Gamma = 2$	$\Delta = 25$	0.3826 (0.2486)	0.3712 (0.2770)	0.4374 (0.2333)
	$\Delta = 50$	0.3943 (0.2425)	0.3725 (0.2448)	0.3234 (0.2493)
	$\Delta = 100$	0.3209 (0.2122)	0.3947 (0.2432)	0.5072 (0.3393)
$\Gamma = 4$	$\Delta = 25$	0.2513 (0.2415)	0.4025 (0.2906)	0.2910 (0.2347)
	$\Delta = 50$	0.3060 (0.2171)	0.2694 (0.2351)	0.4245 (0.2508)
	$\Delta = 100$	0.2855 (0.2420)	0.2357 (0.2230)	0.3426 (0.2939)
$\Gamma = 8$	$\Delta = 25$	0.2431 (0.2237)	0.2711 (0.2784)	0.3265 (0.2509)
	$\Delta = 50$	0.3199 (0.2110)	0.2430 (0.1694)	0.3367 (0.2481)
	$\Delta = 100$	0.2507 (0.2215)	0.3212 (0.2307)	0.4346 (0.2546)
Algorithm 2				
Number of directions	Number of levels	$n = 25$	$n = 50$	$n = 100$
$\Gamma = 2$	$\Delta = 25$	0.4278 (0.2947)	0.4764 (0.2830)	0.4921 (0.2359)
	$\Delta = 50$	0.5637 (0.3072)	0.5866 (0.2655)	0.5510 (0.3005)
	$\Delta = 100$	0.3028 (0.2026)	0.5540 (0.2932)	0.4155 (0.2892)
$\Gamma = 4$	$\Delta = 25$	0.5738 (0.3467)	0.5293 (0.2335)	0.4714 (0.2967)
	$\Delta = 50$	0.4489 (0.2582)	0.4639 (0.3050)	0.4669 (0.3310)
	$\Delta = 100$	0.5193 (0.2830)	0.5579 (0.2984)	0.5557 (0.2215)
$\Gamma = 8$	$\Delta = 25$	0.4786 (0.2669)	0.4782 (0.3068)	0.4721 (0.3296)
	$\Delta = 50$	0.3867 (0.2768)	0.4543 (0.3116)	0.5324 (0.2943)
	$\Delta = 100$	0.6138 (0.2375)	0.5110 (0.2581)	0.4109 (0.2592)

L Proofs

L.1 Proof of Theorem C.1

Proof of Theorem C.1. Since $H_0^1([0, T])$ is a separable Hilbert space (Brezis, 2011, Section 8.3), it suffices to show the results (i) and (ii).

The separability of \mathcal{H} implies that \mathcal{H} has an orthonormal basis $\{\mathbf{e}_j\}_{j=1}^{\infty}$ (Brezis, 2011, Theorem 5.11). Since $C(\mathbb{S}^{d-1}) = C(\mathbb{S}^{d-1}; \mathbb{R})$ is separable (Brezis, 2011, Section 3.6), $C(\mathbb{S}^{d-1})$ has a dense and countable subset D . Then, the linear hull $\tilde{D} \stackrel{\text{def}}{=} \text{span}\{g\mathbf{e}_j \mid g \in D \text{ and } j = 1, 2, \dots\}$ is a dense and countable subset of $C(\mathbb{S}^{d-1}; \mathcal{H})$, and the reasoning is the following.

For any $f \in C(\mathbb{S}^{d-1}; \mathcal{H})$, we have

$$f(\nu) = \sum_{j=1}^{\infty} \langle f(\nu), \mathbf{e}_j \rangle \mathbf{e}_j, \quad \text{for each } \nu \in \mathbb{S}^{d-1},$$

where $\langle \cdot, \cdot \rangle$ denotes the inner product of \mathcal{H} and $\sum_{j=1}^{\infty}$ converges in the \mathcal{H} -topology. It is straightforward that the function $\nu \mapsto \langle f(\nu), \mathbf{e}_j \rangle$ is an element of $C(\mathbb{S}^{d-1})$, for each fixed $j = 1, 2, \dots$. Hence, for any $\epsilon > 0$, there exists $\{g_j\}_{j=1}^{\infty} \subseteq D$ such that

$$\sup_{\nu \in \mathbb{S}^{d-1}} |\langle f(\nu), \mathbf{e}_j \rangle - g_j(\nu)| < \frac{\epsilon}{2^{j+1}},$$

for all $j = 1, 2, \dots$, which implies

$$\begin{aligned} \left\| f - \sum_{j=1}^{\infty} g_j \mathbf{e}_j \right\|_{C(\mathbb{S}^{d-1}; \mathcal{H})} &= \sup_{\nu \in \mathbb{S}^{d-1}} \left\| f(\nu) - \sum_{j=1}^{\infty} g_j(\nu) \mathbf{e}_j \right\|_{\mathcal{H}} \\ &= \sup_{\nu \in \mathbb{S}^{d-1}} \left\| \sum_{j=1}^{\infty} (\langle f(\nu), \mathbf{e}_j \rangle - g_j(\nu)) \mathbf{e}_j \right\|_{\mathcal{H}} \\ &\leq \sup_{\nu \in \mathbb{S}^{d-1}} \sum_{j=1}^{\infty} |\langle f(\nu), \mathbf{e}_j \rangle - g_j(\nu)| < \epsilon. \end{aligned}$$

Since $\{\sum_{j=1}^n g_j \mathbf{e}_j\}_{n=1}^{\infty} \subseteq \tilde{D}$, the proof of result (i) is complete.

The result (ii) can be proved using the same trick implemented in the proof of result (i). The proof is complete. \square

L.2 An Elementary Proof of Eq. (2.1)

Proof of Eq. (2.1). For any $f \in \mathcal{H} = H_0^1([0, T]) = \{f \in L^2([0, 1]) \mid f' \in L^2([0, T]) \text{ and } f(0) = f(T) = 0\}$, we identify f as a continuous function defined on the compact interval $[0, T]$

(see Section A.1, also Theorem 8.2 of Brezis (2011), for a justification). It suffices to show

$$\|f\|_{C^{0,\frac{1}{2}}([0,T])} \leq \tilde{C}_T \cdot \|f\|_{\mathcal{H}} \text{ for some constant } \tilde{C}_T \text{ depending only on } T.$$

Theorem 8.2 of Brezis (2011) implies

$$f(t) - f(s) = \int_s^t f'(\tau) d\tau, \quad \text{for all } s, t \in [0, T], \quad (\text{L.1})$$

where f' denotes the weak derivative of f . Without loss of generality, we assume $s < t$ in

Eq. (L.1). $f(0) = 0$ and Eq. (L.1) imply the following inequalities for all $t \in [0, T]$

$$\begin{aligned} |f(t)| &= \left| \int_0^t f'(\tau) d\tau \right| \\ &\leq \int_0^T |f'(\tau)| d\tau \\ &\leq \sqrt{T} \cdot \left(\int_0^T |f'(\tau)|^2 d\tau \right)^{1/2} \\ &= \sqrt{T} \cdot \|f\|_{\mathcal{H}}. \end{aligned}$$

Hence, $\sup_{t \in [0, T]} |f(t)| \leq \sqrt{T} \cdot \|f\|_{\mathcal{H}}$. Again, Eq. (L.1) implies

$$\begin{aligned} |f(t) - f(s)| &= \left| \int_s^t f'(\tau) d\tau \right| \\ &\leq \sqrt{t-s} \cdot \left(\int_s^t |f'(\tau)|^2 d\tau \right)^{1/2} \\ &\leq \sqrt{t-s} \cdot \left(\int_0^T |f'(\tau)|^2 d\tau \right)^{1/2} \\ &= \sqrt{t-s} \cdot \|f\|_{\mathcal{H}}. \end{aligned}$$

Therefore, we have

$$\sup_{s, t \in [0, T] \text{ and } s \neq t} \left(\frac{|f(t) - f(s)|}{\sqrt{|t-s|}} \right) \leq \|f\|_{\mathcal{H}},$$

which implies

$$\|f\|_{C^{0,\frac{1}{2}}([0,T])} = \sup_{t \in [0, T]} |f(t)| + \sup_{s, t \in [0, T] \text{ and } s \neq t} \left(\frac{|f(t) - f(s)|}{\sqrt{|t-s|}} \right) \leq (1 + \sqrt{T}) \cdot \|f\|_{\mathcal{H}}.$$

The desired Eq. (2.1) follows (i.e., $\tilde{C}_T = 1 + \sqrt{T}$). \square

L.3 Proof of Theorem C.2

We recall that the discontinuities of $t \mapsto \beta_k(K_t^\nu)$ and $t \mapsto \chi(K_t^\nu) = \chi_t^\nu(K)$ are the HCPs of K in direction ν (see Section A.2).

Proof of Theorem C.2. For any fixed $\nu \in \mathbb{S}^{d-1}$, the following inclusion is straightforward

$$\left(\text{Dgm}_k(K; \phi_\nu) \cap (-\infty, t) \times (t, \infty) \right) \subseteq \{ \xi \in \text{Dgm}_k(K; \phi_\nu) \mid \text{pers}(\xi) > 0 \}, \quad (\text{L.2})$$

where the function ϕ_ν is defined in Eq. (B.1), and the definitions of $\text{Dgm}_k(K; \phi_\nu)$ and $\text{pers}(\xi)$ are given in Appendix B. Together with the k-triangle lemma (Edelsbrunner et al., 2000; Cohen-Steiner et al., 2007), the inclusion in Eq. (L.2) and Condition 3.1 imply

$$\begin{aligned} \beta_k(K_t^\nu) &= \# \left(\text{Dgm}_k(K; \phi_\nu) \cap (-\infty, t) \times (t, \infty) \right) \\ &\leq \# \{ \xi \in \text{Dgm}_k(K; \phi_\nu) \mid \text{pers}(\xi) > 0 \} \\ &\leq \frac{M}{d}, \end{aligned} \quad (\text{L.3})$$

for all $k \in \{0, 1, \dots, d-1\}$ and all t that are not HCPs in direction ν , where the cardinality $\#\{\cdot\}$ counts the multiplicity of the multisets. Eq. (3.2) implies

$$\begin{aligned} |\chi_t^\nu(K)| &= \left| \sum_{k=0}^{d-1} (-1)^k \cdot \beta_k(K_t^\nu) \right| \\ &\leq d \cdot \sup_{k \in \{0, \dots, d-1\}} \beta_k(K_t^\nu) \\ &\leq M, \end{aligned} \quad (\text{L.4})$$

for all t that are not HCPs in direction ν . The right continuity of $t \mapsto \chi(K_t^\nu)$ stated in Lemma C.1, together with Eq. (L.4), implies that $|\chi_t^\nu(K)| \leq M$ holds for all $t \in [0, T]$.

Then, we have

$$\sup_{\nu \in \mathbb{S}^{d-1}} \left(\sup_{0 \leq t \leq T} |\chi_t^\nu(K)| \right) \leq M.$$

The proof is complete. \square

L.4 Proof of Lemma C.3

To prove Lemma C.3, we need the following lemma as a preparation.

Lemma L.1. *For any $K \in \mathcal{S}_{R,d}^M$ and fixed $\nu \in \mathbb{S}^{d-1}$, the function $t \mapsto \int_0^t \chi_\tau^\nu(K) d\tau$ has its first-order weak derivative $t \mapsto \chi_t^\nu(K)$.*

Proof. Because of

$$\begin{aligned} \left\{ \int_0^t \chi_\tau^\nu(K) d\tau \right\}_{t \in [0, T]} &\in \{ \text{all absolutely continuous functions on } [0, T] \} \\ &= \{ x \in L^1([0, T]) : \text{the weak derivative } x' \text{ exists and } x' \in L^1([0, T]) \} \\ &\stackrel{\text{def}}{=} W^{1,1}([0, T]) \end{aligned}$$

(see the Remark 8 after Proposition 8.3 in Brezis (2011) for details), the weak derivative of $\{ \int_0^t \chi_\tau^\nu(K) d\tau \}_{t \in [0, T]}$ exists. Lemma L.1 follows from Theorem 8.2 of Brezis (2011). \square

Remark: Using Lemma 3.1, one can verify that $\chi_t^\nu(K)$ is the classical derivative of $\int_0^t \chi_\tau^\nu(K) d\tau$ for all t except for the finitely many HCPs of K in direction ν .

With Lemma L.1, we prove Lemma C.3 as follows.

Proof of Lemma C.3. For the simplicity, we denote

$$F(t) \stackrel{\text{def}}{=} \int_0^t \chi_\tau^\nu(K) d\tau - \frac{t}{T} \int_0^T \chi_\tau^\nu(K) d\tau, \quad \text{for } t \in [0, T].$$

Theorem C.2 implies

$$|F(t)| \leq \int_0^t |\chi_\tau^\nu(K)| d\tau + \frac{t}{T} \int_0^T |\chi_\tau^\nu(K)| d\tau \leq 2TM, \quad \text{for } t \in [0, T].$$

Hence, $F \in L^p([0, T])$ for $p \in [1, \infty)$. Lemma L.1 implies that the weak derivative of F exists and is $F'(t) = \chi_t^\nu(K) - \frac{1}{T} \int_0^T |\chi_\tau^\nu(K)| d\tau$. We have the boundedness

$$|F'(t)| \leq |\chi_t^\nu(K)| + \frac{1}{T} \int_0^T |\chi_\tau^\nu(K)| d\tau \leq 2M, \quad \text{for } t \in [0, T],$$

which implies $F' \in L^p([0, T])$ for $p \in [1, \infty)$. Furthermore, $F(0) = F(T) = 0$, together with the discussion above, implies $F \in W_0^{1,p}([0, T])$ for all $p \in [1, \infty)$ (Brezis, 2011, Theorem 8.12). Theorem 8.8 and the Remark 8 after Proposition 8.3 in Brezis (2011) imply $W_0^{1,p}([0, T]) \subseteq \mathcal{B}$ for $p \in [1, \infty)$. The proof of Lemma C.3 is complete. \square

L.5 Proof of Eq. (C.1)

This subsection gives the proof of the first half of Theorem C.3, i.e., Eq. (C.1). The following lemmas are prepared for the proof of Eq. (C.1).

Lemma L.2. *Suppose $K \in \mathcal{S}_{R,d}^M$. We have the following estimate for all t that are neither HCPs of K in direction ν_1 nor HCPs of K in direction ν_2 .*

$$\begin{aligned} \Upsilon_k(t; \nu_1, \nu_2) &\stackrel{\text{def}}{=} |\beta_k(K_t^{\nu_1}) - \beta_k(K_t^{\nu_2})| \\ &\leq \# \left\{ x \in \text{Dgm}_k(K; \phi_{\nu_1}) \mid x \neq \gamma^*(x) \text{ and } \underline{(x, \gamma^*(x))} \cap \partial((-\infty, t) \times (t, \infty)) \neq \emptyset \right\}, \end{aligned} \quad (\text{L.5})$$

where $\underline{(x, \gamma^*(x))}$ denotes the straight line segment connecting points x and $\gamma^*(x)$ in \mathbb{R}^2 , the map γ^* is any optimal bijection such that

$$W_\infty\left(\text{Dgm}_k(K; \phi_{\nu_1}), \text{Dgm}_k(K; \phi_{\nu_2})\right) = \sup \left\{ \|\xi - \gamma^*(\xi)\|_{l^\infty} \mid \xi \in \text{Dgm}_k(K; \phi_{\nu_1}) \right\} \quad (\text{L.6})$$

(see Definition B.1, and $\|\cdot\|_{l^\infty}$ is defined in Eq. (B.4)), and the cardinality $\#$ counts the corresponding multiplicity.

Remark L.1. *Because (\mathcal{D}, W_∞) is a geodesic space, the optimal bijection γ^* does exist (Turner, 2013, Proposition 1 and its proof).*

Proof of Lemma L.2. Since t is not an HCP, neither $\text{Dgm}_k(K; \phi_{\nu_1})$ nor $\text{Dgm}_k(K; \phi_{\nu_2})$ has a point on the boundary $\partial((-\infty, t) \times (t, \infty))$. If $\beta_k(K_t^{\nu_1}) = \beta_k(K_t^{\nu_2})$, Eq. (L.5) is true. Otherwise, without loss of generality, we assume $\beta_k(K_t^{\nu_1}) > \beta_k(K_t^{\nu_2})$. Notice

$$\beta_k(K_t^{\nu_i}) = \# \left\{ \text{Dgm}_k(K; \phi_{\nu_i}) \cap ((-\infty, t) \times (t, \infty)) \right\}, \quad \text{for } i \in \{1, 2\}.$$

Let γ^* be any optimal bijection, then there should be at least $\beta_k(K_t^{\nu_1}) - \beta_k(K_t^{\nu_2})$ straight line segments $\underline{(x, \gamma^*(x))}$ crossing $\partial((-\infty, t) \times (t, \infty))$; otherwise, γ^* is not bijective. Hence,

$$\begin{aligned} & \beta_k(K_t^{\nu_1}) - \beta_k(K_t^{\nu_2}) \\ & \leq \# \left\{ x \in \text{Dgm}_k(K; \phi_{\nu_1}) \mid x \neq \gamma^*(x) \text{ and } \underline{(x, \gamma^*(x))} \cap \partial((-\infty, t) \times (t, \infty)) \neq \emptyset \right\}, \end{aligned}$$

and Eq. (L.5) follows. \square

Lemma L.3. *Suppose $K \in \mathcal{S}_{R,d}^M$. Except for finitely many t , we have*

$$\Upsilon_k(t; \nu_1, \nu_2) \leq \frac{2M}{d} \cdot \mathbb{1}_{\mathcal{T}_k}, \quad \text{where}$$

$$\mathcal{T}_k \stackrel{\text{def}}{=} \left\{ t \in [0, T] \text{ not an HCP in direction } \nu_1 \text{ or } \nu_2 \mid \text{there exists } x \in \text{Dgm}_k(K; \phi_{\nu_1}) \text{ such that } x \neq \gamma^*(x) \right. \\ \left. \text{and } \underline{(x, \gamma^*(x))} \cap \partial((-\infty, t) \times (t, \infty)) \neq \emptyset \right\},$$

and $\gamma^* : \text{Dgm}_k(K; \phi_{\nu_1}) \rightarrow \text{Dgm}_k(K; \phi_{\nu_2})$ is any optimal bijection satisfying Eq. (L.6).

Proof of Lemma L.3. Eq. (L.3) implies

$$\Upsilon_k(t; \nu_1, \nu_2) = |\beta_k(K_t^{\nu_1}) - \beta_k(K_t^{\nu_2})| \leq 2M/d.$$

Furthermore, the inequality in Eq. (L.5) indicates that $\Upsilon_k(t; \nu_1, \nu_2) = 0$ if $t \notin \mathcal{T}_k$, except for finitely many HCPs in directions ν_1 and ν_2 . Then the desired estimate follows. \square

Proof of Eq. (C.1). Eq. (3.2) and Lemma L.3 imply the following for $p \in [1, \infty)$

$$\begin{aligned}
& \int_0^T \left| \left\{ \chi_\tau^{\nu_1}(K) - \chi_\tau^{\nu_2}(K) \right\} \right|^p d\tau \\
&= \int_0^T \left| \sum_{k=0}^{d-1} (-1)^k \cdot \left(\beta_k(K^{\nu_1}) - \beta_k(K^{\nu_2}) \right) \right|^p d\tau \\
&\leq \int_0^T \left(\sum_{k=0}^{d-1} \Upsilon_k(\tau; \nu_1, \nu_2) \right)^p d\tau \\
&\leq d^{(p-1)} \cdot \sum_{k=0}^{d-1} \int_0^T \left(\Upsilon_k(\tau; \nu_1, \nu_2) \right)^p d\tau \\
&\leq \frac{(2M)^p}{d} \cdot \sum_{k=0}^{d-1} \int_{\mathcal{T}_k} d\tau \\
&\leq \frac{(2M)^p}{d} \cdot \sum_{k=0}^{d-1} \left(\sum_{\xi \in \text{Dgm}_k(K; \phi_{\nu_1})} 2 \cdot \|\xi - \gamma^*(\xi)\|_{l^\infty} \right),
\end{aligned} \tag{L.7}$$

where the last inequality follows from the definition of \mathcal{T}_k . Since $\|\xi - \gamma^*(\xi)\|_{l^\infty}$ can be positive only if $\text{pers}(\xi) > 0$ or $\text{pers}(\gamma^*(\xi)) > 0$, there are at most N terms $\|\xi - \gamma^*(\xi)\|_{l^\infty} > 0$, where the condition in Eq. (3.4) implies

$$N \stackrel{\text{def}}{=} \sum_{i=1}^2 \#\{\xi \in \text{Dgm}_k(K; \phi_{\nu_i}) \mid \text{pers}(\xi) > 0\} \leq 2M/d.$$

Therefore, the inequality in Eq. (L.7) implies

$$\begin{aligned}
\int_0^T \left| \left\{ \chi_\tau^{\nu_1}(K) - \chi_\tau^{\nu_2}(K) \right\} \right|^p d\tau &\leq \frac{2 \cdot (2M)^{(p+1)}}{d} \cdot \sup \left\{ \|\xi - \gamma^*(\xi)\|_{l^\infty} \mid \xi \in \text{Dgm}_k(K; \phi_{\nu_1}) \right\} \\
&= \frac{2 \cdot (2M)^{(p+1)}}{d} \cdot W_\infty \left(\text{Dgm}_k(K; \phi_{\nu_1}), \text{Dgm}_k(K; \phi_{\nu_2}) \right).
\end{aligned}$$

Then, Theorem B.1 implies

$$\int_0^T \left| \left\{ \chi_\tau^{\nu_1}(K) - \chi_\tau^{\nu_2}(K) \right\} \right|^p d\tau \leq \frac{2 \cdot (2M)^{(p+1)}}{d} \cdot \sup_{x \in K} |x \cdot (\nu_1 - \nu_2)|.$$

Additionally, $|x \cdot (\nu_1 - \nu_2)| \leq \|x\| \cdot \|\nu_1 - \nu_2\|$ and $K \subseteq B(0, R)$ provide

$$\int_0^T \left| \left\{ \chi_\tau^{\nu_1}(K) - \chi_\tau^{\nu_2}(K) \right\} \right|^p d\tau \leq \frac{2 \cdot R \cdot (2M)^{(p+1)}}{d} \cdot \|\nu_1 - \nu_2\|. \tag{L.8}$$

Define the constant $C_{M,R,d}^*$ as follows

$$C_{M,R,d}^* \stackrel{\text{def}}{=} \sqrt{\frac{16M^3R}{d} + \frac{32M^3R}{d} + \frac{64M^4R}{d^2}}. \quad (\text{L.9})$$

(The constant $C_{M,R,d}^*$ defined in Eq. (L.9) will also be implemented in other proofs.)

Setting $p = 2$, Eq. (L.8) implies the following

$$\begin{aligned} \left(\int_0^T \left| \left\{ \chi_\tau^{\nu_1}(K) - \chi_\tau^{\nu_2}(K) \right\} \right|^2 d\tau \right)^{1/2} &\leq \sqrt{\frac{16M^3R}{d} \cdot \|\nu_1 - \nu_2\|} \\ &\leq C_{M,R,d}^* \cdot \sqrt{\|\nu_1 - \nu_2\|}, \end{aligned}$$

which is the inequality in Eq. (C.1). \square

L.6 Proof of Theorem 3.2

Proof of result (i), i.e., Eq. (3.5). The definition of $\text{SECT}(K)$, together with Eq. (L.8), implies

$$\begin{aligned} &\left\| \text{SECT}(K)(\nu_1) - \text{SECT}(K)(\nu_2) \right\|_{\mathcal{H}}^2 \\ &= \int_0^T \left| \frac{d}{dt} \text{SECT}(K)(\nu_1; t) - \frac{d}{dt} \text{SECT}(K)(\nu_2; t) \right|^2 dt \\ &= \int_0^T \left| \left(\chi_t^{\nu_1}(K) - \chi_t^{\nu_2}(K) \right) - \frac{1}{T} \int_0^T \left(\chi_\tau^{\nu_1}(K) - \chi_\tau^{\nu_2}(K) \right) d\tau \right|^2 dt \\ &\leq \int_0^T \left(\left| \chi_t^{\nu_1}(K) - \chi_t^{\nu_2}(K) \right| + \frac{1}{T} \int_0^T \left| \chi_\tau^{\nu_1}(K) - \chi_\tau^{\nu_2}(K) \right| d\tau \right)^2 dt \\ &\leq 2 \int_0^T \left| \chi_t^{\nu_1}(K) - \chi_t^{\nu_2}(K) \right|^2 dt + \frac{2}{T} \left(\int_0^T \left| \chi_\tau^{\nu_1}(K) - \chi_\tau^{\nu_2}(K) \right| d\tau \right)^2 \\ &\leq \frac{32M^3R}{d} \cdot \|\nu_1 - \nu_2\| + \frac{64M^4R}{d^2} \cdot \|\nu_1 - \nu_2\|^2, \end{aligned}$$

where the last inequality above comes from Eq. (L.8). Then, we have

$$\begin{aligned} &\left\| \text{SECT}(K)(\nu_1) - \text{SECT}(K)(\nu_2) \right\|_{\mathcal{H}} \\ &\leq \sqrt{\frac{32M^3R}{d} \cdot \|\nu_1 - \nu_2\| + \frac{64M^4R}{d^2} \cdot \|\nu_1 - \nu_2\|^2} \\ &\leq C_{M,R,d}^* \cdot \sqrt{\|\nu_1 - \nu_2\| + \|\nu_1 - \nu_2\|^2}, \end{aligned}$$

where $C_{M,R,d}^*$ is defined in Eq. (L.9). The proof of result (i), i.e., Eq. (3.5), is complete. \square

Proof of result (ii). The law of cosines and Taylor's expansion indicates

$$\begin{aligned} \frac{\|\nu_1 - \nu_2\|}{d_{\mathbb{S}^{d-1}}(\nu_1, \nu_2)} &= \sqrt{2 \cdot \frac{1 - \cos(d_{\mathbb{S}^{d-1}}(\nu_1, \nu_2))}{\{d_{\mathbb{S}^{d-1}}(\nu_1, \nu_2)\}^2}} \\ &= \sqrt{2 \cdot \left[\sum_{n=1}^{\infty} \frac{(-1)^{n+1}}{(2n)!} \cdot \{d_{\mathbb{S}^{d-1}}(\nu_1, \nu_2)\}^{2n-2} \right]} = O(1). \end{aligned}$$

Then, result (ii) comes from the following

$$\begin{aligned} &\frac{\|\text{SECT}(K)(\nu_1) - \text{SECT}(K)(\nu_2)\|_{\mathcal{H}}}{\sqrt{d_{\mathbb{S}^{d-1}}(\nu_1, \nu_2)}} \\ &\leq C_{M,R,d}^* \cdot \sqrt{\frac{\|\nu_1 - \nu_2\|}{d_{\mathbb{S}^{d-1}}(\nu_1, \nu_2)} + \frac{\|\nu_1 - \nu_2\|^2}{d_{\mathbb{S}^{d-1}}(\nu_1, \nu_2)}} = O(1). \end{aligned} \tag{L.10}$$

The proof of Theorem 3.2 is complete. \square

L.7 Proof of Lemma C.2

Proof of Lemma C.2. Theorem C.2, Lemma L.1, and the definition of $\|\cdot\|_{\mathcal{H}}$ imply the following

$$\begin{aligned} \|\text{SECT}(K)\|_{C(\mathbb{S}^{d-1}, \mathcal{H})} &= \sup_{\nu \in \mathbb{S}^{d-1}} \{\|\text{SECT}(K)(\nu)\|_{\mathcal{H}}\} \\ &= \sup_{\nu \in \mathbb{S}^{d-1}} \left(\int_0^T \left| \chi_t^\nu(K) - \frac{1}{T} \int_0^T \chi_\tau^\nu(K) d\tau \right|^2 dt \right)^{1/2} \\ &\leq 2M \cdot \sqrt{T}. \end{aligned}$$

The proof of Lemma C.2 is complete. \square

L.8 Proof of Eq. (C.2)

This subsection gives the proof of the second half of Theorem C.3, i.e., Eq. (C.2).

Proof of Eq. (C.2). We consider the following inequality for all $\nu_1, \nu_2 \in \mathbb{S}^{d-1}$ and $t_1, t_2 \in [0, T]$

$$\begin{aligned}
& |\text{SECT}(K)(\nu_1; t_1) - \text{SECT}(K)(\nu_2; t_2)| \\
& \leq |\text{SECT}(K)(\nu_1; t_1) - \text{SECT}(K)(\nu_1; t_2)| \\
& \quad + |\text{SECT}(K)(\nu_1; t_2) - \text{SECT}(K)(\nu_2; t_2)| \\
& \stackrel{\text{def}}{=} I + II.
\end{aligned} \tag{L.11}$$

From the definition of $\|\cdot\|_{C^{0, \frac{1}{2}}([0, T])}$ and Eq. (2.1), we have

$$\begin{aligned}
& \sup_{t_1, t_2 \in [0, T], t_1 \neq t_2} \frac{|\text{SECT}(K)(\nu_1; t_1) - \text{SECT}(K)(\nu_1; t_2)|}{|t_1 - t_2|^{1/2}} \\
& \leq \|\text{SECT}(K)(\nu_1)\|_{C^{0, \frac{1}{2}}([0, T])} \\
& \leq \tilde{C}_T \|\text{SECT}(K)(\nu_1)\|_{\mathcal{H}} \\
& \leq \tilde{C}_T \|\text{SECT}(K)\|_{C(\mathbb{S}^{d-1}; \mathcal{H})},
\end{aligned}$$

which implies the following for all $t_1, t_2 \in [0, T]$

$$\begin{aligned}
I & \leq \tilde{C}_T \|\text{SECT}(K)\|_{C(\mathbb{S}^{d-1}; \mathcal{H})} \cdot |t_1 - t_2|^{1/2} \\
& \leq \tilde{C}_T \cdot 2M\sqrt{T} \cdot \sqrt{|t_1 - t_2|},
\end{aligned}$$

where the second inequality follows from Lemma C.2.

Applying Eq. (2.1) again, we have

$$\begin{aligned}
II & \leq \|\text{SECT}(K)(\nu_1) - \text{SECT}(K)(\nu_2)\|_{\mathcal{B}} \\
& \leq \tilde{C}_T \|\text{SECT}(K)(\nu_1) - \text{SECT}(K)(\nu_2)\|_{\mathcal{H}} \\
& \leq \tilde{C}_T \cdot C_{M, R, d}^* \cdot \sqrt{\|\nu_1 - \nu_2\| + \|\nu_1 - \nu_2\|^2},
\end{aligned}$$

where the last inequality follows from Theorem 3.2(i). Then, the inequality in Eq. (C.2) follows from Eq. (L.11). \square

L.9 Proof of Theorem 3.3

Recall the following concepts discussed in Appendix C:

- For any given o-minimal structure \mathcal{S} , any elements of \mathcal{S} are called definable sets.
- Compact definable sets are called constructible sets. The collection of constructible subsets of \mathbb{R}^d is denoted by $\text{CS}(\mathbb{R}^d)$.
- If \mathcal{S} satisfies Assumption 1, we have $\mathcal{S}_{R,d}^M \subseteq \text{CS}(\mathbb{R}^d)$.

Then, Theorem 3.3 follows directly from Corollary C.1 (i.e., Corollary 1 of Ghrist et al. (2018)).

We have the following as a further explanation for Corollary C.1: Using a Morse theory-like result, Ji et al. (2023) showed that the ECT and SECT determine each other; then, the injectivity of the ECT stated in Theorem C.4 (i.e., Theorem 1 of Ghrist et al. (2018) or Theorem 3.5 of Curry et al. (2022)) implies the injectivity of the SECT.

L.10 Proof of Theorem 4.1

Proof of Theorem 4.1. The proof needs the concept of PECT defined in Eq. (C.3).

The compactness of K , together with $K \subseteq B(0, R)$, implies that $\chi(K_t^\nu) = 0$ for all t satisfying the following

$$0 \leq t < \text{dist}(K, \partial B(0, R)) = \inf \left\{ \|x - y\| \mid x \in K \text{ and } y \in \partial B(0, R) \right\} \stackrel{\text{def}}{=} \sigma > 0.$$

Therefore, $\text{PECT}(K)(\nu, t) = \int_0^t \chi_\tau^\nu(K) d\tau = 0$ for all $0 \leq t < \sigma$, which implies

$$\left. \frac{d^+}{dt} \right|_{t=0} \text{SECT}(K)(\nu, t) = -\frac{1}{T} \text{PECT}(K)(\nu, T),$$

where $\frac{d^+}{dt}$ denotes the right derivative with respect to t . Hence, we have

$$\text{PECT}(K)(\nu, t) = \text{SECT}(K)(\nu, t) - t \cdot \left. \frac{d^+}{dt} \right|_{t=0} \text{SECT}(K)(\nu, t).$$

That is, $\text{PECT}(K)$ and $\text{SECT}(K)$ determine each other. Then, Theorem 3.3 implies that the PECT defined in Eq. (C.3) is injective. (Alternatively, Lemma L.1, together with Lemma C.1 and Theorem C.4, also implies that the PECT in Eq. (C.3) is injective.)

The triangle inequalities and symmetry of ρ follow from that of the metric of $C(\mathbb{S}^{d-1}; \mathcal{H})$. Equation $\rho(K_1, K_2) = 0$ indicates $\|\text{PECT}(K_1)(\nu) - \text{PECT}(K_2)(\nu)\|_{\mathcal{H}_{BM}} = 0$ for all $\nu \in \mathbb{S}^{d-1}$. Evans (2010) (Theorem 5 of Chapter 5.6) implies $\|\text{PECT}(K_1)(\nu) - \text{PECT}(K_2)(\nu)\|_{\mathcal{B}} = 0$ for all $\nu \in \mathbb{S}^{d-1}$. Then, we have $\int_0^t \chi_\tau^\nu(K_1) d\tau = \int_0^t \chi_\tau^\nu(K_2) d\tau$ for all $t \in [0, T]$ and $\nu \in \mathbb{S}^{d-1}$; hence, $\text{SECT}(K_1) = \text{SECT}(K_2)$. Then, Theorem 3.3 implies $K_1 = K_2$. Therefore, ρ is a distance.

The proof of that $\mathcal{F} = \mathcal{B}(\rho)$ satisfies Assumption 2 is motivated by the following chain of maps for any fixed $\nu \in \mathbb{S}^{d-1}$ and $t \in [0, T]$.

$$\begin{aligned} \mathcal{S}_{R,d}^M &\xrightarrow{\text{PECT}} C(\mathbb{S}^{d-1}; \mathcal{H}_{BM}) \xrightarrow{\text{projection}} \mathcal{H}_{BM}, \text{ which is embedded into } \mathcal{B} \xrightarrow{\text{projection}} \mathbb{R}, \\ K &\mapsto \{\text{PECT}(K)(\nu')\}_{\nu' \in \mathbb{S}^{d-1}} \mapsto \{\text{PECT}(K)(\nu, t')\}_{t' \in [0, T]} \mapsto \text{PECT}(K)(\nu, t) = \int_0^t \chi_\tau^\nu(K) d\tau, \end{aligned}$$

where all spaces above are metric spaces and equipped with their Borel algebras. We notice the following facts:

- the mapping $\text{PECT} : \mathcal{S}_{R,d}^M \rightarrow C(\mathbb{S}^{d-1}; \mathcal{H}_{BM})$ is isometric;
- the projection $C(\mathbb{S}^{d-1}; \mathcal{H}_{BM}) \rightarrow \mathcal{H}_{BM}$, $\{F(\nu')\}_{\nu' \in \mathbb{S}^{d-1}} \mapsto F(\nu)$ is continuous for each fixed direction ν ;
- applying Evans (2010) (Theorem 5 of Chapter 5.6) again, the embedding $\mathcal{H}_{BM} \rightarrow \mathcal{B}$, $F(\nu) \mapsto F(\nu)$ is continuous;
- projection $\mathcal{B} \rightarrow \mathbb{R}$, $\{x(t')\}_{t' \in [0, T]} \mapsto x(t)$ is continuous.

Therefore, $\mathcal{S}_{R,d}^M \rightarrow \mathbb{R}$, $K \mapsto \text{PECT}(K)(\nu, t)$ is continuous, hence, measurable.

For any $K \in \mathcal{S}_{R,d}^M$, Lemmas 3.1 and C.1 imply the following for all t and ν

$$\chi_t^\nu(K) = \lim_{n \rightarrow \infty} \left[\frac{1}{\delta_n} \{ \text{PECT}(K)(\nu, t + \delta_n) - \text{PECT}(K)(\nu, t) \} \right],$$

where $\lim_{n \rightarrow \infty} \delta_n = 0$ and $\delta_n > 0$. The measurability of $\text{PECT}(\nu, t + \delta_n)$ and $\text{PECT}(\nu, t)$ implies that $\chi_t^\nu : \mathcal{S}_{R,d}^M \rightarrow \mathbb{R}, K \mapsto \chi_t^\nu(K)$ is measurable, for any fixed ν and t .

The proof of Theorem 4.1 is complete. \square

L.11 Proof of Lemma 4.1

Proof of Lemma 4.1. Lemma C.2 implies the following for all $K \in \mathcal{S}_{R,d}^M$

$$\sup_{\nu \in \mathbb{S}^{d-1}} \|\text{SECT}(K)(\nu)\|_{\mathcal{H}}^2 \leq 4M^2T.$$

Then, we have

$$\int_{\mathcal{S}_{R,d}^M} \left\{ \sup_{\nu \in \mathbb{S}^{d-1}} \|\text{SECT}(K)(\nu)\|_{\mathcal{H}}^2 \right\} \mathbb{P}(dK) \leq 4M^2T < \infty.$$

The proof of Lemma 4.1 is complete. \square

L.12 Proof of Lemma C.4

The proof of Lemma C.4 is divided into five small proofs.

Proof of result (i). For each fixed direction $\nu \in \mathbb{S}^{d-1}$, Theorem 4.2 indicates that the mapping $\text{SECT}(\nu) : K \mapsto \text{SECT}(K)(\nu)$ is an \mathcal{H} -valued measurable function defined on the probability space $(\mathcal{S}_{R,d}^M, \mathcal{F}, \mathbb{P})$. We first show the Bochner \mathbb{P} -integrability of $\text{SECT}(\nu)$ (see Section 5 in Chapter V of Yosida (2012) for the definition of Bochner \mathbb{P} -integrability), and the Bochner integral of $\text{SECT}(\nu)$ will be fundamental to our proof. Lemma 1.3 of Da Prato and Zabczyk (2014) indicates that $\text{SECT}(\nu)$ is strongly \mathcal{F} -measurable (see Section 4 in

Chapter V of [Yosida \(2012\)](#) for the definition of strong \mathcal{F} -measurability). Then, Lemma 4.1 indicates that the Bochner integral

$$m_\nu^* \stackrel{\text{def}}{=} \int_{\mathcal{S}_{R,d}^M} \text{SECT}(K)(\nu) \mathbb{P}(dK)$$

is Bochner \mathbb{P} -integrable and $m_\nu^* \in \mathcal{H}$ ([Yosida, 2012](#), Section 5 of Chapter V, Theorem 1).

The Corollary 2 in Section 5 of Chapter V of [Yosida \(2012\)](#), together with that \mathcal{H} is the RKHS generated by the kernel $\kappa(s, t) = \min\{s, t\} - \frac{st}{T}$ ([Lifshits, 2012](#), Example 4.9), implies

$$\begin{aligned} m_\nu^*(t) &= \langle \kappa(t, \cdot), m_\nu^* \rangle \\ &= \int_{\mathcal{S}_{R,d}^M} \left\langle \kappa(t, \cdot), \text{SECT}(K)(\nu) \right\rangle \mathbb{P}(dK) \\ &= \int_{\mathcal{S}_{R,d}^M} \text{SECT}(K)(\nu, t) \mathbb{P}(dK) \\ &= \mathbb{E} \{ \text{SECT}(\nu, t) \} = m_\nu(t), \quad \text{for all } t \in [0, T], \end{aligned}$$

where $\langle \cdot, \cdot \rangle$ denotes the inner product of \mathcal{H} . Therefore, $m_\nu = m_\nu^* \in \mathcal{H}$. The proof of result (i) is complete. \square

Proof of result (ii). To prove result (ii), we first show the product measurability of the following map for each fixed direction $\nu \in \mathbb{S}^{d-1}$

$$\begin{aligned} (\mathcal{S}_{R,d}^M \times [0, T], \mathcal{F} \otimes \mathcal{B}([0, T])) &\rightarrow (\mathbb{R}, \mathcal{B}(\mathbb{R})), \\ (K, t) &\mapsto \text{SECT}(K)(\nu, t), \end{aligned} \tag{L.12}$$

where $\mathcal{F} \otimes \mathcal{B}([0, T])$ denotes the product σ -algebra generated by \mathcal{F} and $\mathcal{B}([0, T])$. Define the filtration $\{\mathcal{F}_t\}_{t \in [0, T]}$ by $\mathcal{F}_t \stackrel{\text{def}}{=} \sigma(\{\text{SECT}(\nu, t') \mid t' \in [0, t]\}) \subseteq \mathcal{F}$ for $t \in [0, T]$. Because the sample paths of $\text{SECT}(\nu)$ are in \mathcal{H} , these sample paths are continuous (see the Sobolev embedding in Eq. (2.2)). Proposition 1.13 of [Karatzas and Shreve \(2012\)](#) implies that the stochastic process $\text{SECT}(\nu)$ is progressively measurable with respect to the filtration $\{\mathcal{F}_t\}_{t \in [0, T]}$. Then, the mapping in Eq. (L.12) is measurable with respect to the product

σ -algebra $\mathcal{F} \otimes \mathcal{B}([0, T])$ (Karatzas and Shreve, 2012, Definitions 1.6 and 1.11, also the paragraph right after Definition 1.11 therein). Lemma 4.1 implies

$$\int_0^T \int_{\mathcal{S}_{R,d}^M} |\text{SECT}(K)(\nu, t)|^2 \mathbb{P}(dK) dt \leq T \cdot \tilde{C}_T^2 \cdot \mathbb{E} \|\text{SECT}(\nu)\|_{\mathcal{H}}^2 < \infty,$$

where the double integral is well-defined because of the product measurability of the mapping in Eq. (L.12) and the Fubini's theorem. Then, the proof of result (ii) is complete. \square

Proof of result (iii). Eq. (C.2) implies

$$\mathbb{E} |\text{SECT}(\nu, t + \epsilon) - \text{SECT}(\nu, t)|^2 \leq \tilde{C}_T^2 \cdot 4M^2T \cdot |\epsilon| \rightarrow 0,$$

as $\epsilon \rightarrow 0$. The proof is complete. \square

Proof of result (iv). Result (iv) follows from Lemma 4.2 of Alexanderian (2015). \square

Proof of result (v). For any $\nu_1, \nu_2 \in \mathbb{S}^{d-1}$, the proof of result (i) implies the following Bochner integral representation

$$\begin{aligned} \|m_{\nu_1} - m_{\nu_2}\|_{\mathcal{H}} &= \left\| \int_{\mathcal{S}_{R,d}^M} \text{SECT}(K)(\nu_1) - \text{SECT}(K)(\nu_2) \mathbb{P}(dK) \right\|_{\mathcal{H}} \\ &\stackrel{(1)}{\leq} \int_{\mathcal{S}_{R,d}^M} \left\| \text{SECT}(K)(\nu_1) - \text{SECT}(K)(\nu_2) \right\|_{\mathcal{H}} \mathbb{P}(dK) \\ &\stackrel{(2)}{\leq} C_{M,R,d}^* \cdot \sqrt{\|\nu_1 - \nu_2\| + \|\nu_1 - \nu_2\|^2}, \end{aligned}$$

where the inequality (1) follows from the Corollary 1 in Section 5 of Chapter V of Yosida (2012), and the inequality (2) follows from Eq. (3.5). With the argument in Eq. (L.10), the proof of result (v) is complete. \square

L.13 Proof of Theorem 5.1

Proof of Theorem 5.1. Lemma C.4 implies that, for each $j \in \{1, 2\}$, the stochastic process $\{\text{SECT}(\nu^*; t) - m_{\nu^*}^{(j)}(t)\}_{t \in [0, T]}$ is of mean zero, mean-square continuous, and belongs to

$L^2(\mathcal{S}_{R,d}^M \times [0, T], \mathbb{P}^{(j)}(dK) \otimes dt)$. Then, result (i) follows from Theorem 7.3.5 of [Hsing and Eubank \(2015\)](#) (equivalently, Corollary 5.5 of [Alexanderian \(2015\)](#)).

To prove result (ii), we denote the following

$$\begin{aligned} & D_L(K^{(1)}, K^{(2)}; t) \\ & \stackrel{\text{def}}{=} \{ \text{SECT}(K^{(1)})(\nu^*; t) - \text{SECT}(K^{(2)})(\nu^*; t) \} \\ & - \left[\left\{ m_{\nu^*}^{(1)}(t) + \sum_{\nu'=1}^L \sqrt{\lambda_{\nu'}} \cdot Z_{\nu'}^{(1)}(K^{(1)}) \cdot \phi_{\nu'}(t) \right\} - \left\{ m_{\nu^*}^{(2)}(t) + \sum_{\nu'=1}^L \sqrt{\lambda_{\nu'}} \cdot Z_{\nu'}^{(2)}(K^{(2)}) \cdot \phi_{\nu'}(t) \right\} \right] \end{aligned}$$

Then, result (i) implies the following

$$\begin{aligned} & \lim_{L \rightarrow \infty} \left\{ \sup_{t \in [0, T]} \|D_L(\cdot, \cdot; t)\|_{L^2}^2 \right\} \\ & = \lim_{L \rightarrow \infty} \left\{ \sup_{t \in [0, T]} \int_{\mathcal{S}_{R,d}^M \times \mathcal{S}_{R,d}^M} |D(K^{(1)}, K^{(2)}; t)|^2 \mathbb{P}^{(1)} \otimes \mathbb{P}^{(2)}(dK^{(1)}, dK^{(2)}) \right\} = 0, \end{aligned}$$

where L^2 is the abbreviation for $L^2(\mathcal{S}_{R,d}^M \times \mathcal{S}_{R,d}^M, \mathcal{F} \otimes \mathcal{F}, \mathbb{P}^{(1)} \otimes \mathbb{P}^{(2)})$. For each fixed $l = 1, 2, \dots$, we have

$$\begin{aligned} & \left\| \frac{1}{\sqrt{2\lambda_l}} \int_0^T D_L(\cdot, \cdot; t) \phi_l(t) dt \right\|_{L^2} \\ & \leq \frac{1}{\sqrt{2\lambda_l}} \int_0^T \|D_L(\cdot, \cdot; t)\|_{L^2} |\phi_l(t)| dt \\ & \leq \sup_{t \in [0, T]} \|D_L(\cdot, \cdot; t)\|_{L^2} \cdot \frac{1}{\sqrt{2\lambda_l}} \int_0^T |\phi_l(\tau)| d\tau \rightarrow 0, \quad \text{as } L \rightarrow \infty. \end{aligned} \tag{L.13}$$

In addition, for each fixed $l = 1, 2, \dots$ and $L > l$, we have

$$\begin{aligned} & \frac{1}{\sqrt{2\lambda_l}} \int_0^T D_L(K^{(1)}, K^{(2)}; t) \phi_l(t) dt \\ & = \frac{1}{\sqrt{2\lambda_l}} \int_0^T \{ \text{SECT}(K^{(1)})(\nu^*; t) - \text{SECT}(K^{(2)})(\nu^*; t) \} \phi_l(t) dt \\ & - \frac{1}{\sqrt{2\lambda_l}} \int_0^T \{ m_{\nu^*}^{(1)}(t) - m_{\nu^*}^{(2)}(t) \} \phi_l(t) dt \\ & - \frac{1}{\sqrt{2\lambda_l}} \int_0^T \left[\sum_{\nu'=1}^L \sqrt{\lambda_{\nu'}} \cdot \{ Z_{\nu'}^{(1)}(K^{(1)}) - Z_{\nu'}^{(2)}(K^{(2)}) \} \cdot \phi_{\nu'}(t) \right] \cdot \phi_l(t) dt \\ & = \delta_l(K^{(1)}, K^{(2)}) - \left[\theta_l + \left(\frac{Z_l^{(1)}(K^{(1)}) - Z_l^{(2)}(K^{(2)})}{\sqrt{2}} \right) \right], \end{aligned}$$

where $\delta_l(K^{(1)}, K^{(2)})$ is defined in Eq. (5.5), and the last equality follows from the $L^2([0, T])$ -orthonormality of $\{\phi_l\}_{l=1}^\infty$. The limit in Eq. (L.13) imply

$$\begin{aligned} & \int_{\mathcal{S}_{R,d}^M \times \mathcal{S}_{R,d}^M} \left| \delta_l(K^{(1)}, K^{(2)}) - \left[\theta_l + \left(\frac{Z_l^{(1)}(K^{(1)}) - Z_l^{(2)}(K^{(2)})}{\sqrt{2}} \right) \right] \right|^2 \mathbb{P}^{(1)} \otimes \mathbb{P}^{(2)}(dK^{(1)}, dK^{(2)}) \\ &= \lim_{L \rightarrow \infty} \left\| \frac{1}{\sqrt{2\lambda_l}} \int_0^T D_L(\cdot, \cdot; t) \phi_l(t) dt \right\|_{L^2} \\ &= 0. \end{aligned}$$

Then, there exists $\mathcal{N}_l \in \mathcal{F} \otimes \mathcal{F}$, which depends on l , such that $\mathbb{P}^{(1)} \otimes \mathbb{P}^{(2)}(\mathcal{N}_l) = 0$ and

$$\delta_l(K^{(1)}, K^{(2)}) = \theta_l + \left(\frac{Z_l^{(1)}(K^{(1)}) - Z_l^{(2)}(K^{(2)})}{\sqrt{2}} \right), \quad (\text{L.14})$$

for any $(K^{(1)}, K^{(2)}) \notin \mathcal{N}_l$. Define $\mathcal{N} \stackrel{\text{def}}{=} \bigcup_{l=1}^\infty \mathcal{N}_l$, we have $\mathbb{P}^{(1)} \otimes \mathbb{P}^{(2)}(\mathcal{N}) = 0$ and Eq. (L.14) holds for all $(K^{(1)}, K^{(2)}) \notin \mathcal{N}$ and $l = 1, 2, \dots$. The proof of result (ii) is complete. \square

L.14 Proof of Lemma 5.1

Proof of Lemma 5.1. We have shown that the null H_0 is equivalent to $m_{\nu^*}^{(1)}(t) = m_{\nu^*}^{(2)}(t)$ for all $t \in [0, T]$, where ν^* is defined in Eq. (5.3). The null H_0 directly implies that $\theta_l = 0$ for all l . On the other hand, if $\theta_l = 0$ for all l , that $\{\phi_l\}_l$ is an orthonormal basis of $L^2([0, T])$ indicates that $m_{\nu^*}^{(1)} = m_{\nu^*}^{(2)}$ almost everywhere with respect to the Lebesgue measure dt . Part (i) of Lemma C.4 and the embedding $\mathcal{H} \subseteq \mathcal{B}$ in Eq. (2.2) imply that $m_{\nu^*}^{(1)}$ and $m_{\nu^*}^{(2)}$ are continuous functions. As a result, $m_{\nu^*}^{(1)}(t) = m_{\nu^*}^{(2)}(t)$ for all $t \in [0, T]$. The proof is complete. \square

L.15 Proof of Theorem C.5

Proof of Theorem C.5. The independence condition implies that the stochastic process $\text{PECT}(\nu) = \{\text{PECT}(\nu, t) = \int_0^t \chi_\tau^\nu d\tau\}_{t \in [0, T]}$ has independent increments. The continuity

of the sample paths of $\text{PECT}(\nu)$ and that $\text{PECT}(\nu, 0) = \int_0^0 \chi_\tau^\nu d\tau = 0$ imply $\text{PECT}(\nu)$ is a Gaussian process (Kallenberg, 2021, Theorem 14.4). \square

M Potential Future Research Areas

In this section, we list several potential future research areas that we believe are related to our work.

M.1 Generative Models for Complex Shapes

Theorem 5.1 also holds for any fixed direction ν ; that is, the distinguishing direction ν^* in Theorem 5.1 can be replaced with any fixed $\nu \in \mathbb{S}^{d-1}$ (see the corresponding proof in Appendix L.13). The first result of Theorem 5.1 can be formally represented as follows

$$\text{SECT}(K)(\nu, t) = m_\nu^{(j)}(t) + \sum_{l=1}^{\infty} \sqrt{\lambda_l} \cdot Z_l^{(j)}(K) \cdot \phi_l(t). \quad (\text{M.1})$$

Using Eq. (M.1), the random sampling of shapes may be considered. This involves sampling the stochastic process on the right-hand side of Eq. (M.1) and reconstructing a shape by applying the inverse of the injective map $\text{SECT} : \mathcal{S}_{R,d}^M \rightarrow C(\mathbb{S}^{d-1}; \mathcal{H})$. Still, several challenges arise:

- i) the map SECT is not surjective, and the characterization of the image $\text{SECT}(\mathcal{S}_{R,d}^M)$ remains to be developed;
- ii) one must properly select the covariance function Ξ_ν and the distribution of $\{Z_l^{(j)}\}_{l=1}^{\infty}$ to ensure that the sample paths of $m_\nu^{(j)}(t) + \sum_{l=1}^{\infty} \sqrt{\lambda_l} \cdot Z_l^{(j)} \cdot \phi_l(t)$ belong to $\text{SECT}(\mathcal{S}_{R,d}^M)$;
- iii) reconstructing shapes K from $\text{SECT}(K)$, as discussed in Fasy et al. (2018), is still an open question in the field. The random sampling of shapes using Eq. (M.1) is left for future research.

M.2 Definition of Mean Shapes

The existence and uniqueness of the mean shapes K_{\oplus} in the Fréchet sense as defined in Eq. (D.3) are still unknown. If mean shapes K_{\oplus} do exist, the relationship between $\text{SECT}(K_{\oplus})$ and $\mathbb{E}\{\text{SECT}\}$ is of particular interest. In addition, the relationship of $\mathbb{E}\{\text{SECT}\}$ to the theory for “expectations of random sets” (Molchanov, 2005) is of interest and left for future research.

The Fréchet mean in Eq. (D.3) may be extended to the conditional Fréchet mean and implemented in the Fréchet regression — predicting shapes K using multiple scalar predictors (Petersen and Müller, 2019). For example, predicting molecular shapes and structures from scalar-valued indicators or sequences has become of high interest in biology (Jumper et al., 2021; Yang et al., 2020). As an example of the other way around, predicting clinical outcomes from the tumors is also of interest (Moon et al., 2020; Somasundaram et al., 2021; Vipond et al., 2021), which is potentially relevant to the Wasserstein regression (Chen et al., 2023).

M.3 Two-sample Test via the Reproducing Kernel Hilbert Space embedding or Optimal Transport

From the viewpoint of statistical inference, the ultimate goal of this paper is to solve the following two-sample test problem (also see Eq. (5.1)):

$$H_0^* : \mathbb{P}^{(1)} = \mathbb{P}^{(2)}, \quad \text{vs.} \quad H_1^* : \mathbb{P}^{(1)} \neq \mathbb{P}^{(2)}, \quad (\text{M.2})$$

where the observed shapes $\{K_i^{(j)}\}_{i=1}^n \stackrel{\text{i.i.d.}}{\sim} \mathbb{P}^{(j)}$, for $j \in \{1, 2\}$. Through the distinguishing direction ν^* defined in Eq. (5.3), the two-sample test problem in Eq. (M.2) can be

transformed into testing the equality of probability measures defined on the RKHS \mathcal{H} , i.e.,

$$H_0 : \mathbf{P}^{(1)} = \mathbf{P}^{(2)}, \text{ vs. } \mathbf{P}^{(1)} \neq \mathbf{P}^{(2)}, \quad (\text{M.3})$$

where $\mathbf{P}^{(j)}(B) \stackrel{\text{def}}{=} \mathbb{P}^{(j)} \{K \in \mathcal{S}_{R,d}^M \mid \text{SECT}(K)(\nu^*) \in B\}$ for all $B \in \mathcal{B}(\mathcal{H})$ and $j \in \{1, 2\}$.

In the literature, numerous powerful frameworks for two-sample test problems have been developed in the past decade. One notable framework is the “kernel two-sample test” (Gretton et al., 2006, 2012; Hagrass et al., 2023), which is based on the concept of “RKHS embedding of probability measures” (Smola et al., 2007; Fukumizu et al., 2009; Sriperumbudur et al., 2010, 2011; Muandet et al., 2017). Another framework is the rank-based distribution-free test framework proposed by Deb and Sen (2023), rooted in the theory of optimal transport (Villani et al., 2009).

With appropriate adjustments, it is possible to adapt the existing two-sample test frameworks from the literature to address the specific two-sample test problems outlined in Eq. (M.2) and Eq. (M.3). The exploration of this avenue is left for our future research.

M.4 Euler Characteristic-based Statistical Inference on Grayscale Images: Theory and Applications

Each shape K can be viewed as a binary-valued image, e.g., the points inside K are assigned to be 1 while the points outside K are assigned to be 0. That is, the shape can be equivalently represented as the indicator function $\mathbb{1}_K$ of the shape K . Many images in applications are real-valued instead of binary-valued, e.g., the computed tomography (CT) scans of lung cancer tumors (Maldonado et al., 2021). The real-valued images are referred to as grayscale images.

Over the past several years, some Euler characteristic-based representations of grayscale images have been proposed. Jiang et al. (2020) proposed the weighted Euler curve transform

(WECT) for the analysis of MNIST digit images (LeCun et al., 1998) and GBM tumor data (Holland, 2000). Kirveslahti and Mukherjee (2023) introduced three representations: the lifted ECT (LECT), super LECT (SELECT), and marginal Euler curve (MEC) for grayscale images. Kirveslahti and Mukherjee (2023) also demonstrated that the MEC coincides with the WECT on weighted simplicial complexes. Meng et al. (2023) introduced the Euler-Radon transform (ERT) for modeling grayscale images using Euler integration over real-valued functions (Baryshnikov and Ghrist, 2010). Notably, they found that the MEC coincides with the “floor version” of the ERT. However, one key question remains unresolved in this series of frameworks: a probability space has yet to be constructed to mathematically characterize the randomness of the grayscale images of interest, which is left for future research.

M.5 Euler Characteristic-based Topological Data Analysis

Euler characteristic-based descriptors, especially the ECT, have been pivotal for TDA due to the following:

- i) Euler calculus (Schapira, 1988; Viro, 1988; Schapira, 1991, 1995; van den Dries, 1998; Baryshnikov and Ghrist, 2010; Ghrist, 2014) provides rich mathematical machinery for the Euler characteristic-based descriptors in TDA. For example, Ghrist et al. (2018) and Curry et al. (2022) applied Schapira’s inversion formula (Schapira, 1995) to show the injectivity of the ECT.
- ii) Compared to persistence diagram-based descriptors, computing Euler characteristic-based descriptors is more efficient (Milosavljević et al., 2011; Hacquard and Lebovici, 2023; Munch, 2023).
- iii) As illustrated in this paper, Euler characteristic-based descriptors may allow the

implementation of functional analysis tools for mathematical purposes and the implementation of functional data analysis for statistical purposes.

Munch (2023) provided a comprehensive overview of the ECT from both theoretical and applied perspectives. In addition, persistent homology-based descriptors have been applied to brain networks for more than a decade (Lee et al., 2011; Wang et al., 2023; Li et al., 2023). We may also consider applying Euler characteristic-based descriptors to weighted graphs, particularly focusing on their applications to brain connectivity (Friston et al., 1993; Lee et al., 2011; Li et al., 2023; Chen et al., 2024; Meng and Eloyan, 2024). There is still much room for the future development of Euler characteristic-based descriptors.

References

- R. Al-Aifari, I. Daubechies, and Y. Lipman. Continuous procrustes distance between two surfaces. *Communications on Pure and Applied Mathematics*, 66(6):934–964, 2013. doi: <https://doi.org/10.1002/cpa.21444>. URL <https://onlinelibrary.wiley.com/doi/abs/10.1002/cpa.21444>.
- A. Alexanderian. A brief note on the karhunen–loève expansion. *arXiv preprint arXiv:1509.07526*, 2015.
- Y. Baryshnikov and R. Ghrist. Euler integration over definable functions. *Proceedings of the National Academy of Sciences*, 107(21):9525–9530, 2010. doi: 10.1073/pnas.0910927107. URL <https://www.pnas.org/doi/abs/10.1073/pnas.0910927107>.
- D. M. Boyer, Y. Lipman, E. S. Clair, J. Puente, B. A. Patel, T. Funkhouser, J. Jernvall, and I. Daubechies. Algorithms to automatically quantify the geometric similarity of

- anatomical surfaces. *Proceedings of the National Academy of Sciences*, 108(45):18221–18226, 2011. doi: 10.1073/pnas.1112822108. URL <https://www.pnas.org/doi/abs/10.1073/pnas.1112822108>.
- H. Brezis. *Functional analysis, Sobolev spaces and partial differential equations*, volume 2. Springer, 2011.
- E. Brunner, H. Dette, and A. Munk. Box-type approximations in nonparametric factorial designs. *Journal of the American Statistical Association*, 92(440):1494–1502, 1997.
- Y. Chen, Z. Lin, and H.-G. Müller. Wasserstein regression. *Journal of the American Statistical Association*, 118(542):869–882, 2023.
- Y. Chen, S.-C. Lin, Y. Zhou, O. Carmichael, H.-G. Müller, and A. D. N. I. Wang, Jane-Ling. Gradient synchronization for multivariate functional data, with application to brain connectivity. *Journal of the Royal Statistical Society Series B: Statistical Methodology*, page qkad140, 01 2024. ISSN 1369-7412. doi: 10.1093/jrsssb/qkad140. URL <https://doi.org/10.1093/jrsssb/qkad140>.
- D. Cohen-Steiner, H. Edelsbrunner, and J. Harer. Stability of persistence diagrams. *Discrete & computational geometry*, 37(1):103–120, 2007.
- L. Crawford, A. Monod, A. X. Chen, S. Mukherjee, and R. Rabadán. Predicting clinical outcomes in glioblastoma: an application of topological and functional data analysis. *Journal of the American Statistical Association*, 115(531):1139–1150, 2020.
- J. Cuesta-Albertos and M. Febrero-Bande. A simple multiway anova for functional data. *Test*, 19(3):537–557, 2010.

- A. Cuevas, M. Febrero, and R. Fraiman. An anova test for functional data. *Computational statistics & data analysis*, 47(1):111–122, 2004.
- J. Curry, S. Mukherjee, and K. Turner. How many directions determine a shape and other sufficiency results for two topological transforms. *Transactions of the American Mathematical Society, Series B*, 9(32):1006–1043, 2022.
- G. Da Prato and J. Zabczyk. *Stochastic equations in infinite dimensions*. Cambridge university press, 2014.
- N. Deb and B. Sen. Multivariate rank-based distribution-free nonparametric testing using measure transportation. *Journal of the American Statistical Association*, 118(541):192–207, 2023.
- J. Duchon. Splines minimizing rotation-invariant semi-norms in sobolev spaces. In *Constructive Theory of Functions of Several Variables: Proceedings of a Conference Held at Oberwolfach April 25–May 1, 1976*, pages 85–100. Springer, 1977.
- D. B. Dunson and N. Wu. Inferring manifolds from noisy data using gaussian processes. *arXiv preprint arXiv:2110.07478*, 2021.
- P. Dupuis, U. Grenander, and M. I. Miller. Variational problems on flows of diffeomorphisms for image matching. *Quarterly of applied mathematics*, pages 587–600, 1998.
- H. Edelsbrunner and J. Harer. *Computational topology: an introduction*. American Mathematical Society, 2010.
- H. Edelsbrunner, D. Letscher, and A. Zomorodian. Topological persistence and simplification. In *Proceedings 41st annual symposium on foundations of computer science*, pages 454–463. IEEE, 2000.

- L. C. Evans. *Partial differential equations*, volume 19. American Mathematical Society, 2010.
- J. Fan. Test of significance based on wavelet thresholding and neyman’s truncation. *Journal of the American Statistical Association*, 91(434):674–688, 1996.
- J. J. Faraway. Regression analysis for a functional response. *Technometrics*, 39(3):254–261, 1997.
- B. T. Fasy, F. Lecci, A. Rinaldo, L. Wasserman, S. Balakrishnan, and A. Singh. Confidence sets for persistence diagrams. *The Annals of Statistics*, 42(6):2301–2339, 2014.
- B. T. Fasy, S. Micka, D. L. Millman, A. Schenfisch, and L. Williams. Challenges in reconstructing shapes from euler characteristic curves. *arXiv preprint arXiv:1811.11337*, 2018.
- M. Fréchet. Les éléments aléatoires de nature quelconque dans un espace distancié. In *Annales de l’institut Henri Poincaré*, volume 10, pages 215–310, 1948.
- K. J. Friston, C. D. Frith, P. F. Liddle, and R. S. Frackowiak. Functional connectivity: the principal-component analysis of large (pet) data sets. *Journal of Cerebral Blood Flow & Metabolism*, 13(1):5–14, 1993.
- K. Fukumizu, A. Gretton, G. Lanckriet, B. Schölkopf, and B. K. Sriperumbudur. Kernel choice and classifiability for rkhs embeddings of probability distributions. In *Advances in Neural Information Processing Systems*, volume 22. Curran Associates, Inc., 2009. URL https://proceedings.neurips.cc/paper_files/paper/2009/file/685ac8cad1be5ac98da9556bc1c8d9e-Paper.pdf.

- T. Gao, S. Z. Kovalsky, D. M. Boyer, and I. Daubechies. Gaussian process landmarking for three-dimensional geometric morphometrics. *SIAM Journal on Mathematics of Data Science*, 1(1):237–267, 2019a.
- T. Gao, S. Z. Kovalsky, and I. Daubechies. Gaussian process landmarking on manifolds. *SIAM Journal on Mathematics of Data Science*, 1(1):208–236, 2019b.
- R. Ghrist, R. Levanger, and H. Mai. Persistent homology and euler integral transforms. *Journal of Applied and Computational Topology*, 2:55–60, 2018.
- R. W. Ghrist. *Elementary applied topology*, volume 1. Createspace Seattle, 2014.
- T. Górecki and Ł. Smaga. A comparison of tests for the one-way anova problem for functional data. *Computational Statistics*, 30:987–1010, 2015.
- T. Górecki and Ł. Smaga. fdanova: an r software package for analysis of variance for univariate and multivariate functional data. *Computational Statistics*, 34(2):571–597, 2019.
- A. Goswami. Phenome10k: a free online repository for 3-d scans of biological and palaeontological specimens. *Google Scholar*, 2015.
- U. Grenander and M. I. Miller. Computational anatomy: An emerging discipline. *Quarterly of applied mathematics*, 56(4):617–694, 1998.
- A. Gretton, K. Borgwardt, M. Rasch, B. Schölkopf, and A. Smola. A kernel method for the two-sample-problem. *Advances in neural information processing systems*, 19, 2006.
- A. Gretton, K. M. Borgwardt, M. J. Rasch, B. Schölkopf, and A. Smola. A kernel two-sample test. *The Journal of Machine Learning Research*, 13(1):723–773, 2012.

- O. Hacquard and V. Lebovici. Euler characteristic tools for topological data analysis. *arXiv preprint arXiv:2303.14040*, 2023.
- M. Hadac, S. Herr, and H. Koch. Well-posedness and scattering for the kp-ii equation in a critical space. In *Annales de l'Institut Henri Poincaré C, Analyse non linéaire*, volume 26, pages 917–941. Elsevier, 2009.
- O. Hagrass, B. K. Sriperumbudur, and B. Li. Spectral regularized kernel goodness-of-fit tests. *arXiv preprint arXiv:2308.04561*, 2023.
- M. Hairer. An introduction to stochastic pdes. *arXiv preprint arXiv:0907.4178*, 2009.
- A. Hatcher. *Algebraic topology*. New York : Cambridge University Press, 2002.
- E. C. Holland. Glioblastoma multiforme: the terminator. *Proceedings of the National Academy of Sciences*, 97(12):6242–6244, 2000.
- T. Hsing and R. Eubank. *Theoretical foundations of functional data analysis, with an introduction to linear operators*, volume 997. John Wiley & Sons, 2015.
- M. Ji, K. Meng, and K. Ding. Euler characteristics and homotopy types of definable sublevel sets, with applications to topological data analysis. *arXiv preprint arXiv:2309.03142*, 2023.
- B. Z. Jia Guo and J.-T. Zhang. New tests for equality of several covariance functions for functional data. *Journal of the American Statistical Association*, 114(527):1251–1263, 2019. doi: 10.1080/01621459.2018.1483827. URL <https://doi.org/10.1080/01621459.2018.1483827>.
- Q. Jiang, S. Kurtek, and T. Needham. The weighted Euler curve transform for shape and

- image analysis. In *Proceedings of the IEEE/CVF Conference on Computer Vision and Pattern Recognition Workshops*, pages 844–845, 2020.
- J. Jumper, R. Evans, A. Pritzel, T. Green, M. Figurnov, O. Ronneberger, K. Tunyasuvunakool, R. Bates, A. Žídek, A. Potapenko, et al. Highly accurate protein structure prediction with alphafold. *Nature*, 596(7873):583–589, 2021.
- O. Kallenberg. *Foundations of modern probability*, volume 2. Springer, 2021.
- I. Karatzas and S. Shreve. *Brownian motion and stochastic calculus*, volume 113. Springer Science & Business Media, 2012.
- D. G. Kendall. The diffusion of shape. *Advances in applied probability*, 9(3):428–430, 1977.
- D. G. Kendall. Shape manifolds, procrustean metrics, and complex projective spaces. *Bulletin of the London mathematical society*, 16(2):81–121, 1984.
- D. G. Kendall. A survey of the statistical theory of shape. *Statistical Science*, 4(2):87–99, 1989.
- H. Kirveslahti and S. Mukherjee. Representing fields without correspondences: the lifted euler characteristic transform. *Journal of Applied and Computational Topology*, pages 1–34, 2023.
- A. Klenke. *Probability theory: a comprehensive course*. Springer Science & Business Media, 2013.
- S. Kurtek, E. Klassen, Z. Ding, S. W. Jacobson, J. L. Jacobson, M. J. Avison, and A. Srivastava. Parameterization-invariant shape comparisons of anatomical surfaces. *IEEE Transactions on Medical Imaging*, 30(3):849–858, 2010.

- S. Kurtek, E. Klassen, J. C. Gore, Z. Ding, and A. Srivastava. Elastic geodesic paths in shape space of parameterized surfaces. *IEEE transactions on pattern analysis and machine intelligence*, 34(9):1717–1730, 2011.
- S. Kurtek, A. Srivastava, E. Klassen, and Z. Ding. Statistical modeling of curves using shapes and related features. *Journal of the American Statistical Association*, 107(499):1152–1165, 2012.
- Y. LeCun, L. Bottou, Y. Bengio, and P. Haffner. Gradient-based learning applied to document recognition. *Proceedings of the IEEE*, 86(11):2278–2324, 1998.
- H. Lee, M. K. Chung, H. Kang, B.-N. Kim, and D. S. Lee. Discriminative persistent homology of brain networks. In *2011 IEEE international symposium on biomedical imaging: from nano to macro*, pages 841–844. IEEE, 2011.
- D. Li, M. Mukhopadhyay, and D. B. Dunson. Efficient manifold approximation with spherelets. *Journal of the Royal Statistical Society Series B: Statistical Methodology*, 84(4):1129–1149, 2022.
- D. Li, P. Nguyen, Z. Zhang, and D. Dunson. Tree representations of brain structural connectivity via persistent homology. *Frontiers in Neuroscience*, 17:1200373, 2023.
- J. Li and K. Meng. Global well-posedness for the fifth order kadomtsev–petviashvili ii equation in three dimensional space. *Nonlinear Analysis*, 130:157–175, 2016. ISSN 0362-546X. doi: <https://doi.org/10.1016/j.na.2015.09.030>. URL <https://www.sciencedirect.com/science/article/pii/S0362546X15003375>.
- M. Lifshits. Lectures on gaussian processes. In *Lectures on Gaussian Processes*, pages 1–117. Springer, 2012.

- G. Lu. Embedding theorems into lipschitz and bmo spaces and applications to quasilinear subelliptic differential equations. *Publicacions Matemàtiques*, pages 301–329, 1996.
- W. Lv, P. He, and Q. Wang. Well-posedness for the stochastic novikov equation. *Statistics & Probability Letters*, 153:157–163, 2019.
- F. Maldonado, C. Varghese, S. Rajagopalan, F. Duan, A. B. Balar, D. A. Lakhani, S. L. Antic, P. P. Massion, T. F. Johnson, R. A. Karwoski, et al. Validation of the broders classifier (benign versus aggressive nodule evaluation using radiomic stratification), a novel hrct-based radiomic classifier for indeterminate pulmonary nodules. *European Respiratory Journal*, 57(4), 2021.
- L. Marsh, F. Y. Zhou, X. Quin, X. Lu, H. M. Byrne, and H. A. Harrington. Detecting temporal shape changes with the euler characteristic transform. *arXiv preprint arXiv:2212.10883*, 2022.
- K. Meng and A. Eloyan. Principal Manifold Estimation Via Model Complexity Selection. *Journal of the Royal Statistical Society Series B: Statistical Methodology*, 83(2):369–394, 03 2021. ISSN 1369-7412. doi: 10.1111/rssb.12416. URL <https://doi.org/10.1111/rssb.12416>.
- K. Meng and A. Eloyan. Population-level task-evoked functional connectivity via Fourier analysis. *Journal of the Royal Statistical Society Series C: Applied Statistics*, page qlae015, 03 2024. ISSN 0035-9254. doi: 10.1093/jrssc/qlae015. URL <https://doi.org/10.1093/jrssc/qlae015>.
- K. Meng, M. Ji, J. Wang, K. Ding, H. Kirveslahti, A. Eloyan, and L. Crawford. Statistical inference on grayscale images via the euler-radon transform. *arXiv preprint arXiv:2308.14249*, 2023.

- Y. Mileyko, S. Mukherjee, and J. Harer. Probability measures on the space of persistence diagrams. *Inverse Problems*, 27(12):124007, 2011.
- E. Miller. Fruit flies and moduli: interactions between biology and mathematics. *Notices of the AMS*, 62(10):1178–1184, 2015.
- N. Milosavljević, D. Morozov, and P. Skraba. Zigzag persistent homology in matrix multiplication time. In *Proceedings of the twenty-seventh Annual Symposium on Computational Geometry*, pages 216–225, 2011.
- I. Molchanov. *Theory of random sets*, volume 19. Springer, 2005.
- C. Moon, Q. Li, and G. Xiao. Predicting survival outcomes using topological features of tumor pathology images. *arXiv preprint arXiv:2012.12102*, 2020.
- K. Muandet, K. Fukumizu, B. Sriperumbudur, B. Schölkopf, et al. Kernel mean embedding of distributions: A review and beyond. *Foundations and Trends® in Machine Learning*, 10(1-2):1–141, 2017.
- E. Munch. An invitation to the euler characteristic transform. *arXiv preprint arXiv:2310.10395*, 2023.
- P. Niyogi, S. Smale, and S. Weinberger. Finding the homology of submanifolds with high confidence from random samples. *Discrete & Computational Geometry*, 39(1-3):419–441, 2008.
- M. Pauly, E. Brunner, and F. Konietzschke. Asymptotic Permutation Tests in General Factorial Designs. *Journal of the Royal Statistical Society Series B: Statistical Methodology*, 77(2):461–473, 05 2014. ISSN 1369-7412. doi: 10.1111/rssb.12073. URL <https://doi.org/10.1111/rssb.12073>.

- A. Petersen and H.-G. Müller. Fréchet regression for random objects with euclidean predictors. *The Annals of Statistics*, 47(2):691–719, 2019.
- C. E. Rasmussen and C. K. Williams. *Gaussian processes for machine learning*, volume 2. MIT press Cambridge, MA, 2006.
- M. Reed and B. Simon. *Methods of modern mathematical physics: Functional analysis*. New York, Academic Press, 1972.
- A. Robinson and K. Turner. Hypothesis testing for topological data analysis. *Journal of Applied and Computational Topology*, 1(2):241–261, 2017.
- B. Roycraft, J. Krebs, and W. Polonik. Bootstrapping persistent betti numbers and other stabilizing statistics. *The Annals of Statistics*, 51(4):1484–1509, 2023.
- P. Schapira. Cycles lagrangiens, fonctions constructibles et applications. *Séminaire Équations aux dérivées partielles (Polytechnique) dit aussi "Séminaire Goulaouic-Schwartz"*, pages 1–9, 1988.
- P. Schapira. Operations on constructible functions. *Journal of pure and applied algebra*, 72(1):83–93, 1991.
- P. Schapira. Tomography of constructible functions. In *International Symposium on Applied Algebra, Algebraic Algorithms, and Error-Correcting Codes*, pages 427–435. Springer, 1995.
- Q. Shen and J. Faraway. An f test for linear models with functional responses. *Statistica Sinica*, pages 1239–1257, 2004.
- T. Sikora. The mpeg-7 visual standard for content description-an overview. *IEEE Transactions on circuits and systems for video technology*, 11(6):696–702, 2001.

- A. Smola, A. Gretton, L. Song, and B. Schölkopf. A hilbert space embedding for distributions. In *International conference on algorithmic learning theory*, pages 13–31. Springer, 2007.
- E. Somasundaram, A. Litzler, R. Wadhwa, S. Owen, and J. Scott. Persistent homology of tumor ct scans is associated with survival in lung cancer. *Medical physics*, 48(11):7043–7051, 2021.
- B. K. Sriperumbudur, A. Gretton, K. Fukumizu, B. Schölkopf, and G. R. Lanckriet. Hilbert space embeddings and metrics on probability measures. *The Journal of Machine Learning Research*, 11:1517–1561, 2010.
- B. K. Sriperumbudur, K. Fukumizu, and G. R. Lanckriet. Universality, characteristic kernels and rkhs embedding of measures. *Journal of Machine Learning Research*, 12(7), 2011.
- W. S. Tang, G. M. da Silva, H. Kirveslahti, E. Skeens, B. Feng, T. Sudijono, K. K. Yang, S. Mukherjee, B. Rubenstein, and L. Crawford. A topological data analytic approach for discovering biophysical signatures in protein dynamics. *PLoS computational biology*, 18(5):e1010045, 2022.
- K. Turner. Means and medians of sets of persistence diagrams. *arXiv preprint arXiv:1307.8300*, 2013.
- K. Turner, S. Mukherjee, and D. M. Boyer. Persistent homology transform for modeling shapes and surfaces. *Information and Inference: A Journal of the IMA*, 3(4):310–344, 2014.
- L. van den Dries. *Tame topology and o-minimal structures*, volume 248. Cambridge university press, 1998.

- C. Villani et al. *Optimal transport: old and new*, volume 338. Springer, 2009.
- O. Vipond, J. A. Bull, P. S. Macklin, U. Tillmann, C. W. Pugh, H. M. Byrne, and H. A. Harrington. Multiparameter persistent homology landscapes identify immune cell spatial patterns in tumors. *Proceedings of the National Academy of Sciences*, 118(41), 2021.
- O. Y. Viro. Some integral calculus based on euler characteristic. *Lecture Notes in Math.*, vol. 1346:127–138, 1988.
- G. Wahba. *Spline models for observational data*. SIAM, 1990.
- B. Wang, T. Sudijono, H. Kirveslahti, T. Gao, D. M. Boyer, S. Mukherjee, and L. Crawford. A statistical pipeline for identifying physical features that differentiate classes of 3d shapes. *The Annals of Applied Statistics*, 15(2):638–661, 2021.
- Y. Wang, J. Yin, and R. H. Desai. Topological inference on brain networks across subtypes of post-stroke aphasia. *ArXiv*, 2023.
- D. Wei and Z. Zhang. Transition threshold for the 3d couette flow in sobolev space. *Communications on Pure and Applied Mathematics*, 74(11):2398–2479, 2021.
- J. Yang, I. Anishchenko, H. Park, Z. Peng, S. Ovchinnikov, and D. Baker. Improved protein structure prediction using predicted interresidue orientations. *Proceedings of the National Academy of Sciences*, 117(3):1496–1503, 2020.
- K. Yosida. *Functional analysis*, volume 123. Springer Science & Business Media, 2012.
- J.-T. Zhang. Statistical inferences for linear models with functional responses. *Statistica Sinica*, pages 1431–1451, 2011.
- J.-T. Zhang. *Analysis of variance for functional data*. CRC press, 2013.

J.-T. Zhang and J. Chen. Statistical inferences for functional data. *The Annals of Statistics*, 35(3):1052 – 1079, 2007.